

---

# Expedition 316 Site C0004<sup>1</sup>

---

Expedition 316 Scientists<sup>2</sup>

## Chapter contents

Background and objectives	1
Operations	2
Lithology	2
Structural geology	5
Biostratigraphy	8
Paleomagnetism	10
Inorganic geochemistry	13
Organic geochemistry	18
Microbiology and biogeochemistry	19
Physical properties	19
References	23
Figures	25
Tables	84

## Background and objectives

Integrated Ocean Drilling Program (IODP) Site C0004 (proposed Site NT2-01I; Kimura et al., 2007) targeted the uppermost 400 meters below seafloor (mbsf) at the seaward edge of the Kumano Basin uplift (outerarc high) where the megasplay fault system branches and approaches the surface (Figs. F1, F2) (Moore et al., 2007). The scientific objectives at Site C0004 are to clarify the character and behavior of the shallow portion of the megasplay, characterize its slip and deformation mechanisms and the evolution of the region updip of the (inferred) unstable seismogenic fault, and investigate the relationship between fluid behavior, slip, and deformation along and adjacent to the megasplay fault.

As described in the IODP Expedition 316 *Scientific Prospectus* (Kimura et al., 2007), proposed Site NT2-01B was intended to penetrate the splay fault at ~600 mbsf and had a planned total depth (TD) of 1000 mbsf. Because of drilling difficulties at this site during IODP Expedition 314, Site NT2-01I was selected as an alternate site where the splay fault could be drilled at a shallower depth (~300 mbsf). TD was 398 mbsf, allowing examination of the slope sediments, prism, splay fault, and underthrust sediments.

During Expedition 314, Hole C0004B was drilled using logging while drilling (LWD) to obtain downhole geophysical information and images (see Fig. F1 in the “Expedition 314 Site C0004” chapter). Interpretation of gamma ray, resistivity, sonic velocity, and caliper log responses during Expedition 314 suggested three logging units corresponding to the slope sediment, accretionary prism, and underthrust sediments. Resistivity-at-the-bit (RAB) images were used during Expedition 314 to define three structural domains that differed in depth ranges from the inferred logging units. The upper domain was characterized by a lack of fractures and weak breakouts, the middle domain was characterized by a series of zones with conductive fractures and intensive development of borehole breakouts, and the deepest domain has gentle dips on bedding planes, less common fractures, and narrower breakouts.

Core samples collected during Expedition 316 provide a vital addition to the LWD data. The recovered cores allow description of lithology and structure, provide age control through paleontological and paleomagnetic analyses, and provide samples for interstitial water, microbiology, and shipboard and physical property and geotechnical studies. In addition to core samples, in situ temperature measurements provide an important control for thermal

<sup>1</sup>Expedition 316 Scientists, 2009. Expedition 316 Site C0004. In Kinoshita, M., Tobin, H., Ashi, J., Kimura, G., Lallemand, S., Screaton, E.J., Curewitz, D., Masago, H., Moe, K.T., and the Expedition 314/315/316 Scientists, *Proc. IODP, 314/315/316*: Washington, DC (Integrated Ocean Drilling Program Management International, Inc.). doi:10.2204/iodp.proc.314315316.133.2009  
<sup>2</sup>Expedition 314/315/316 Scientists' addresses.



models of the subduction zone. The results, when integrated with data from other Nankai Trough Seismogenic Zone Experiment (NanTroSEIZE) expeditions, will characterize physical properties, strength, composition, and structure of the slope sediments, hanging wall, and footwall of the splay fault. Development of the splay fault at this site will also be compared to later drilling of the splay fault at greater depths at Sites C0001 and C0002.

## Operations

### Positioning on Site C0004

The D/V *Chikyu* arrived at Site C0004 on 19 December 2007. The final site drilled during IODP Expedition 315 was <5 nmi from Site C0004, requiring minimal transit time prior to the start of Expedition 316 operations. Additionally, because the site was occupied during Expedition 314 for both pilot hole (Hole C0004A) and LWD (Hole C0004B) operations, the acoustic beacons required for dynamic positioning (DP) operations were already in place. The first part of the science party arrived on the vessel on 13 December, and by the afternoon of 19 December all were onboard. Hole C0004C was tagged at 0535 h on 20 December at 2632 m drillers depth below rig floor (DRF) (2603.5 m mud depth below sea level [MSL]).

### Hole C0004C

Hydraulic piston coring system (HPCS) coring commenced at that time and continued to 89.22 m core depth below seafloor (CSF). Three advanced piston coring temperature tool (APCT3) measurements were taken at the same time Cores 316-C0004C-3H, 6H, and 9H were collected. We changed to the extended shoe coring system (ESCS) at 2213 h on 20 December 2007 and continued to 127.22 m CSF. Because of poor ESCS core quality, we changed back to the HPCS at 0447 h on 21 December and collected three cores (316-C0004C-16H through 18H). The last HPCS core (316-C0004C-18H, 133.18–135.00 m CSF) also included an APCT3 run. At 0732 h on 21 December, because of failure to achieve full penetration using the HPCS, we pulled the bottom-hole assembly (BHA) and drill pipe out of the hole and killed the hole with high-density mud.

Table T1 shows the cores collected, type of coring system, depths, and recovery for Hole C0004C.

### Hole C0004D

Repositioning to Hole C0004D began at 1300 h on 21 December 2007, while making up the rotary core barrel (RCB) assembly and running pipe to the seafloor.

We tagged Hole C0004D at 0030 h on 22 December at 2659 m DRF (2630.5 m MSL) and washed to 100 m CSF. We commenced RCB coring at 1225 h on 22 December. During RCB coring, we inferred several instances of plugged bit throat and plugged bit nozzles from coring results and pressure readings and conducted bit unplugging to clear the problem. We used variations in rotations per minute (rpm) and drilling fluid pressure/flow rate to attempt to improve recovery and cleaned the bit by increasing flow after each core. Additionally, because of recovery problems, short cores (4.5 m) were taken on every coring run below 238 m CSF (Core 316-C0004D-21R).

Coring was delayed several times because of weather conditions, for a total of ~6 h of standby. An additional 3 h of downtime was caused by a fault in the integrated automation system that provides power to one of the DP modules.

Drilling reached TD (400 m CSF) at 2334 h on 25 December. We pulled out of the hole and killed the hole with high-density mud. Then we tripped the drill string and broke down the bit assembly.

We recovered seafloor acoustic navigation beacons, repositioned the vessel to IODP Site C0006, and commenced preparations for testing the underwater television camera (for drilling at depths >3000 m MSL).

Table T2 shows the cores collected, type of coring system, depths, and recovery for Hole C0004D.

## Lithology

Four lithologic units were recognized during examination of cores from Site C0004 (Fig. F3; Table T3). Two subunits are recognized in Unit II. Units and subunits are differentiated based on contrasts in grain size, mineralogy, composition, and presence (and thickness) of minor lithologies. In choosing unit boundaries, we also considered biostratigraphic information, paleomagnetic data, X-ray computed tomography (CT) images, observations of structural style, and interpretations of LWD and seismic results obtained during Expedition 314 (see the “Expedition 314 Site C0004” chapter).

### Unit I (slope-apron facies)

Interval: Sections 316-C0004C-1H-1, 0 cm, through 9H-5, 70 cm

Depth: Hole C0004C = 0.00–78.06 m CSF

Age: Pleistocene

The dominant lithology of Unit I is greenish gray silty clay with a substantial component of calcareous nannofossils (up to ~25%) and a lesser amount of siliceous biogenic debris (sponge spicules, diatoms,

and radiolarians) (Fig. F3; Table T3). In LWD data, the comparable base of logging Unit I was placed at 67.9 m CSF. Green color banding is present throughout most of the unit (Fig. F4) along with isolated glauconite grains. Secondary lithologies include thin interbeds and irregular patches of sand, sandy silt, silt, and volcanic ash.

An additional minor lithology is synsedimentary breccia (silty clay clasts in a silty clay matrix; ranging from ~4 to 30 cm thick) recognized in X-ray CT images (Section 316-C0004C-1H-1) (Fig. F5). The breccia is cryptic in the split core. Sediment at the top of the core has suffered drilling-induced disturbance, including drag folding along the core liner, vertical rotation of disrupted stratum, and flow texture with liquefaction. Despite this disturbance, some horizontal layers are preserved, and it is clear that intervals of sedimentary breccia are interspersed with horizontally bedded sediment. Some trace fossils penetrate both clasts and horizontal layers, clear evidence that the brecciation predates coring and is not a drilling-induced artifact. Within the breccia layers, dark gray (low CT number) clasts are mixed within a light gray (high CT number) matrix.

Within Unit I there is a consistent trend in bulk powder X-ray diffraction (XRD) data toward diminishing calcite content with depth (Fig. F6; Tables T4, T5), ranging from ~20% near the top of the cores to below XRD detection at the lower unit boundary. The silt and sand fraction is dominated by quartz and plagioclase (averaging 21% and 19% of the bulk sediment, respectively) and locally includes abundant clear volcanic glass and pumice fragments.

The Unit I/II boundary is an angular unconformity that dips ~50° across the core (Fig. F7). The unconformity is associated with a significant stratigraphic hiatus, as indicated by both paleomagnetic and nanofossil data (see “**Biostratigraphy**” and “**Paleomagnetism**”). X-ray fluorescence (XRF) scanning data show significant variation in rock composition in the vicinity of the unconformity (Fig. F8); CaO declines uniformly from ~7 wt% in the silty mud 10 cm above the unconformity to ~2 wt% immediately above the unconformity. Iron displays an ~2 wt% increase in the 2 cm below the unconformity.

Unit I was deposited from early to late Pleistocene as a sediment blanket on the trench slope mainly by hemipelagic settling with minor volcanic ash and sand-silt input. The gradual increase in carbonate content upsection is consistent with greater carbonate dissolution at depth and implies that the unit was slowly uplifted to its present water depth of 2632 m. Gradual tectonic uplift is consistent with accretion and thickening of the underlying accretionary prism during the Pleistocene. A similar history

was recorded at IODP Site C0001 (see the “**Expedition 315 Site C0001**” chapter) and Ocean Drilling Program (ODP) Sites 1175, 1176, and 1178 of the Muroto transect (Shipboard Scientific Party, 2001a, 2001b, 2001c; Underwood et al., 2003; Moore, Taira, Klaus, et al., 2001; Moore et al., 2001), ~200 km west-southwest of Site C0004.

## Unit II (upper accretionary prism)

Intervals: Sections 316-C0004C-9H-5, 70 cm, through 15X-1, 0 cm, and 316-C0004D-1R-1, 0 cm, through 25R-CC, 29 cm

Depths: Hole C0004C = 78.06–117.72 m CSF and Hole C0004D = 100.00–258.01 m CSF

Age: Pliocene

Strata below the unconformity at the top of Unit II extend from 78.06 m CSF in Hole C0004C to 258.01 m CSF (Fig. F3). Within this interval, Expedition 314 shipboard scientists recognized four subunits in the logs (see the “**Expedition 314 Site C0004**” chapter). Lithologic variations in the cores, however, do not precisely correspond to these divisions. Two subunits are recognized in the cores with a boundary at 117.72 m CSF.

### Subunit IIA (mass-transport complex)

Interval: Sections 316-C0004C-9H-5, 70 cm, through 15X-1, 0 cm

Depth: Hole C0004C = 78.06–117.72 m CSF

Age: Pliocene

The dominant lithology of Subunit IIA is greenish gray synsedimentary breccia made of rounded to subangular clasts of pebble size with subsidiary silty clay horizons (Figs. F7, F8). Both the clasts and the matrix in the breccia are composed of dark greenish gray silty clay, and no discernible compositional difference exists between the two parts of the sediment. The breccia is clast-supported in places and matrix-supported in others, and there are horizons in which no obvious clasts can be identified in either visual core description (VCD) or X-ray CT scans. We interpret the mud intervals as products of hemipelagic settling between episodes of mass wasting and formation of mass-transport deposits. Locally, patches of hemipelagic mud clasts occur within the base of overlying breccia beds, indicating reworking and a rather catastrophic style of mass wasting deposition (e.g., Hampton et al., 1996). The immediate upslope source of the mass-transport deposits, slope sediments versus reworked prism material versus some combination of these sources, cannot be discriminated on the basis of shipboard observation.

Thin layers of silt or silty sand are rare and are restricted to the upper part of the unit (Fig. F3),

although their absence in the lower part of the unit cannot be proven indisputably because of poor core recovery. Volcanic ash layers are also rare and thin (Fig. F9). Calcareous nannofossils are significantly less abundant in this unit than within comparable mud deposits of Unit I as shown by the calcite XRD values (Fig. F6), which are generally below detection (0%–5%; average = 0.8%). Quartz and plagioclase content in the bulk sediment (averaging 21% and 19%, respectively) display no trend within the unit.

Preliminary observations in core and X-ray CT images suggest that sediments immediately below the unconformity (i.e., at the top of Unit II) preserve a complex paragenetic sequence that potentially encompasses burial, chemical alteration and deformation, uplift, and seafloor exposure. Pyrite mineralization is clearly visible in the core in the top 5 cm below the unconformity (Fig. F7B, F7C). Pyrite in proximity to the unconformity forms cubes and aggregates of cubes (Fig. F10) that contrast with the mostly framboidal form of pyrite that is widely distributed through the muddy lithologies throughout the core. In X-ray CT images, pyrite fills near-vertical fractures that end abruptly at the upper surface of the unconformity and do not transect the overlying hemipelagic mudstones (Fig. F7B).

Subunit IIA has only been positively identified in Hole C0004C and does not appear to be present in Hole C0004D. However, drilling disturbance (by rotary drilling) in Hole C0004D in particular has caused widespread brecciation of Unit II, which may have masked much of the original texture of the rock, including the sedimentary breccias observed in Hole C0004C. The base of Subunit IIA is picked partially on the basis of a discernible drop in magnetic susceptibility (see “Paleomagnetism”) and partially on the basis of small changes in XRD mineralogy (Fig. F6).

### Subunit IIB

Interval: Sections 316-C0004D-1R-1, 0 cm,  
through 25R-CC, 29 cm  
Depth: Hole C0004D = 100.00–258.01 m CSF  
Age: Pliocene

The dominant lithology in Subunit IIB is dark greenish gray silty clay. Minor breccias may also occur, but these are difficult to identify because of the extensive drilling-induced brecciation of the core. Sand and silt beds were not observed, though their absence could be ascribed to the poor core recovery throughout much of the interval because LWD in Expedition 314 suggests the existence of sand/silt beds in this unit (see the “Expedition 314 Site C0004” chapter). Minor ash (Fig. F9) and carbonate (0%–6%; average = 1%) occurrences are observed in the upper portions

of this subunit. Quartz and plagioclase content in the mud average 18% and 17%, respectively. Overall, assessment of this subunit was hampered by poor core recovery.

### Summary for Unit II

Logging Unit II was interpreted during Expedition 314 as the accretionary prism based on seismic data and log characteristics (see the “Expedition 314 Site C0004” chapter). Coring during Expedition 316 indicates that the uppermost part of Unit II consists mainly of sedimentary breccia with silty clay clasts that most likely resulted from deposition of slumps and mass wasting along an unstable slope. The original environment of deposition is conjectural. The low carbonate content of Unit II is consistent with deposition at much greater depths than its present setting and was presumably formed either close to or below the calcite compensation depth.

### Unit III (structurally bounded package)

Interval: Sections 316-C0004D-25R-CC, 29 cm,  
through 36R-CC, 5 cm  
Depth: Hole C0004D = 258.01–307.52 m CSF  
Age: Pliocene

Volcanic ash layers appear to be more common below 250 m CSF than in the overlying but poorly recovered Subunit IIB (Fig. F9). Dispersed glass and pumice clasts/microclasts are also common in the silty clay in this interval. Vitric grains are typically more abundant than quartz and feldspar grains (averaging 20% and 19%, respectively) in these sediments. XRD results show that calcite is also slightly more abundant (0%–9%; average = 2.7%) than in the overlying subunit.

The exact position of the Unit II/III boundary is difficult to identify from lithologic information alone. However, a small biostratigraphic age reversal above and below 258.01 m CSF (Cores 316-C0004D-25R and 26R) coincides with a lithologic change to slightly more calcitic and ash-bearing sediments across a fault contact between Units II and III. A larger age reversal is found at the Unit III/IV boundary at 307.52 m CSF. Unit III is a structurally bounded package that hosts most of the prominent brittle deformation in the hanging wall of the thrust fault zone (see “Structural geology”). Its original stratigraphic affinity is ambiguous. The Pliocene-age fault-bounded sedimentary package may be related to the overlying slightly older Pliocene-age prism sediments (a repetition of the overlying age-equivalent upper part of Subunit IIB). Alternatively, a fault-transported sliver may have been derived from the underlying underthrust sequence (a unit that would be encountered beneath Unit IV).

## Unit IV (underthrust slope facies)

Interval: Sections 316-C0004D-36R-CC, 5 cm, through 56R-CC, 15 cm

Depth: Hole C0004D = 307.52–398.79 m CSF

Age: Pleistocene

The dominant lithology of Unit IV is dark olive-gray silty clay with a moderate amount of calcareous nanofossils and a lesser amount of calcareous and siliceous microfossils (foraminifers, diatoms, radiolarians, and sponge spicules). The calcite content ranges from 0% to 39% and averages 3%. The mud is typically parallel laminated, although divergent or even wavy laminations can be observed locally. Bioturbation, by the *Zoophycos-Chondrites* association, is common throughout much of the section. Thin sand and silt beds are common in this unit, particularly in the upper part (Fig. F11), and some are graded. Grain size of the silty clay is typically coarser than in the overlying units. Volcanic ash beds are rare, along with a moderate amount of dispersed lapilli and glass shards. The low abundance of volcanoclastic grains as observed in smear slides, slightly greater carbonate content (as mentioned above), higher plagioclase content (average = 26%), and relative abundance of red-brown organic matter (Fig. F12) are some of the compositional attributes that have been used to distinguish these sediments from Unit III.

Unit IV is considered to have formed in a lower trench-slope environment, dominated by fine-grained hemipelagic deposition with relatively minor input of sand and silt turbidites. The environment was similar to that of Unit I, although the inclination of the seafloor may have been flatter, thereby allowing for more turbidite deposition. The lower carbonate content compared to Unit I (Fig. F5) may indicate that deposition was closer to the carbonate compensation depth (CCD), or alternatively, the pelagic calcite has been diluted by a larger siliciclastic influx.

### X-ray CT-defined lithologies

X-ray CT images were used extensively for evaluation of structural features in Units II and III. Figure F13 shows the depth trends for CT number (averaged pixel intensity for a 1 mm<sup>2</sup> area) determined for coherent rock pieces and tectonic breccia clasts. CT number reflects average sample density at the scale of the CT observation, a value that is affected both by sample composition (mineral composition and density) and porosity (bulk density); in these porous samples it is likely to be dominated by porosity. Across Units I, II, and III, CT number varies widely with no apparent discontinuities or depth trend. At the Unit III/IV boundary, CT number distinctly increases, which is consistent with the abrupt compo-

sitional change observed at this boundary. Average CT numbers of Unit I, Subunit IIB, and Units III and IV are 1223, 1235, 1208, and 1327, respectively. CT number of Unit III is notably lower than the others, especially in the lower part of Unit III below 274 m CSF, where it averages 1197. Attempted correlation of CT numbers to specific lithologies at the core scale was not successful. This result is not surprising, given the relatively high porosity in these samples and the relatively narrow range of densities characteristic of the main rock-forming minerals (clay minerals, quartz, feldspar, and calcite).

## Structural geology

Site C0004 penetrated the shallow portion of a splay fault crossing the prism. As can be expected from such a location, various deformation structures were observed in cores. All structural data are given as a supplementary material (see C0004\_STRUCT\_DATA.XLS in folder 316\_STRUCTURE in “[Supplementary material](#)”). Where possible, we corrected the measurements of planar and linear structures to true geographic coordinates using paleomagnetic data (see “[Structural geology](#)” in the “Expedition 316 methods” chapter). The distribution of planar structures and lithologic divisions with depth are shown in Figure F14. The chief structural features at this site are southeast-dipping beds and normal faults in lithologic Unit I (upper slope sediments) (0–78 m CSF), reverse faults and shear zones in Unit II (prism) (78–256 m CSF), a fractured/brecciated zone associated with Unit III (fault-bounded unit) (256–315 m CSF), and subhorizontal beds and fissility in Unit IV (underthrust slope sediments) (315–400 m CSF).

### Structures in Unit I (upper slope sediments)

Sediments deposited on the slope are only weakly deformed. After paleomagnetic correction, bedding surfaces dip gently to moderately southeastward (Fig. F15), which is consistent with the regional strike of the Nankai accretionary margin and southeast-dipping beds displayed in the seismic reflection profile passing through Site C0004 (see Fig. F3 in the “Expedition 316 summary” chapter). The high-angle faults are concentrated between 50 and 80 m CSF (Fig. F14). Most faults are planar, but some faults are bifurcated and curvilinear to irregular. Where displacement can be determined, all faults show a normal offset with displacements ranging from 2 to 10 mm (Fig. F16). After paleomagnetic correction, the fault orientations show a scattered distribution about the vertical (Fig. F17), possibly reflecting vertical compaction of the sediments.

## Structures in Unit II (prism)

There is no obvious deformation in the 78–100 m CSF interval of Hole C0004C. Drilling disturbance (i.e., biscuiting, fracturing, and brecciation) occurs throughout the cores recovered from prism sediments in the 100–256 m CSF interval of Hole C0004D. Particularly, drilling-induced brecciation often complicates identification of deformation structures and precludes measurements of structures. Intense drilling-induced brecciation coupled with poor core recovery cause scarcity of measurements in the prism sediments at 100–256 m CSF (Fig. F14). Despite these facts, faults and shear zones can locally be observed within the fragments of drilling-induced breccias. In addition, rare sediment-filled veins (vein structures) are observed within the fragments. In order to maintain consistent terminology between NanTroSEIZE Expeditions 315 and 316, the definitions of shear zones and sediment-filled veins follow those used during Expedition 315 (see the “[Expedition 315 Site C0001](#)” chapter).

In the cores, faults and shear zones are darker than the surrounding material and are spatially close to each other. In most cases, faults cut and offset shear zones and have a reverse sense of shear with displacement less than a few millimeters (Fig. F18A). Faults are planar and <1 mm thick. In contrast, shear zones change in thickness from 1 to 5 mm along their length and tend to bifurcate into twin strands that coalesce along zones (Fig. F18B). The margins of shear zones are polished and slickenlined. On X-ray CT images, shear zones are expressed as bright bands or seams with CT numbers ~150–200 higher than those of the surrounding material (Fig. F19). CT images suggest that shear zones are denser than the surrounding material. This may result from shear-induced consolidation.

Sediment-filled veins are characterized by parallel sets of sigmoidal or planar seams <1 mm wide. One fragment of drilling-induced breccia shows sediment-filled veins being displaced 2 mm along a shear zone with a reverse sense of shear (Fig. F18C).

## Structures in Unit III (fault-bounded unit)

Below 256 m CSF, drilling-induced brecciation still dominates but core recovery improved. We define a fractured/brecciated zone between 256 and 315 m CSF based on the following evidence:

- Fragments in the drilling-induced breccia at 256–315 m CSF ubiquitously have slickensided and slickenlined surfaces. In contrast, fragments in drilling-induced breccia above 256 m CSF commonly lack such features, except for “spiral” slickenlines clearly resulting from the coring process.

In addition, fragments between 256 and 315 m CSF tend to be smaller than those above 256 m CSF. Although drilling-induced brecciation precludes an accurate definition of the upper boundary of the fractured/brecciated zone, the abrupt occurrence of brecciated fragments with polished and slickenlined surfaces below 256 m CSF suggests that the upper boundary is sharp.

- From 310 to 315 m CSF, there is a gradual increase of unbroken rock intervals in which subhorizontal bedding and fissility are well preserved. Both natural breccias and drilling-induced breccias are absent below 315 m CSF. Therefore, we define the termination of brecciation at 315 m CSF as the lower boundary.
- Coherent sections of fractured rocks, fault breccia, and microbreccia are preserved between 256 and 315 m CSF. Microbreccia is absent above 256 m CSF and below 315 m CSF.
- Low-angle faults are developed only between 256 and 315 m CSF.

Therefore, the fractured/brecciated zone is ~60 m thick. Drilling-induced breccia between 256 and 315 m CSF is most likely derived from naturally fractured and brecciated intervals that have been enhanced by the drilling process. The seismic reflection profile passing through Site C0004 (see Fig. F3 in the “[Expedition 316 summary](#)” chapter) suggests that the projected depth of the splay fault is ~290 m CSF. There are two inversions of biostratigraphic age at ~259 and ~308 m CSF (see “[Biostratigraphy](#)”), which can be correlated with reverse faulting along the splay fault zone. Based on the correlation between these signals and our observations, we conclude that the ~60 m thick fractured/brecciated zone represents the splay fault zone.

## Structural elements in the splay fault zone

The structural elements in the splay fault zone are fractured rocks, fault breccia, and microbreccia. The distribution of each element is shown in Figure F20. Our observation indicates no obvious evidence of fluid-rock interaction (e.g., mineralized veins and alteration) in the fault zone.

### Fractured rocks

Fractured rocks are defined by a breakage of rocks into trapezoidal fragments along sets of fractures (Fig. F21). Some fragments are aligned along the inclined fractures. The trapezoidal fragments are commonly centimeter size with lengths <10 cm, but their sizes locally decrease to millimeter size and are locally replaced by brecciated material. Fragments do not exhibit visible internal deformation structures.

Most fracture surfaces are polished and striated. Some fracture measurements can be reoriented to true geographic coordinates using paleomagnetic data. The reoriented fracture surfaces do not show any preferred orientation (Fig. F22A), and slip directions are complex and heterogeneous (Fig. F22B).

### **Fault breccia**

Fault breccia is characterized by a predominance of angular to subangular fragments of centimeter to millimeter size. Brecciated fragments are commonly slickensided with variable slip directions. Fault breccia is locally characterized by the alignment of fragments that are inclined at moderate angle with respect to a horizontal plane, showing a foliated aspect. Despite intense fracturing and brecciation, the original layering of ash and mudstone has been preserved (Fig. F23). This layering suggests distributed fracturing and shearing with very small displacements along individual slip surfaces. On CT images, brecciated intervals are expressed as bright zones in which fragments are included in the matrix (Fig. F24). The contrast between the matrix and fragments is low, and the matrix CT numbers are commonly >1100 (Fig. F25A, F25B). These features contrast with those of drilling-induced breccias, which exhibit spherical voids and bright fragments in a much darker matrix characterized by low CT numbers (700–900) (Fig. F25C, F25D). In general, high CT numbers correspond to bright colors in CT images, reflecting relatively high bulk density (low porosity), and there is a positive linear relationship between CT number and bulk density (see “X-ray computed tomography” in the “Expedition 316 methods” chapter). Apparently, fault breccia matrix is much denser than drilling-induced breccia matrix.

### **Microbreccia**

Microbreccia is marked by a zone of comminution that is mainly composed of angular to subangular fragments of millimeter to <1 mm size (Fig. F26). The CT character of microbreccia is similar to that of fault breccia: low contrast between the matrix and fragments and matrix CT numbers >1100.

### **Internal characteristics of the fault zone**

Two biostratigraphic age reversals correspond to intervals of poor core recovery within the fault zone (Fig. F20). Based on recovered cores, fractured rocks and drilling-induced breccias are widely distributed in the fault zone, whereas fault breccia and microbreccia have relatively limited distribution. The upper and lower boundaries of fault breccia zones and microbreccia zones are commonly obscured by drilling-induced brecciation and nonrecovery of cores.

At 291 m CSF, however, a 6 cm thick microbreccia is bounded above and below by fault breccia ~50 cm thick, which in turn is bounded above and below by fractured rocks (Figs. F20, F26). The localized comminution in microbreccia zones contrasts with distributed deformation in fractured rocks and fault breccia.

## **Structures in Unit IV (underthrust slope sediments)**

Overall, the underthrust slope sediments exhibit horizontal to gently dipping bedding and fissility (Figs. F14, F27), which is consistent with the bedding dips acquired by the borehole images at this site (see the “Expedition 314 Site C0004” chapter) and the seismic reflection profile (see Fig. F3 in the “Expedition 316 summary” chapter). Fissility was reported elsewhere in the Nankai accretionary margin and is thought to result from burial compaction (Taira, Hill, Firth, et al., 1991; Moore, Taira, Klaus, et al., 2001). Steeply dipping faults are sporadically distributed in the underthrust sediments. After paleomagnetic correction, the orientations of these faults show highly scattered distribution with variable shear sense, suggesting a lack of tectonic influence associated with plate convergence (Fig. F28).

Bedding-oblique foliation is recognized in mudstone at 355–360 m CSF. This foliation lacks polished and striated surfaces. The crosscutting relationship between bedding-oblique foliation and fissility is invisible at the core scale. Bedding-oblique foliation was documented at ODP Site 1178 in the upper part of the Nankai accretionary prism and is considered to correspond to the flattening plane associated with shear deformation in a fault zone (Ujiie et al., 2003). Another possible origin of bedding-oblique foliation includes an axial planar cleavage associated with folding. In the underthrust slope sediments of Site C0004, however, neither distinct fault zones nor folds are recognized in the cores or in the seismic reflection profile (see Fig. F3 in the “Expedition 316 summary” chapter); the origin of bedding-oblique foliation at Site C0004 remains unclear.

## **Discussion**

The shallow portion of the splay fault zone is marked by brittle deformation. The aspects of fracturing and brecciation in the fault zone are similar to those of the décollement zone in the Nankai accretionary prism off Muroto (ODP Sites 1174 and 808) (Taira, Hill, Firth, et al., 1991; Moore, Taira, Klaus, et al., 2001) and the fault zones in the accretionary prism at Site C0002 (see the “Expedition 315 Site C0002” chapter). However, the splay fault zone contains mi-

crobreccia zones, including fragments that are thinner and finer than those previously reported in fault zones in shallow parts (<1 km in depth) of the Nankai accretionary prism. Microbreccia possibly represents a zone of concentrated shear within the splay fault zone. However, the location of microbrecciation is not correlated with two inversions of biostratigraphic age (Figs. F14, F20).

Two intervals at which biostratigraphic age reversals occur are also candidates for concentrated shear in the fault zone. Borehole image analysis of the structurally defined fault zone (we considered depth shift between Holes C0004B and C0004D) shows that conductive fractures are relatively concentrated in these intervals (see the “Expedition 314 Site C0004” chapter). The presence of conductive fractures and/or highly deformed material associated with the concentrated shear may have caused poor recovery at these intervals.

## Biostratigraphy

Two holes were drilled at Site C0004 on the shallow portion of the megasplay fault system during Expedition 316. Hole C0004C was cored from the seafloor to 134.97 m CSF through the slope sediments into the upper part of the accretionary prism. Hole C0004D was cored from 100.00 to 398.79 m CSF from the upper part of the accretionary prism through its lower boundary into the underthrust slope sediments below.

Biostratigraphy was determined for Site C0004 based on examination of calcareous nannofossils, radiolarians, and foraminifers. A few samples were additionally analyzed for diatoms.

### Calcareous nannofossils

All core catcher samples plus additional samples from some critical intervals in the vicinity of zonal boundaries were examined for calcareous nannofossils at Site C0004. Calcareous nannofossils from slope sediments are generally abundant and moderately preserved, whereas those from the accretionary prism sediments and the underthrust slope sediments are low in abundance and moderately to mostly poorly preserved (Tables T6, T7).

In Hole C0004C, a total of 10 nannofossil biostratigraphic events were recognized (Table T8). *Pseudoe-miliania lacunosa* was absent in Sample 316-C0004C-1H-CC, 0–5 cm (6.27 m CSF) but occurs in Sample 2H-CC, 0–5 cm (16.33 m CSF); therefore, the last occurrence (LO) of *P. lacunosa* is located between 6.27 and 16.33 m CSF, marking the boundary between nannofossil Zones NN20 and NN19. Zone NN19 was

further subdivided by four events: the last consistent occurrence (LCO) and first consistent occurrence (FCO) of *Reticulofenestra asanoi* and the LO and FCO of *Gephyrocapsa* spp. large (>5.5  $\mu$ m) (Table T8). Among these events, the FCO of *Gephyrocapsa* spp. large (>5.5  $\mu$ m) (1.46 Ma) was assigned between Samples 316-C0004C-8H-CC, 23.5–28.5 cm, and 9H-2, 94 cm (73.64–75.23 m CSF). The bottom of the FCO of *Gephyrocapsa* spp. was truncated by a number of late Pliocene–early Pleistocene events:

- The LO of *Calcidiscus macintyreii* was recorded in the same sediment interval (73.64–75.23 m CSF) as the FCO of *Gephyrocapsa* spp. large (>5.5  $\mu$ m).
- The interval below, from 75.23 to 78.86 m CSF, was barren of nannofossils.
- LOs of *Discoaster brouweri* (marker of Zone NN18) and *Discoaster pentaradiatus* (marker of Zone NN17) occur in common abundance between Samples 316-C0004C-9H-6, 17 cm, and 9H-6, 44 cm.
- *Discoaster surculus* (marker of Zone NN16) was observed between Samples 9H-6, 17 cm, and 9H-CC, 0–5 cm (79.03–80.87 m CSF) (Table T8).

That is, the lower part of lower Pleistocene Zone NN19 and upper Pliocene Zones NN18 and NN17 were missing in the interval, indicating a significant unconformity (with a time difference of ~1 m.y.) in the interval from 74.44 to 80.87 m CSF, which is compatible with results from magnetostratigraphy in the same hole (see “Paleomagnetism;” Fig. F29). This unconformity, indicated by nannofossil events, can be correlated to the upper boundary of the upper slope deposits, indicated by seismic profile in the same hole. The sediment interval from below 80.87 m CSF to the bottom of Hole C0004C was assigned to middle Pliocene Zone NN16, based on the occurrence of *D. surculus*. The LO of *D. tamalis* (2.87 Ma) was identified between Samples 316-C0004C-11H-CC, 0–5 cm, and 12H-CC, 0–5 cm (89.23–98.51 m CSF) (Table T8).

In Hole C0004D, reworked nannofossils are common throughout the sediment samples obtained, leading to difficulty in recognizing nannofossil events and zones. For example, middle Pliocene zone markers *Discoaster asymmetricus* (base marker of Zones NN15–NN14), *Ceratolithus rugosus* (marker of Zone NN13), and *Ceratolithus acutus* (rare but important species occurring just below and above the Zone NN12/NN13 boundary) are observed nearly continuously in the upper slope sediment sequences (Table T7).

A total of 13 nannofossil biostratigraphic events were recognized for age and depth correlation in Hole C0004D (Table T9; Figs. F30, F31). The upper

part of the sediment sequence to Sample 316-C0004D-19H-CC, 0–5 cm (226.98–227.03 m CSF), was assigned to middle Pliocene calcareous nannofossil Zone NN16, based on the co-occurrence of *D. surculus* (marker of top of Zone NN16) and *D. tamalis*, as well as on the absence of *Sphenolithus* spp. and *Reticulofenestra pseudoumbilicus* ( $>7\ \mu\text{m}$ ) (top marker of Zones NN15–NN14) (Table T9; Fig. F30). Trace occurrences of these two species in a few samples in this interval were considered to be due to reworking. The frequent to common occurrence of *R. pseudoumbilicus* ( $>7\ \mu\text{m}$ ) between the interval from 228.80 to 256.79 m CSF (Samples 316-C0004D-20H-CC, 0–5 cm [228.77–228.82 m CSF], through 25R-1, 79 cm [256.79 m CSF]) marked the short middle interval of Hole C0004D as upper lower Pliocene Zones NN15–NN14. In this interval, *Sphenolithus* spp. (LO just above the top of Zone NN15) occurs frequently to commonly. *D. asymmetricus* (base marker of Zones NN15–NN14 with first occurrence [FO] at 4.13 Ma) occurs continuously in this interval (Table T7), suggesting the sediments at the bottom of this interval are younger than 4.13 Ma (Fig. F30).

Sample 316-C0004D-25H-CC, 0–5 cm (257.72–257.75 m CSF), was barren of nannofossils. The interval from below this sample to 292 m CSF (Sample 316-C0004D-33R-1, 20 cm) lacked frequent occurrences of *Sphenolithus* spp. and *R. pseudoumbilicus* ( $>7\ \mu\text{m}$ ); however, this interval had occurrences of *D. surculus* and *D. tamalis* and therefore was assigned to Zone NN16. The age of the bottom of this interval was estimated between 3.65 and 2.87 Ma, based on the absence of *Sphenolithus* spp. (LO = 3.65 Ma) and the presence of *D. tamalis* (LO = 2.87 Ma) (Table T7). There is an age gap between Zones NN15–NN14 sediments and underlying Zone NN16 sediments in the interval between ~256.79 and 260.69 m CSF (Fig. F30). The reentry of Zone NN16 below sediments of Zones NN15–NN14 suggests a sequence reversal or disturbance of normal sediment sequences caused by faulting. The location of this age reversal is consistent with the top of lithologic Unit III, the fault-bounded unit (see “Structural geology”).

The determination of zonation or subdivision for the interval from Samples 316-C0004D-33R-CC, 0–5 cm (296.06–296.11 m CSF), through 36R-CC, 0–5 cm (307.47–307.52 m CSF), was impossible during the cruise because samples observed contained a mixture of Pleistocene and Pliocene nannofossils in various degrees or were barren of nannofossils. Sediments within this interval are fractured and brecciated (see “Structural geology”).

The lower part of the sediment sequence of Hole C0004D to the bottom of the hole (from Sample 316-C0004D-37R-1, 17 cm [310.16 m CSF], to the

bottom of the hole) was assigned to Pleistocene Zone NN19 because of the frequent to common occurrence of various sized Pleistocene *Gephyrocapsa* spp., such as *Gephyrocapsa* spp. large ( $>5.5\ \mu\text{m}$ ) and *Gephyrocapsa* spp. medium I and medium II. The FO of *Gephyrocapsa* spp. large ( $>5.5\ \mu\text{m}$ ) (1.560–1.617 Ma) can be placed between Samples 316-C0004D-40R-CC, 4.0–9.0 cm (325.43–325.48 m CSF), and 41R-CC, 0–5 cm (330.37–330.42 m CSF). This further provides an estimation of the age for the top of the lowest sequence of lithologic Unit IV: between 1.46 Ma (FCO of *Gephyrocapsa* spp. large [ $>5.5\ \mu\text{m}$ ]) and 1.560–1.617 Ma, indicating the lower part of Hole C0004D is in the range of lower Zone NN19 (Fig. F30).

The occurrence of Zone NN19 below both Zone NN16 and the zone containing a mixture of Pleistocene and Pliocene nannofossils implies a significant age reversal. This event is in good agreement with the lower boundary of the thrust fault suggested by seismic reflection profile and LWD in the same hole and a fractured/brecciated zone of Unit III (see “Structural geology” and “Lithology”). The age difference for the age reversal is ~2.05 m.y. (Fig. F30).

## Other microfossil groups

Radiolarians, diatoms, and foraminifers occur in variable abundances and preservation throughout the upper part of the hole (Unit I and Subunit IIA). Sediments retrieved from the lower part (Subunit IIB to Unit IV) contain only rare microfossils. Radiolarians and diatoms are reworked or are barren. Although all core catchers were processed and radiolarians were checked throughout the hole, only the upper part appeared to be reliable for biostratigraphic analysis (Fig. F31).

## Radiolarians

Radiolarians are common to abundant and moderately to well preserved in the upper part of the sequence in Hole C0004C (until Section 316-C0004C-7H-CC). In this interval (Unit I and Subunit IIA), three biozones were identified. The appearance of *Stylatractus universus* in Sample 316-C0004C-2H-CC assigns the upper interval to the *Botryostrobus aquilonaris* Biozone. The association of *Lamprocyrtis heteroporos* and *Pterocanium praetextum* in Sample 316-C0004C-6H-CC was assigned to the *Eucyrtidium matuyamai* Biozone. This zone can be extended to the base of lithologic Unit I, although diagnostic radiolarian taxa are not available to confirm this.

Deeper samples (Units II and III) contain rare and nondiagnostic specimens or are barren. In this interval, preservation is moderate to poor and spongy and fragments of highly silicified radiolarian shells

dominate the assemblages, which are often undiagnostic for radiolarian zonation.

Preliminary results on the preservation of radiolarian shells (highly silicified and spongy specimens) seem to show their preservation is significantly different in the four lithologic units (Fig. F31). Unit I contains undamaged shells with only a few broken specimens, whereas shell preservation varies between well preserved and poorly preserved in Subunit IIA and Unit IV. Only a few poorly preserved radiolarian shells were found in Subunit IIB. In Unit III, radiolarians are well preserved and even fragile shells are found. Although a more detailed analysis (e.g., scanning electron microscope [SEM] imaging and opal diagenesis data) is needed and more samples have to be checked, there is an obvious difference in preservation among these four lithologic units, probably because of the surrounding chemical composition (e.g., silica in pore water, sediment content) and the burial depth.

### Diatoms

For this site, diatom analysis was attempted only in Unit I and in a few critical intervals as reference for nanofossil determinations in Units II and III.

Diatoms in Unit I appeared to be well preserved, although breakage is common. Most of the retrieved diatoms were undiagnostic for zonation purposes, although the LO of *Nitzschia reinholdii* was recognized in the interval between Samples 316-C0004C-2H-CC and 3H-CC.

Throughout the hemipelagic interval, diatom assemblages are composed of coastal (e.g., *Actinoptycus senarius*) and open-ocean species, mainly from warm-water environments. *Thalassionema nitzschoides* and *N. reinholdii* are ubiquitous taxa within their biostratigraphic interval, and *Coscinodiscus radiatus*, a large taxa characteristic of warm-water environments, was systematically found within the radiolarian size fraction (>63  $\mu\text{m}$ ). Below Sample 316-C0004C-9H-CC, diatoms (>63  $\mu\text{m}$ ) are absent or strongly reworked.

### Summary

Unit II and III prism sediments in the megasplay fault system are of early–middle Pliocene age (from Zone NN16 to Zones NN15–NN14). Sediments above and below the prism are Pleistocene sequences (upper Pleistocene sediments above the prism and lower Pleistocene sediments below it), based on nanofossil data from Holes C0004C and C0004D. Plots of age and depth for upper Pleistocene slope sediments in Hole C0004C were combined with results from mag-

netostratigraphy in the same hole (see “Paleomagnetism;” Fig. F29).

Three significant age gaps were recognized in the shallow portion of the megasplay fault system. The unconformity (with time difference of ~1 m.y.) at ~78–79 m CSF in Hole C0004C indicates the boundary of the slope sediments and the top of Unit II (Fig. F29). The second age gap occurs in Hole C0004D in the interval between lower–middle Pliocene Zones NN15–NN14 and the reentry of middle Pliocene Zone NN16 (from about >256.79 to <260.69 m CSF). The most significant age gap and reversal occurs in Hole C0004D between middle Pliocene Zone NN16 and Pleistocene Zone NN19 and can be correlated to the lower boundary between Units III and IV. The time difference for this age reversal was estimated as ~2.05 m.y. (Fig. F30).

## Paleomagnetism

Shipboard paleomagnetic studies for Site C0004 consisted of continuous measurements of archive half core sections and progressive demagnetization measurements of discrete samples in a similar fashion to that performed during Expedition 315 (see “Paleomagnetism” in the “Expedition 315 Site C0001” chapter). A total of 16 discrete samples were stepwise thermally or alternating-field (AF) demagnetized to evaluate the directional stability and coercivity/unblocking temperature spectra of each sample. The anisotropy of magnetic susceptibility (AMS) was measured on seven discrete samples with the Kappa-bridge KLY 3. Volume magnetic susceptibility of these discrete samples was measured before the AMS measurement. The Königsberger ratio was also determined for these samples.

### Natural remanent magnetization and magnetic susceptibility

Within the recovered sediments, there are considerable variations in magnetic properties and demagnetization behavior among the various lithologies. The most important observations at Site C0004 are summarized below.

Natural remanent magnetization (NRM) intensities of the archive halves from Holes C0004C and C0004D span more than two orders of magnitude (ranging from 0.02 to >80 mA/m; Fig. F32). NRM intensity peaks at 352.7 m CSF (Sample 316-C0004D-46R-2, 80 cm), corresponding to the silty clay with volcanic sand layers (see “Lithology”). Variations in magnetic susceptibility are consistent with variations in NRM intensity (see Fig. F32 for an example). Magnetic susceptibility values are generally  $\sim 10 \times 10^{-3}$

SI for the upper slope sediment Unit I, prism Subunit IIB, and fault-bounded Unit III but significantly higher ( $>50 \times 10^{-3}$  SI) for the underthrust slope sediment deposits in Unit IV, which contain volcanic and sand layers (see “[Lithology](#)”). Magnetic susceptibility rapidly decreases and then increases within Sections 316-C0004C-9H-5 (~78 m CSF) and 15X-1 (~118 m CSF), marking the beginning and end of the breccia observed in Subunit IIA. These susceptibility variations were verified by further measurements of corresponding discrete samples (see “[Anisotropy of magnetic susceptibility](#)”).

Pervasive remagnetization imparted by the coring process is commonly encountered, as noted during previous Deep Sea Drilling Project/ODP/IODP legs (e.g., Gee et al., 1989; Zhao et al., 1994). This remagnetization is characterized by NRM inclinations that are strongly biased toward vertical (mostly toward  $+90^\circ$ ) in a majority of cores. As shown in Figure [F32](#), with AF demagnetization to 40 mT a significant decrease in intensity and a shift of inclination toward shallower or negative values were observed for intervals with normal or reversed polarity, respectively, suggesting the presence of drilling-induced remagnetization. In two intervals (~350 and 370 m CSF) where recovered sediments are dominated by hemipelagic silty clay with sand layers, however, remagnetization appears to have only affected inclination and to have little effect on NRM intensity (Fig. [F32](#)).

The most diagnostic feature in the paleomagnetic data obtained at Site C0004 is that changes in magnetic polarity can be correlated with changes in biostratigraphic zonations. For example, the uppermost 15 m of sediments at Hole C0004C is known to be of Pleistocene age, based on biostratigraphic age markers (Zones NN20–NN19,  $>0.291$  and  $<0.9$  Ma). Therefore, the normal polarity of Cores 316-C0004C-1H through 2H suggests that these sediments were deposited during the Brunhes Chron (i.e.,  $<0.781$  Ma). In the lower part of Hole C0004D, sediments between 314.6 m CSF (Sample 316-C0004D-38R-1, 12 cm) and 398.8 m CSF (Sample 56R-CC, 14 cm) show reversed polarity. Biostratigraphic Zone NN19 with well-defined FO events is also placed at the beginning of this interval, suggesting the reversed polarity should correlate with the Matuyama Chron. In addition, biostratigraphic data suggest that sediments below 398 m CSF (Sample 316-C0004D-56R-CC, 14 cm) may be  $<2$  Ma. This information is in good agreement with paleomagnetic observations and suggests that the shift of polarity from reversed to normal at ~390 m CSF should correspond to the beginning of the Olduvai Subchron (C2n; 1.778–1.945 Ma).

## Paleomagnetic stability tests and general polarity sequences

Because of the rotary technique used for drilling in Hole C0004D, relative rotation frequently occurred between different segments of sediment within the core. This may cause apparent changes in the declination of stable remanent magnetization. Consequently, magnetic polarity has been assigned on the basis of the inclination of the stable remanent magnetization. As Site C0004 is situated at moderate latitude in the Northern Hemisphere, positive (downward directed) inclinations are taken to signify normal polarity and negative (upward directed) inclinations signify reversed polarity. NRM was measured at 5 cm intervals for each core section, followed by AF demagnetization at 5, 10, 20, and 40 mT peak fields. In most cases, an unambiguous polarity determination of the stable component of magnetization was achieved after the 40 mT treatment. Figure [F33](#) illustrates the stable behavior of several samples; this behavior demonstrates the removal of a normal component of magnetization and the isolation of a more stable reversed component that univectorially decays toward the origin of the vector plots (Zijderveld, 1967). Because the maximum level of AF demagnetization on the ship’s cryogenic magnetometer was not always able to remove remagnetization, several discrete samples were stepwise thermally or AF demagnetized (Fig. [F33](#)). An example of demagnetization behavior of a sample during thermal demagnetization is illustrated in Figure [F33C](#). A secondary component of magnetization was removed at low temperatures ( $200^\circ\text{C}$ ), and a characteristic remanent magnetization (ChRM) component having higher unblocking temperatures could be identified. The response of ChRM to AF and thermal demagnetization suggests that ChRM in most samples is carried by fine (i.e., single-domain to pseudosingle-domain) low-Ti titanomagnetite grains.

Demagnetization of core sections sometimes showed antipodal relative declinations within the same piece of core section (Fig. [F34](#)). After AF demagnetization at 40 mT, the reversal indicated by the difference in polarity of inclination was confirmed by the near  $180^\circ$  change in declination. This positive “antipodal test” is perhaps the most compelling argument for isolating primary ChRM, although this test is not sufficient by itself. We also noticed that the inclination values of ChRM are moderately downward or upward consistent with the expected inclination for the site ( $52.6^\circ$  for normal polarity or  $-52.6^\circ$  for reversed polarity).

A number of pass-through measurements, however, have inclinations that do not resemble the time-averaged geomagnetic field (expected inclination =

$\pm 52^\circ$ ). In particular, Cores 316-C0004C-2H through 18H (~15–134 m CSF) and Cores 316-C0004D-1R through 13R (~105–180 m CSF) have remanent inclinations that are consistently shallower ( $\pm 20^\circ$ – $30^\circ$ ) than predicted. Shipboard studies revealed that the sedimentary layers may have tilted after formation (see Fig. F35). Assuming the regional strike for the sedimentary sequence is northeast–southwest with dips ranging from  $40^\circ$  to  $60^\circ$ , a moderate tilt correction ( $\sim 45^\circ$ ) along a northeast fold axis would restore these shallow inclinations to the expected dipole inclination at Site C0004. Another possible explanation is that drilling-induced remagnetization was not completely removed from the recovered sediments, and therefore these sediments do not necessarily have an inclination corresponding to that expected from a geocentric axial dipole.

The magnetostratigraphy at Site C0004 indicates several magnetic reversals that may be discerned on the basis of changes in sign of inclinations on cores from Holes C0004C and C0004D (Fig. F36; Table T10). Each of the major polarity zones in Figure F36 is defined by several measurements of the same polarity. On the basis of shipboard micropaleontological data, the uppermost 15 m of sediment in Hole C0004C is Pleistocene in age. Therefore, the normal polarity of Core 316-C0004C-1H suggests that these sediments were deposited during the Brunhes Chron. The first evidence for reversed magnetization occurs at 6.73 m CSF in Section 316-C0004-2H-1, 55 cm, which may correspond to the Emperor event (0.42 Ma; see Gradstein et al., 2004). The Brunhes/Matuyama Chron boundary (0.78 Ma) is placed at 15.87 m CSF, as the magnetic inclination at this depth changes polarity from normal to reversed. Sediments between 17.92 and 40.18 m CSF show normal polarity, indicating that the Jaramillo Subchron (0.99–1.07 Ma) may be recorded in these sediments and implying a relatively rapid sediment accumulation rate. Biostratigraphic marker *R. asanoi* (0.9–1.078 Ma) is also placed in this depth interval (see Fig. F29). Below 40.99 m CSF, the dominantly reversed polarity correlates well with the Matuyama reversed polarity chron. This dominantly reversed polarity sequence extends to 102.20 m CSF. Biostratigraphic data suggest that the sediments below 98.51 m CSF (Sample 316-C0004C-12X-CC, 5 cm) are older than 2.52 Ma but younger than 3.65 Ma. This information suggests that the shift of polarity from reversed to normal at ~102 m CSF should correspond to the Matuyama/Gauss boundary (2.58 Ma). Within the sequence assigned to the Matuyama reversed chron, one apparently thin normal polarity zone is present in the depth range of 50.78–54.20 m CSF in Hole C0004C and at 356.68 m CSF in Hole C0004D. This short normal polarity zone appears to correspond to the

Olduvai Subchron (1.77–1.95 Ma). Key nannofossil markers around this depth in both Holes C0004C and C0004D are in good agreement with the paleomagnetic data, suggesting that these sediments span the Pliocene/Pleistocene boundary (Zone NN19a). Below the Matuyama/Gauss boundary, a dominantly normal polarity sequence extends to at least the bottom of Hole C0004C at 135.00 m CSF (Fig. F36). This dominantly normal polarity sequence should correspond to the Gauss normal chron. Unfortunately, sedimentary sequences in Hole C0004D are structurally disrupted with several age-reversed intervals. Consequently, these age-reversed intervals prevent us from constructing a magnetostratigraphy older than the Gauss Chron.

Paleomagnetic and biostratigraphic age determinations are compatible with each other in Hole C0004C (Fig. F29). This compatibility allows a determination of sedimentation rates and a better definition of the times at which significant changes in sedimentation rate occurred.

### Paleomagnetically determined sedimentation rates for Hole C0004C

Pleistocene and Pliocene sediments cored in Hole C0004C yielded a preliminary magnetic polarity stratigraphy (Fig. F36; Table T10) and age-depth profile (Fig. F29) from which preliminary sedimentation rates can be calculated. The Brunhes/Matuyama (0.78 Ma), Jaramillo (0.99–1.07 Ma), Olduvai (1.77–1.95 Ma), and Matuyama/Gauss (2.58 Ma) chrons are tentatively determined at depths of 15.87, 17.92–40.18, 50.78–54.20, and 102.20 m CSF, respectively. If correct, these calibration points allow the determination of sedimentation accumulation rate values and the assignment of “absolute” ages to the biostratigraphic zonal boundaries identified in Hole C0004C. The lower Pliocene–Holocene sediment accumulation rates at Site C0004C are 20.4 m/m.y. for the middle Pleistocene and 39.6 m/m.y. for the late Pliocene. Furthermore, if the identification of the Olduvai Subchron is correct, a decrease in accumulation rate or a short hiatus is inferred within the interval of 1.77–1.95 Ma.

### Anisotropy of magnetic susceptibility

AMS measurements were carried out on discrete samples from the area of special scientific interest to inspect magnetic properties and fabrics. Seven samples were collected across the unconformity in Section 316-C0004C-9H-5, which forms a boundary between Unit I and Subunit IIA, upper slope sediments and upper prism. Although the equipment (AGICO Kappabridge KLY 3) is so sensitive that it is barely stable onboard because of the movement of the vessel, we

accomplished the analyses with low error values. Magnetic susceptibility of the samples was measured in various orientations and resulted in a magnetic ellipsoid with three principal axes from maximum (K1) to minimum (K3). Parameters of anisotropy degree and shape parameter are expressed as

$$L = K1/K2$$

and

$$F = K2/K3,$$

respectively.

Bulk magnetic susceptibility showed a significant decrease below the unconformity, which is consistent with the results of continuous whole-core logging using the multisensor core logger (MSCL) (Table T11). Although  $L$  and  $F$  values vary in the hanging wall in ranges of  $1.002 < L < 1.024$  and  $1.010 < F < 1.030$ , measurements in the footwall are relatively low and stable ( $1.003 < L < 1.007$  and  $1.003 < F < 1.012$ ). With such low  $L$  and  $F$  values, three principal axes of magnetic ellipsoids have only little variation so that the shapes of the ellipsoids are close to spherical. Even the results do not show significant preferences; a small variance in the hanging wall possibly indicates some structural disturbance or mineralogical difference from the foot wall. Further onshore study is required to make this question clear.

As shown in Table T11, the decrease in magnetic susceptibility and intensity at the unconformity might indicate some mineralogical change of magnetic carrier. The hanging wall consists of silty clay, whereas the footwall consists of green brecciated silty clay. Shipboard XRD measurements revealed that breccia below the unconformity contains a slightly higher iron component (see “Lithology” for details), which is not consistent with magnetic data. Resolution of this discrepancy will require further detailed mineralogical investigations.

The Königsberger ratio,  $Q$ , is defined as the ratio of remanent magnetization to the induced magnetization in Earth’s magnetic field. In general, the Königsberger ratio is used as a measure of stability to indicate a rock’s capability of maintaining a stable remanence. The International Geomagnetic Reference Field (IGRF) value at Site C0004 ( $45,706 \text{ nT} = 36.39 \text{ mA/m}$ ) was used for calculating the Königsberg ratio ( $Q$ ):

$$Q = J_{\text{nm}} [\text{mA/m}] / [K_{\text{m}} (\text{SI}) \times H (\text{mA/m})],$$

where

$H$  = local geomagnetic field,  
 $K_{\text{m}}$  = bulk susceptibility, and

$J_{\text{nm}}$  = NRM intensity.

Results show that  $Q$  ratios in a majority of samples are  $<1$ , suggesting that the total magnetization of the sediments contains dominantly induced magnetization. The relatively low  $Q$  ratios may also explain the pervasive drilling-induced remagnetization imparted to these cores.

In sum, preliminary shipboard paleomagnetic data revealed important magnetic signatures that await further verification in terms of age and origin. Further integrated work with biostratigraphic and structural studies is required to constrain the timing and origin of magnetization recorded by the Site C0004 sediments.

## Inorganic geochemistry

The main objectives of the geochemical program at Site C0004 are to

- Characterize in situ biogeochemical reactions.
- Constrain in situ inorganic diagenetic reactions with depth.
- Identify potential fluids derived from depth within the fault zone and within other permeable horizons as well as fluid-sediment reactions.
- Constrain the subsurface hydrology, including fluid flow pathways and possible transport mechanisms.

A host of diagenetic reactions occur within the temperature range that coincides with the updip limit of the seismogenic zone ( $\sim 80^{\circ}$ – $175^{\circ}\text{C}$ ). These reactions include the opal–quartz transition, the smectite–illite transition, albitization, and desorption of cations from clays, as well as cementation by carbonate, clay, and zeolite. At higher temperatures and pressures within the seismogenic zone, a suite of hydrous metamorphic minerals, such as chlorite, serpentine, and amphiboles, form and break down, releasing fluids and altering the pore fluid composition. Fluid chemistry is predictably altered with increasing temperature and pressure and, assuming fluid–mineral equilibrium at various temperatures, can facilitate estimation of the depth of fluid sources, thus constraining the role of in situ diagenetic reactions and deeper sourced reactions in fluid production within fault zones. Characterizing these in situ fluid–rock reactions and identifying fluids migrating from depth are critical to understanding the hydrogeologic behavior of the splay fault system and constraining the processes of slip along this boundary.

A total of 41 whole-round samples were collected for interstitial water analyses at Site C0004 (18 from Hole C0004C and 23 from Hole C0004D). Whole-round lengths ranged from 21.5 to 43 cm with larger

subsamples collected from cores recovered deeper within the hole where sediments were more consolidated (see “**Physical properties**”). Samples were collected in Hole C0004C at a higher spatial resolution than in Hole C0004D to better define the sulfate-methane transition (SMT) and to identify and quantify the anaerobic oxidation of methane (AOM) magnitude at this site, as well as for future geochemical and microbiological studies. In Hole C0004C, two samples were collected per core for Cores 316-C0004-1H through 3H, which span the depths ranging from the sediment/water interface to ~8 m below the SMT. Below this depth, one sample was taken per core. Only one sample was taken per core to TD in Hole C0004D. Because of poor core recovery in lithologic Subunits IIA and IIB, we were unable to take interstitial water samples from cores that were <1 m long. Because of the brecciated nature of the sedimentary material in Subunit IIA and Unit III (see “**Structural geology**”), some cores were extremely difficult to clean prior to processing. This difficulty is observed in the elevated  $\text{SO}_4$  concentrations (Table T12), which show that a significant portion of the interstitial water samples were contaminated with surface seawater during drilling operations. All of the contaminated samples were collected below the SMT, where in situ  $\text{SO}_4$  concentrations are expected to be zero. These samples were corrected for drill water contamination based on measured  $\text{SO}_4$  concentrations using the procedure and equations outlined in the “**Inorganic geochemistry**” section of the “Expedition 316 methods” chapter. Uncorrected concentrations of all of the elements analyzed are presented in Tables T12, T13, and T14, and the corrected values for the major and minor elements are presented in Tables T15 and T16. Only corrected values are presented in figures.

### Salinity, chloride, and sodium

Pore fluid salinity decreases nearly monotonically from 34.5 at 2.6 m CSF to 33.3 at 29.5 m CSF (Fig. F37A). The salinity decrease in the upper ~30 m of the sediment section reflects active sulfate reduction and subsequent precipitation of authigenic carbonates consuming pore fluid  $\text{SO}_4$ , Ca, and Mg in this interval (Fig. F38A, F38B, F38C, F38D). Salinity then increases sharply to 35.9 at 114.0 m CSF near the base of Subunit IIA. Pore fluid salinity varies in Subunit IIB and Units III and IV. Salinity slightly decreases at the base of the fault zone in Unit III (Fig. F37A) and just below the fault zone at 350 m CSF, after which it steadily increases to 36.06 at 393.6 m CSF (TD).

Chloride increases steadily from near-seawater value at 2.6 m CSF to 642 mM (~15% greater than modern seawater value) at the base of Subunit IIA. The rate of

increase in Cl lessens in Subunit IIB, and Cl slightly increases below the fault zone in Unit IV to 649 mM (~17% greater than seawater value) at 393.6 m CSF.

A significant amount of volcanic ash was recovered from Units I, III, and IV at this site (see “**Lithology**”). In these intervals, ash layers >13 cm thick were recovered, and as much as 20% ash was disseminated within both the fine-grained sediment and silty clays. Thus, the steady downhole increase in Cl at Site C0004 likely reflects in situ ash alteration where water is consumed during the formation of authigenic clays and zeolites. There was relatively little ash in Subunit IIB between 140 and 250 m CSF, which is the same interval where Cl remains relatively constant (Fig. F37B).

Dissolved sodium follows the same trend as Cl (Fig. F37C). However, the rate of increase in Na is greater than that of Cl through all three lithologic units (Na/Cl plot, Fig. F37D). This discrepancy is consistent with ash alteration, where Na is partitioned into the fluid phase during ash dissolution and authigenic mineral formation. There are four peaks in Na/Cl in Subunit IIB and Unit III at ~180, 250, 307, and 344 m CSF. Three of these peaks occur slightly above, within, and ~29 m below the main fault zone (Unit III). These maxima indicate addition of Na within these intervals.

### Pore fluid constituents controlled by microbially mediated reactions

#### Sulfate and alkalinity

Sulfate decreases linearly from 25.31 mM at 2.7 m CSF to 17.19 mM at 5.5 m CSF (Fig. F38A, F38F). The slope of the sulfate reduction profile then increases to 9.1 m CSF. Sulfate decreases steadily from 13.9 m CSF to below the detection limit at ~20 m CSF. A concomitant increase in headspace methane at ~16 m CSF constrains the depth of the SMT at ~16–20 m CSF (Fig. F38F). Below the SMT, sulfate remains depleted except for excursions up to 10 mM in Subunit IIB and Unit III (Table T15). These units are highly brecciated, and these excursions represent contamination of the whole-round samples collected for interstitial water analyses by seawater circulating in the borehole during drilling. Sulfate concentrations from these units were used to correct the interstitial water data for drilling contamination (see “**Inorganic geochemistry**” in the “Expedition 316 methods” chapter) (Tables T15, T16).

Pore fluid alkalinity rapidly increases downhole in the upper part of Unit I; a maximum of 18.3 mM occurs just below the SMT at 22.9 m CSF. Below the SMT, alkalinity decreases with depth to 7.6 mM at 393.6 m CSF. Superimposed on the steady decrease

in alkalinity are a maximum (15.6 mM) at 179.5 m CSF and a minimum (8.1 mM) in the fault zone at 282.2 m CSF. Alkalinity at and near the SMT is much lower than values expected from either AOM or organic matter degradation by sulfate reduction (Fig. F38B). Ca reaches a minimum at the depth of the SMT, and Mg decreases in the sulfate reduction zone (Fig. F38C, F38D). The decreases in Ca and Mg in the sulfate reduction zone indicate active precipitation of authigenic Mg-calcite, which consumes pore fluid alkalinity at and near the SMT. Dissolved Mn also decreases rapidly in this interval and becomes essentially depleted at the SMT, suggesting minor precipitation of authigenic rhodochrosite at this depth (Fig. F39D).

### Ammonium, phosphate, bromide, and manganese

Dissolved ammonium increases monotonically with depth through Unit I to ~200 m CSF (Fig. F39A). Below this depth, ammonium varies, ranging from 4662 to 8343  $\mu\text{M}$ . The steady ammonium increase in the upper ~180 m indicates production by microbially mediated decomposition of organic matter fueled by sulfate reduction above the SMT. Below the SMT, Mn oxides and oxyhydroxides are likely the terminal electron acceptors for organic matter oxidation based on the progressive increase in dissolved Mn through this depth interval (Fig. F39D). Ammonium concentration is variable above, within, and just below the fault zone (Unit III).

Bromide in marine interstitial waters is sensitive to organic matter diagenesis; concentrations higher than seawater reflect marine organic matter decomposition. For this reason, Br profiles are similar to dissolved ammonium profiles. Br increases from 0.89 mM at 2.7 m CSF to 1.20 mM at 126.2 m CSF, coincident with the base of Subunit IIA (Fig. F39C). Below this depth, Br increases gradually to 1.24 mM at 393.6 m CSF. There are no major variations in the Br profile in the splay fault zone (Unit III). The Br profile at this site reflects decomposition of marine organic matter with a greater rate of Br input from marine organic matter decomposition above 130 m CSF and more uniform values below this depth.

Phosphate increases rapidly in Unit I, reaching a maximum of 55.4  $\mu\text{M}$  at 39.2 m CSF, below which phosphate decreases before increasing moderately at the top of the main fault zone. The phosphate increase in the upper 30 m reflects active organic matter decomposition in the active sulfate reduction zone. Manganese concentration is above seawater value in the upper 5 m of the sediment column, reflecting  $\text{MnO}_2$  reduction during microbially mediated organic matter degradation. Mn becomes totally

depleted at the SMT, which is likely due to authigenic rhodochrosite precipitation at the alkalinity maximum. Below this depth, Mn increases as a result of progressive organic matter degradation, with maxima within and near the main fault zone.

### Major cations (Ca, Mg, and K)

Calcium monotonically decreases from 8.57 mM at 2.7 m CSF to 3.12 mM at 22.9 m CSF, which coincides with the depth of sulfate depletion and the alkalinity maximum (Fig. F38C). Between the seafloor and the SMT, Ca is consumed by active precipitation of authigenic carbonates, which also consumes pore fluid alkalinity. From 22.9 to 276.8 m CSF, Ca steadily increases to 8.55 mM. Below this depth, Ca remains relatively constant to TD. Increasing Ca with depth is consistent with progressive ash alteration downhole. There are no major anomalies in the Ca profile in the main fault zone at this site.

Magnesium decreases sharply from 47.8 mM at 2.7 m CSF to 38.0 mM at 22.9 m CSF (Fig. F38D). This zone of rapid Mg depletion coincides with the  $\text{SO}_4$  reduction zone and the SMT, indicating active precipitation of Mg with authigenic carbonates in this depth interval, as well as uptake during ash alteration. Mg then steadily decreases from 22.9 m CSF to 16.5 mM at 393.6 m CSF. Superimposed on this gradual Mg decrease are three minima at 248.0, 306.8, and 344.0 m CSF. These three depths are coincident with zones of deformation above, within, and below the splay fault zone at this site. The general decrease in Mg likely indicates Mg uptake in hydrous silicate minerals (mainly clays) formed during volcanic ash alteration.

The dissolved potassium profile can be split into two zones. The first zone, from the seafloor to 153.1 m CSF, is characterized by K concentrations higher than modern seawater value in the upper ~40 m and then approximately at seawater value to 153.1 m CSF (Fig. F40E). Elevated K values in the upper 40 m are likely due to sampling artifacts related to the pressure change during core recovery or to cation exchange with  $\text{NH}_4$  on clay mineral surfaces during the early stages of organic matter degradation and ammonium production. From 40.0 to 153.1 m CSF, K decreases with local minima, though ammonium remains elevated, indicating authigenic zeolite formation during the alteration of volcanic ash. The second zone in the K profile extends from 153.1 m CSF to TD, where K gradually decreases to 8.2 mM at 393.6 m CSF. The steady potassium decrease is due to progressive K uptake by zeolites formed during ash alteration. Superimposed on the steady K decrease are three minima at 248.0, 306.8, and 344.0 m CSF that coincide with the three Mg minima.

## Minor elements (B, Li, H<sub>4</sub>SiO<sub>4</sub>, Sr, and Ba)

Boron decreases relatively sharply within Unit I and Subunit IIA from 498  $\mu\text{M}$  at 2.7 m CSF to 228  $\mu\text{M}$  at 126.0 m CSF, with local minima at the base of Unit I and in Subunit IIA (Fig. F40A). Boron decreases less rapidly with depth in Subunit IIB and Units III and IV, reaching ~193–216  $\mu\text{M}$  at TD (~55%–60% less than modern seawater value). This steady B decrease with depth reflects ash alteration, mainly B uptake in authigenic clay minerals. The slope change of the B profile at the base of Subunit IIA is consistent with this interpretation, as the relative abundances of disseminated and massive ash layers decrease within this unit (see “[Lithology](#)”).

Lithium initially decreases from a near-seawater value at the top of Unit I to 21.8  $\mu\text{M}$  at 48.6 m CSF. Li then increases steadily to 125  $\mu\text{M}$  at 227.0 m CSF (~25 m above the fault zone). Below this depth, Li decreases to 44.4  $\mu\text{M}$  at TD (393.6 m CSF). Li depletion in the uppermost 50 m of Unit I is consistent with volcanic ash alteration. The broad concentration peak above the main fault zone is not observed in any other element profiles collected at Site C0004. The source of Li at 227.0 m CSF and the shape of the Li profile remains enigmatic and will be the focus of future postcruise research.

Dissolved silica increases steadily from 625  $\mu\text{M}$  at 2.7 m CSF to 966  $\mu\text{M}$  at the top of Subunit IIB at 140.0 m CSF (Fig. F40B). From 140.0 to 361.2 m CSF (~50 m below the main fault zone), silica varies, ranging from 827 to 1161  $\mu\text{M}$ . Three peaks in H<sub>4</sub>SiO<sub>4</sub> coincide with K and Mg minima at 248.0, 306.7, and 344.0 m CSF. Below 361 m CSF, H<sub>4</sub>SiO<sub>4</sub> remains rather constant at ~630  $\mu\text{M}$ . Siliceous nannofossils (diatoms, radiolarians, and sponge spicules) were quite rare at Site C0004 with the exception of Unit I (see “[Lithology](#)” and “[Biostratigraphy](#)”). In Subunits IIA and IIB and Units III and IV, diatoms and radiolarians were either absent or very rare (see “[Lithology](#)” and “[Biostratigraphy](#)”). Thus, the initial increase in H<sub>4</sub>SiO<sub>4</sub> is likely due to dissolution of siliceous biogenic material, whereas silica variations below Unit I reflect variations in lithology and ash alteration.

Sr is below modern seawater value in the upper ~15 m of Unit I and then increases steadily to ~118  $\mu\text{M}$  at the base of Subunit IIA at 126.2 m CSF. Below this depth, Sr varies in Subunit IIB and then stabilizes and remains nearly constant from the top of Unit III to TD at 393.6 m CSF. The slight Sr decrease in the upper 15 m reflects minor Sr precipitation in authigenic carbonates in the SO<sub>4</sub> reduction zone. Below this interval, dissolved Sr mimics sedimentary CaCO<sub>3</sub> concentration (see “[Organic geochemistry](#)” and “[Lithology](#)”), indicating that Sr is primarily controlled by carbonate diagenesis.

Ba concentration was determined shipboard by inductively coupled plasma–atomic emission spectroscopy (ICP-AES) and on shore by inductively coupled plasma–mass spectrometry (ICP-MS). Ba from both methods is presented in Table T13, but only the shipboard Ba is shown in Figure F38. The main Ba-containing sediment phase in most marine sediments is barite (BaSO<sub>4</sub>). Elevated Ba is typically found in sediments underlying high-productivity surface waters (Ganeshram et al., 2003; Dymond et al., 1992; Eagle et al., 2003); thus, Ba concentration is typically greater in carbonate-bearing sections. Under oxic conditions, the mineral barite is extremely stable. However, when SO<sub>4</sub> becomes depleted, barite becomes undersaturated and dissolves, releasing a significant amount of Ba<sup>2+</sup> to the surrounding pore fluids. Dissolved Ba is slightly elevated with respect to bottom water from 2.7 to 13.4 m CSF. Ba markedly increases at 20 m CSF and continues to increase to the base of Subunit IIB to 285  $\mu\text{M}$  (~2000 times seawater value). After a sharp drop in dissolved Ba at 101.5 m CSF, it remains relatively constant in Subunit IIB, Unit III, and the top of Unit IV. Ba increases in the fault zone to 52  $\mu\text{M}$  at 290 m CSF, which is consistent with increased sediment CaCO<sub>3</sub>. Between 352 and 400 m CSF, Ba remains relatively constant at ~50  $\mu\text{M}$ . Like Sr, Ba generally mimics CaCO<sub>3</sub> concentration (see “[Organic geochemistry](#)” and “[Lithology](#)”). Slightly elevated Ba in the upper 13 m of Unit I likely reflects release of Ba from Fe and Mn oxides and oxyhydroxides during the early stages of organic matter diagenesis. The sharp increase in Ba below the SMT is the result of barite dissolution, and the variability in the dissolved Ba profile is likely controlled by the abundance of barite within the sediment.

## Trace elements (Rb, Cs, V, Cu, Zn, Mo, Pb, and U)

Rb decreases relatively rapidly from 1.71  $\mu\text{M}$  at 2.7 m CSF to 1.00  $\mu\text{M}$  at 29.5 m CSF and then remains remarkably constant to TD at 393.6 m CSF (Fig. F40F). The decline in Rb concentration in Unit I likely reflects uptake of Rb by zeolite formation during volcanic ash alteration. The Cs profile differs from those of Rb and K and generally varies with changes in lithology. Cs increases monotonically in Unit I from 2.7  $\mu\text{M}$  at 2.1 m CSF to 3.6  $\mu\text{M}$  at 126.0 m CSF. An abrupt transition from Units I to II is manifested by a decrease in Cs, which remains relatively constant at ~4  $\mu\text{M}$  to 306.8 m CSF. Cs increases again across the base of the fault zone into Unit IV.

Iron, copper, zinc, molybdenum, and lead display similar trends with depth, characterized by lower concentrations and variability in Unit I. Cu, Zn, V, and Pb display a peak at the base of Subunit IIA and

they are relatively constant in Subunit IIB (Figs. F41, F42). All of the trace metals display higher concentrations and variability in the fault zone (Unit III) and in Unit IV. Fe increases in some intervals in Unit I and Subunit IIA as a result of ongoing microbially mediated organic matter decomposition, which uses sedimentary Fe oxides and oxyhydroxides as electron acceptors. Likewise, Zn and Mo are likely mobilized within these units because of microbially mediated reduction of both Mn and Fe oxyhydroxides.

Uranium decreases abruptly from near seawater value at 2.7 m CSF to 2.2  $\mu\text{M}$  at 9.1 m CSF (Fig. F42C). Uranium is much more fluid mobile under oxic conditions than reducing conditions; thus, the rapid decline in U is the manifestation of the rapid depletion of dissolved oxygen and other complexes in the upper part of the sediment section. U remains relatively stable to 350 m CSF and then increases to 4.3  $\mu\text{M}$  at TD. Vanadium decreases sharply from 110  $\mu\text{M}$  at 2.7 m CSF to 11.9  $\mu\text{M}$  at 9.1 m CSF. Vanadium remains relatively constant to the base of Subunit IIA with a local maximum of 94  $\mu\text{M}$ . Vanadium remains near-seawater value but is variable from Subunit IIB to TD. Yttrium varies downhole with concentration ranging from 0.45 to 3.6 pM.

### $\delta^{18}\text{O}$

Pore fluid  $\delta^{18}\text{O}$  decreases almost linearly from seawater value at 2.7 m CSF to  $-2.82\text{‰}$  at the base of Subunit IIA (Fig. F43). Below  $\sim 120$  m CSF,  $\delta^{18}\text{O}$  decreases more slowly with positive anomalies at 248, 307, and 344 m CSF. The slight increases in  $\delta^{18}\text{O}$  in these intervals likely reflect mixing with drill water in brecciated zones, as  $\delta^{18}\text{O}$  data have not been corrected for drill water contamination. Below 352 m CSF,  $\delta^{18}\text{O}$  decreases slightly to  $-3.98\text{‰}$  at TD.

## Summary and discussion

The two primary controls on the pore fluid geochemical profiles collected at Site C0004 are volcanic ash alteration and microbially mediated reactions.

### Volcanic ash alteration

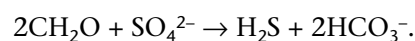
The dominant process controlling the pore fluid chemical profiles at Site C0004 is the alteration of volcanic ash to authigenic clay minerals and zeolites. This alteration is manifested by downhole increases in Cl and Na and decreases in Mg, B, K, and Rb. Chloride progressively increases with depth, reaching a value  $\sim 17\%$  greater than modern seawater value at 397.6 m CSF. This progressive Cl enrichment is most likely the result of water consumption during replacement of volcanic ash by authigenic clays and zeolites. The Mg, B, K, and Rb profiles corroborate

this inference because these chemical species are consumed from pore fluids during the formation of these authigenic minerals: Mg and B by clay minerals and Rb and K by zeolites. This strong signature of ash alteration was not observed at Site C0006 downslope from this site or along the Muroto transect drilled during ODP Leg 190.

Superimposed on the general concentration profiles associated with ash alteration are three anomalies associated with the fault zones at 248.0, 306.7, and 344.0 m CSF manifested by increases in  $\text{H}_4\text{SiO}_4$ , Na, and trace metals and decreases in Mg, K, and Rb. Additional shore-based analyses will be important for determining the cause of these variations.

### Microbially mediated reactions

Pore fluid profiles in the upper 30 m of the sediment column are dominated by microbially mediated reactions, and the SMT is reached between 16 and 20 m CSF. Above this interface, sulfate-reducing microbial communities utilize interstitial sulfate to oxidize sedimentary organic matter, reducing sulfate to sulfide and producing bicarbonate through the following reaction:



Below the interface, methanogens generate methane. At the interface in some environments (especially diffusive settings), microorganisms symbiotically reduce sulfate and oxidize methane by AOM. This net biogeochemical process is described by the following reaction (Reeburgh, 1976):



When methane oxidation by AOM is complete, usually in diffusional settings but not necessarily in advection-dominated environments, all of the methane fluxing upward is consumed before entering the water column. AOM also drives precipitation of authigenic carbonates, affecting carbon chemistry both above and below the SMT. The  $\delta^{13}\text{C}$  of dissolved inorganic carbon produced by AOM is depleted with respect to that produced by oxidation of organic matter by sulfate, and shore-based samples for carbon isotopic analyses were preserved to constrain the presence and relative amount of AOM occurring at this site.

In typical continental margin sediments with low upward advection rates, the downward sulfate flux is balanced by upward methane flux. In regions of upward advection of fluid and methane, AOM is not complete and a significant amount of methane can pass across the sediment/water interface and into the

water column. These conditions are most often present within continental margin sediments that harbor gas hydrate and in subduction zones. In the case of low upward methane advection, sulfate and methane are coupled geochemical species because AOM occurring at the SMT involves the microbially mediated co-consumption of sulfate and methane. If AOM is complete, the stoichiometric ratio between sulfate and methane consumed by AOM is 1:1 and the flux of sulfate to the SMT is equivalent to the upward methane flux to the SMT. However, it is often difficult to discern between sulfate reduction by organic matter degradation and sulfate reduction by AOM from sulfate concentration-depth profiles alone. By knowing both the sulfate and alkalinity concentration-depth profile to the depth of the SMT, it is possible to discern between these two processes because for each mole of  $\text{SO}_4$  reduced by AOM, 1 mole of alkalinity is produced. In contrast, during organic matter diagenesis, 2 moles of alkalinity are produced for each mole of sulfate reduced. In Figure F44, we plot the change in alkalinity versus the change in sulfate in the uppermost part of Unit I at Site C0004. The alkalinity data are corrected for the consumption of alkalinity by authigenic carbonate precipitation. The blue line is the trajectory expected for simple organic matter degradation, and the red line is that expected for AOM. As shown in the plot, sulfate reduction by organic matter degradation is the dominant process occurring in the upper 5 m of the sediment column, whereas AOM is the dominant process consuming sulfate from 5 m CSF to the SMT with only a minor contribution from ordinary organic matter degradation.

Below the SMT, there is evidence for ongoing microbially mediated decomposition of organic matter. This is manifested by the progressive increase in pore fluid  $\text{NH}_4$  and Mn, as well as elevated  $\text{PO}_4$  and Br. The similarity in the manganese and ammonium profiles indicates Mn oxyhydroxides are being utilized as terminal electron acceptors for organic matter degradation at greater depths in the sediment column. Three maxima in  $\text{NH}_4$  at 248.0, 306.7, and 344.0 m CSF correspond to marked changes in pore fluid major, minor, and trace elements.

## Organic geochemistry

### Hydrocarbon gas composition

Methane was detected in all samples at Site C0004 (Table T17; Fig. F45). The estimated SMT zone is at 16–20 m CSF. Below this depth, methane concentration increases sharply and reaches a maximum of 9.7 mM at 35.3 m CSF. In deeper sediments, concentration is highly variable. The changes could poten-

tially reflect changes in lithology and corresponding effects on methane degassing upon core retrieval (including core quality) rather than in situ changes in interstitial water methane concentration (Paull, Matsumoto, Wallace, and Dillon, 2000). Changes in lithology and/or physical properties, such as the occurrence of unconsolidated sand and gravels with greater pore space, can have a strong influence on the degassing of methane. Additionally, the quality of the recovered core or contamination (e.g., by seawater; see “**Inorganic geochemistry**”) can lead to a higher loss of methane. If there are “real” changes in in situ methane concentration, they should also be visible in related pore water constituents (i.e., sulfate, alkalinity, and chloride), which is not seen (see “**Inorganic geochemistry**”). However, increased methane concentration below ~260 m CSF (in Unit III) coincides with a fractured zone (fault-bounded unit, see “**Structural geology**”) coincident with variations in major, minor, and trace element concentrations (see “**Inorganic geochemistry**”). Thus, it cannot be completely excluded that the higher methane concentration in this zone may be related to flow of methane-enriched fluids. This requires further shore-based analyses.

Low ethane concentration was detected in a majority of the samples with mean concentration of ~2  $\mu\text{M}$  below the SMT (Table T17; Fig. F45). The methane/ethane ( $C_1/C_2$ ) ratio is constantly high throughout the cores, indicating biogenic origin of the hydrocarbon gases. Only at the SMT is a decrease in the  $C_1/C_2$  ratio found. The additional applied headspace extraction procedure with NaOH solution resulted in higher gas yields compared to the 30 min extraction for safety monitoring purposes (cf. Tables T18, T17). This is consistent with observations from ODP Leg 201 (D’Hondt, Jørgensen, Miller, et al., 2003).

### Sediment carbon, nitrogen, and sulfur composition

Calcium carbonate ( $\text{CaCO}_3$ ) content calculated from inorganic carbon concentration ranges from 16.3 to 0.2 wt% (Table T19; Fig. F46). The amount of  $\text{CaCO}_3$  is rather high in Unit I and decreases to a mean value of ~3.5 wt% in the lower units. This is in good agreement with calcite data from XRD measurements (see “**Lithology**”).

Total organic carbon (TOC) content remains low throughout the cores (average = 0.43 wt%). Like TOC concentration, total nitrogen (TN) content is rather uniform in the sediments and averages ~0.07 wt%. The ratio of TOC and TN (C/N) has a mean value of ~6, which indicates that the organic matter in the sediments from Site C0004 is mainly of marine origin (with an expected value for marine organic mat-

ter of 6–9). Below 350 m CSF, C/N values increase to a maximum value of 10.0.

Total sulfur (TS) content was generally low, ranging from 0.04 to 0.57 wt% through Units I and II (average = 0.23 wt%). In Units III and IV, the concentration is even lower (average = 0.19 wt%) except for a slight enrichment at ~390 m CSF.

## Microbiology and biogeochemistry

### Sample processing

To study microbiological and biogeochemical characteristics in sediments at Site C0004, samples were obtained from 71 different depth locations (Table T20). Almost all sample processing was carried out after X-ray CT scanning and was completed within 1 h after core recovery on deck.

### Cell abundance

Using paraformaldehyde-fixed slurry samples, preliminary microbial cell abundances were enumerated by visual inspection using the SYBR Green I staining method (Lunau et al., 2005; see “**Microbiology and biogeochemistry**” in the “Expedition 316 methods” chapter). Under epifluorescent microscopy, very high numbers of microbial cells were observed in sediments at Site C0004 (Fig. F47). In the near-seafloor core samples, relatively large coccoids and rod-shaped cells were observed with population size estimated to be  $5.70 \times 10^9 \pm 1.01 \times 10^9$  cells/cm<sup>3</sup> ( $N = 6$ ). Some aggregate structures consisting of a few bright cells were observed in shallow sediment samples. Cell populations slightly decreased with depth to 150 m CSF and slightly increased at ~280 m CSF in the fault zone of the lithologic Unit III accretionary prism (Fig. F47). In the fault zone,  $3.64 \times 10^9 \pm 5.90 \times 10^8$  cells/cm<sup>3</sup> ( $N = 6$ ) were present as the endolithic microbial community, of which some components produced brighter fluorescent signals than those in upper sediments (Fig. F48). Irregular coccoids as well as tiny coccoids were also observed. Interestingly, cell populations sharply decreased across the lithologic Unit III/IV boundary. Minimum cell abundance,  $5.48 \times 10^8 \pm 2.09 \times 10^8$  cells/cm<sup>3</sup> ( $N = 6$ ), was observed at 320.8 m CSF. Fluorescent signals below the fault structure were recognizable as cells but were generally dark, likely indicating low metabolic activity. Average cell abundance in the sediments at Site C0004 was estimated to be  $1.83 \times 10^9 \pm 4.25 \times 10^8$  cells/cm<sup>3</sup> ( $N = 25$ ).

The average detected microbial population at this site is notably higher than at other drilling sites that

typically harbor  $10^6$ – $10^9$  microbial cells/cm<sup>3</sup> (Parkes et al., 2000). The population size generally decreases with increasing depth because of the limitation of available nutrients (carbon and energy sources) and habitable space during burial. One exception was observed during the *Chikyu* shakedown cruise CK06-06 offshore the Shimokita Peninsula in Japan, where the sediments harbor  $>10^{10}$  cells/cm<sup>3</sup> throughout the core to 365 m CSF, showing little or no decrease in cell number with depth (Inagaki et al., submitted). At the Shimokita site, the strong fluid and gas flow from underlying coal layers as well as high photosynthetic production in the water column are thought to support the large microbial population. Elevated cell numbers in deep seafloor environments were also observed in sediment cores at Site 1301 on the Juan de Fuca Ridge flank, where the upward flow of hydrothermal fluids from the basaltic aquifer supports microbial life (Cowen et al., 2002; Nakagawa et al., 2006; Engelen et al., 2008). Similarly, this environment may be affected by fluid and dissolved gas flow, in which dissolved nutrients (probably generated by physical degradation of subducted organic matter and/or reaction between sedimentary rocks and fluids) may support the abundant microbial life. The adaptation and ecological functioning of these cells in the seafloor seep ecosystem will be intensively investigated on shore by cultivation, molecular (deoxyribonucleic acid/ribonucleic acid/enzyme), and lipid biomarker analyses including carbon and nitrogen isotopic compositions.

## Physical properties

At Site C0004, physical property measurements were made to provide basic information characterizing lithologic units, states of consolidation, deformation, and strain and to correlate coring results with downhole logging data. After capturing X-ray CT images and letting the core reach thermal equilibrium with ambient temperature at ~20°C, gamma ray attenuation (GRA) density, magnetic susceptibility, natural gamma radiation, *P*-wave velocity, and non-contact electrical resistivity were measured using a MSCL system on whole-round core sections (MSCL-W). Thermal conductivity was measured using a full-space needle probe method to 138 m CSF and a half-space line source method on split working halves for lithified sediments deeper in the hole that were impenetrable with the needle probe. Cores were then split in two longitudinally, one half for archiving and one half for sampling and analysis. A photo image capture logger (MSCL-I) and a color spectrophotometer (MSCL-C) were used to collect images of the

split surfaces of the archive halves. Moisture and density (MAD) were measured on discrete subsamples collected from the working halves as well as from “clusters” adjacent to whole-round samples that were removed before splitting. Vane shear and penetration experiments were performed on working halves to 73 m CSF. Additional discrete subsamples from working halves were used to perform electrical conductivity measurements, *P*-wave velocity measurements, and *P*-wave anisotropy calculations.

## Density and porosity

Bulk density values at Site C0004 were determined from both GRA measurements on whole cores and MAD measurements on discrete samples from the working halves of split cores (see “**Physical properties**” in the “Expedition 316 methods” chapter). A total of 375 discrete samples were analyzed for MAD (198 from Hole C0004C and 177 from Hole C0004D). Wet bulk density values determined from MAD measurements increase roughly linearly with depth (Fig. F49A). In comparison, GRA bulk density measured with the MSCL logging suite also roughly increases linearly with depth, albeit at a diminished rate of increase. GRA bulk density is generally lower than MAD bulk density and reveals a larger degree of scatter. Grain density values were also determined from MAD measurements on discrete samples. Grain density was approximately constant with depth (average =  $\sim 2.67$  g/cm<sup>3</sup>) (Fig. F49B).

Porosity values for core samples were estimated from whole-round core MSCL scans and calculated from MAD measurements. MAD-derived porosity (see “**Physical properties**” in the “Expedition 316 methods” chapter) generally decreases with depth (Fig. F49C). In comparison, MSCL-derived porosity estimates are generally higher by as much as a factor of  $\sim 1.6$  and are much more scattered than MAD-derived porosity values. The larger degree of scatter in MSCL porosity reflects the fact that these measurements integrate the effects of cracks, voids, and other porosity variations over the whole core, whereas discrete measurements are typically made on intact chunks of material when possible. Because of the greater amount of scatter in MSCL density and porosity data, we focus on bulk density and porosity derived from MAD measurements.

Within lithologic Unit I (see “**Lithology**”), bulk density increases gradually with depth ( $\sim 1.60$  to  $1.68$  g/cm<sup>3</sup>) from 0 to  $\sim 78$  m CSF (Fig. F49A) and porosity decreases slightly from  $\sim 65\%$  to  $59\%$  (Fig. F49A, F49C).

Within lithologic Unit II, bulk density is scattered over a relatively wide range from  $1.63$  to  $2.02$  g/cm<sup>3</sup>

slightly increasing overall with depth (Fig. F49A). Density variations likely reflect lithologic variations, which varied from predominantly mud and silt to occasional sand, each with varying degrees of lithification. This overall trend in bulk density is mirrored by a slight decrease in porosity with depth, from  $\sim 53\%$  at the top of Unit II to  $\sim 49\%$  near the bottom of Unit II (Fig. F49C). The paucity of data from Unit II is due to low core recovery in this interval ( $< 50\%$ ).

Within lithologic Unit III, bulk density and porosity are scattered over the ranges  $1.70$ – $2.04$  g/cm<sup>3</sup> and  $46\%$ – $59\%$ , respectively (Fig. F49A, F49C). No clear trends in either density or porosity with depth were observed in Unit III.

Within lithologic Unit IV, bulk density and porosity are scattered between  $1.69$  and  $2.09$  g/cm<sup>3</sup> and  $37\%$ – $62\%$ , respectively (Fig. F49C); this scatter may be due to variations in lithologies of the measured samples. Within Unit IV, porosity increases (from  $\sim 42\%$  to  $\sim 50\%$ ) with depth in two zones ( $320$ – $355$  and  $355$ – $400$  m CSF). However, data are too scattered to allow us to make any definitive conclusions from these trends.

## Density and porosity changes across lithologic unit boundaries

At the Unit I/II boundary ( $\sim 78$  m CSF), bulk density increases from  $1.68$  to  $1.79$  g/cm<sup>3</sup> (Fig. F49A) and porosity abruptly decreases from  $\sim 59\%$  to  $53\%$ . These changes coincide with the abrupt transition from younger less compacted Quaternary slope sediments to older more compacted Pliocene prism sediments.

At the Unit II/III boundary, little change is seen in the values of bulk density and porosity. At the Unit III/IV boundary, bulk density abruptly increases and porosity decreases from  $\sim 1.84$  to  $1.98$  g/cm<sup>3</sup> and from  $\sim 50\%$  to  $43\%$ , respectively. At this boundary, older Pliocene sediments of Unit III (which are younger than the lower part of Unit II) are thrust over the younger Quaternary sediments (see “**Lithology**” and “**Structural geology**”) of Unit IV. Unit III is an interval of faulted and brecciated rocks (identified as a fault zone between  $\sim 256$  and  $315$  m CSF, see “**Structural geology**,” and denoted with an orange band in Fig. F49). The higher than expected porosity values and associated lower bulk density values in Unit III may reflect its younger age compared to the lower half of Unit II, as well as increased crack/damage porosity within the fault zone. The lower values of porosity at the top of Quaternary Unit IV compared to Quaternary Unit I are probably due to the deeper structural horizon of Unit IV and the initially greater burial depth of these sediments prior to underthrusting.

## Electrical conductivity, *P*-wave velocity, and anisotropy

Measurements of *P*-wave velocity and electrical conductivity and the relative anisotropy of these properties were made on RCB samples that were indurated enough to construct sample polyhedrons. In many cores, no samples were taken because of poor recovery, drilling-induced deformation, or low cohesion. *P*-wave velocity ranges from 1200 to 2000 m/s with noticeable excursions around an average value of ~1500 m/s, particularly between 260 and 400 m CSF (Fig. F50A). In order to confirm these variations, even though they exceed the estimated uncertainty caused by partial drying, an additional series of *P*-wave velocity measurements was performed on nominally dry samples (i.e., several days after initial processing [blue circles, Fig. F50A]). Results show an overall decrease in *P*-wave velocity associated with sample drying. More importantly, however, the *P*-wave velocity variations in the dry samples are nearly identical to the original pattern. Candidate processes that might cause these variations include changes in lithology, uneven stress relief, weak cementation, or deformation. Deformation may induce either increases or decreases in *P*-wave velocity, depending on whether the deformation involves compaction or microcracking. Two notably fractured and brecciated intervals were recognized at ~275 and ~312 m CSF (see “**Structural geology**”), and these intervals correspond to slightly higher *P*-wave velocity. Below the thrust zone at ~312 m CSF, two relatively low velocity zones (~1.3 km/s) can be isolated at 340 and 380 m CSF. These zones are located at depths where small-scale (0.1 m) fracturing and faulting had been identified. Moreover, slight lithologic changes such as centimeter-scale sand and ash layers may potentially be responsible for contrasting mechanical properties that lead to variations in *P*-wave velocity.

*P*-wave velocity anisotropy data (Fig. F50B), although scarce and nearly constant in the uppermost 300 m CSF, exhibit a considerable increase in anisotropy within the underthrust sediments between the two zones of relatively low *P*-wave velocity. This anisotropy is mostly planar and is consistent with typical sedimentary compaction (vertical minimum velocity and high maximum and intermediate velocities within the bedding plane). This type of fabric might be present over most of the depth range of the underthrust sediments except in zones where interrupted by mechanical deformation such as fracturing/faulting. However, the anisotropy data are also consistent with bed-parallel shear of the underthrust sediments.

Electrical conductivity data (Fig. F50C) were obtained over a narrower depth range than *P*-wave velocity measurements. Like *P*-wave data, no general trend is observed in the electrical conductivity data. However, these data do exhibit an interesting correlation with *P*-wave velocity data. In the underthrust sediments between 345 and 375 m CSF, at depths where *P*-wave velocity and *P*-wave anisotropy are relatively high, electrical conductivity reaches a local minimum. This observation suggests the presence of a smaller and/or more tortuous pore space relative to the strata above and below these depths. The anisotropy of electrical conductivity (Fig. F50D) is also consistent with these observations. At these depths, electrical conductivity anisotropy is higher, with significantly lower bedding-normal conductivity than bedding-parallel conductivity.

These results provide significant information on the microstructure of indurated samples across the shallow megasplay. Preliminary hypotheses are that this material has been either strongly deformed, in which case the samples may have been crushed and re-consolidated, or very slightly deformed to undeformed, in which case the samples have retained cohesion. These end-members could be revealed by higher and lower *P*-wave velocities, respectively. A potential bias exists in that samples meeting measurement criteria were relatively rare in split cores and may not be representative of the average because they tended to be more indurated than the rest of the cored material. An overwhelming amount of the material cored was not indurated enough to make these measurements. Postcruise work will test the formulated hypotheses. These tests include sample reorientation through paleomagnetic measurements, measurement of the anisotropy of magnetic susceptibility, and thin sectioning of some of the cubes to identify facies, textural fabrics, and deformation features.

## Thermal conductivity

Thermal conductivity measurements were conducted on whole-round HPCS cores (<230 m CSF) and on split core samples from RCB cores from depths >230 m CSF. Thermal conductivity of the HPCS cores (<230 m CSF) ranges from 0.81 to 1.45 W/(m·K) (Table T21; Fig. F51A). Between 200 and 230 m CSF, the sediments became more lithified, resulting in a relatively large variation in thermal conductivity because of poor contact between the needle probe and the core. Line source measurements were restricted to samples that did not show significant mechanical disturbance and that were 10 cm or larger. Unfortunately, between ~150 and 375 m CSF, split core sections did not have pieces large enough for half-space measurements. Below 375 m CSF, line

source measurements were made. Thermal conductivity from cores deeper than 150 m CSF will be measured postcruise using a divided bar apparatus.

Average thermal conductivities are 1.02, 1.09, and 1.50 W/(m·K), for Units I, II, and IV, respectively. In general, thermal conductivity increases with depth and correlates with porosity. As porosity decreases, thermal conductivity increases as water is forced from void spaces because the thermal conductivity of grains is greater than that of water.

### In situ temperature

In situ temperature was measured using the APCT3. Starting at 25.4 m CSF, measurements were taken at Cores 316-C0004-3H, 6H, 9H, and 18H. In total, four successful temperature measurements were made to 135.0 m CSF (Table T22; Fig. F51B). The APCT3 was not used when approaching HPCS refusal depth and is not compatible with RCB coring. Davis-Villinger Temperature Probe (DVTP) measurements were not attempted at this site.

All measurements were made in a moderate sea state (2 m swell) and all temperature-time series were recorded at a sample interval of 1 s. The temperature tool was stopped at the mudline for as long as 10 min prior to each penetration with the exception of the third measurement (Core 316-C0004-9H). The average apparent bottom water temperature is 1.87°C (Table T22). Temperature-time series for each temperature measurement are shown in Figure F52. Significant frictional heating occurred on all penetrations of the APCT3 with the temperature-time records exhibiting characteristic probe penetration and subsequent decay. For most of the measurements, the probe was kept in the bottom for >7 min, allowing accurate extrapolation to equilibrium formation temperature based on a 1/time approximation (Table T22). The effective origin time of the thermal pulse was estimated by varying the assumed origin time until the thermal decay pulse best fit a theoretical curve. A delay of 13–25 s from the initial penetration heating time was found to give the best fitting linear 1/time curve. All of the measurements appear to be reliable, exhibiting good penetration heating and initial decay curves. Equilibrium fits to temperature-time series are good, and temperatures increase linearly with depth. Coupled with the average bottom water temperature, temperature measurements yield a least-squares gradient of 52°C/km (Fig. F51B).

### Heat flow

If heat transfer is by conduction and heat flow is constant, the thermal gradient will be inversely pro-

portional to thermal conductivity according to Fourier's Law. This relationship can be linearized by plotting temperature as a function of summed thermal resistance (Bullard, 1939) (Fig. F51C). The least-squares fit to temperature and thermal resistance data indicates a heat flow of 55 mW/m<sup>2</sup> and a bottom water temperature of 1.90°C. The estimated bottom water temperature is only 0.03°C different than the average of the measured apparent bottom water temperature (Table T22). Predicted temperature deviates from those measured by <0.3°C. A constant conductive heat flow appears to describe the overall thermal structure quite well. APCT3 temperature measurements were restricted to depths above 135 m CSF, and the preceding discussion applies only to this interval. Below this interval, temperatures can be projected on the basis of the thermal conductivity measurements, assuming constant heat flow and conductive heat transfer. Because of the lithologic similarity between Units II and III, thermal conductivity measured in Unit II is used to estimate thermal conductivity in Unit III. The extrapolated conductive temperature at 258 m CSF (estimated depth of the megasplay) is 18°C.

### Shear strength

Shear strength measurements were determined using a semiautomated miniature vane shear device and a pocket penetrometer. Measurements were made at discrete locations on the working halves of split cores at a frequency of approximately three measurements per core in sections 2, 5, and 7 to a maximum depth of 73 m CSF. Below these depths, excessive cracking and separation of the core material occurred and the measurement technique was discontinued. Tests were conducted on relatively intact and homogenous regions of these sections, generally somewhere between 50 and 100 cm below the top of the section. To minimize uncertainties induced by the measurement technique, vane shear tests were conducted first, followed by penetrometer tests. Penetrometer tests were located 1–2 cm from the site of the vane shear penetration. No vane shear measurements were conducted on whole cores. Both instruments were inserted orthogonally to the surface of the working halves. The rotation rate of the semiautomated vane shear apparatus on board the *Chikyu* is 71°/min.

Shear strength at Site C0004 increases with depth (Fig. F53) and inversely correlates with porosity. Penetrometer measurements of compressive strength are consistently lower than those measured directly using the vane shear apparatus with an average difference of 17% across all measurements.

## Color spectrometry

Color reflectance results are presented in Figure F54. The L\* values range from ~30 to 50. Some high values of ~70 may correspond to ash layers. The a\* values range from -2 to 1 and the b\* values range from 2 to 6. At depths less than ~100 m CSF, each index slightly decreases. There is no significant anomaly of these values with depth.

## Magnetic susceptibility

Volumetric magnetic susceptibility was measured using the whole-round core MSCL in all recovered cores from Site C0004 (Fig. F55). Magnetic susceptibility values in Unit I are low and relatively uniform. Magnetic susceptibility values are higher in the upper 50 m of Unit II and then decrease. High values of magnetic susceptibility seem to be correlated with the megathrust and great scatter occurs in this region.

## Natural gamma ray

MSCL natural gamma ray (NGR) is reported in counts per second (cps). The background scatter, produced by Compton scattering, photoelectric absorption, and pair production was measured at the beginning and subtracted from measured gamma ray values. In general, NGR counts are low and are consequently likely to be affected by the short counting interval and porosity variations. Values <15 cps are likely due to voids. The average and standard deviation of NGR results are 30 and 8 cps, respectively (Fig. F56). NGR values decrease slightly with depth and appear to oscillate subtly as a function of depth; however, there are no large anomalies.

## Integration with logging-while-drilling data

Holes C0004B, C0004C, C0004D are ~20 m apart (Fig. F1). Core-seismic integration between Holes C0004B, C0004C, and C0004D is mainly based on prestack depth-migrated corrected seismic profiles Inline 2675 (Fig. F2A) and Cross-line 5295 (Fig. F2B). In these seismic profiles, some key reflectors and thick layers are clear. For example, an unconformity is identified at 78 m CSF in cores from Hole C0004C and the bottom of the splay fault is at ~322 m CSF in Hole C0004D. Moreover, the dips at various depths indicate that even though the distance between holes is relatively small, depth shifts are >10 m because steeply dipping strata and faults may be needed to correlate data.

Despite the low vertical resolution of the seismic data, core-log integration between Holes C0004C, C0004D, and C0004B is referenced to seismic profiles relying primarily on the comparison between

MSCL NGR and P-wave velocity and gamma ray and sonic velocity logs from LWD data sets (Fig. F57). Cores from Hole C0004C provide a more continuous record of MSCL-W logs than those from Hole C0004D. Generally, the estimated uncertainty on a depth correlation is <10 cm. However, from 130 to 280 m CSF in Hole C0004D, correlations are more uncertain because of low core recovery. Further, the LWD gamma ray log does not provide a unique solution. For this interval, correlations rely to a greater extent on bedding and structural dips interpreted from seismic reflection data. In addition, the borehole image from the RAB tool was also used to correlate data between holes. Breakout zones, shear zones, some steep faults, and rare sand/sandstone layers distinguished from RAB images matched well with cores.

Depth-shifted profiles are shown in Figure F57, and depth shifts applied to Hole C0004B are given in Table T23. Depth shifts are based on 47 correlations between the three holes. Depth transfer functions were defined by linear regression of the correlated positions. LWD data from Hole C0004B have been used to create synthetic LWD logs for the locations of Holes C0004C and C0004D.

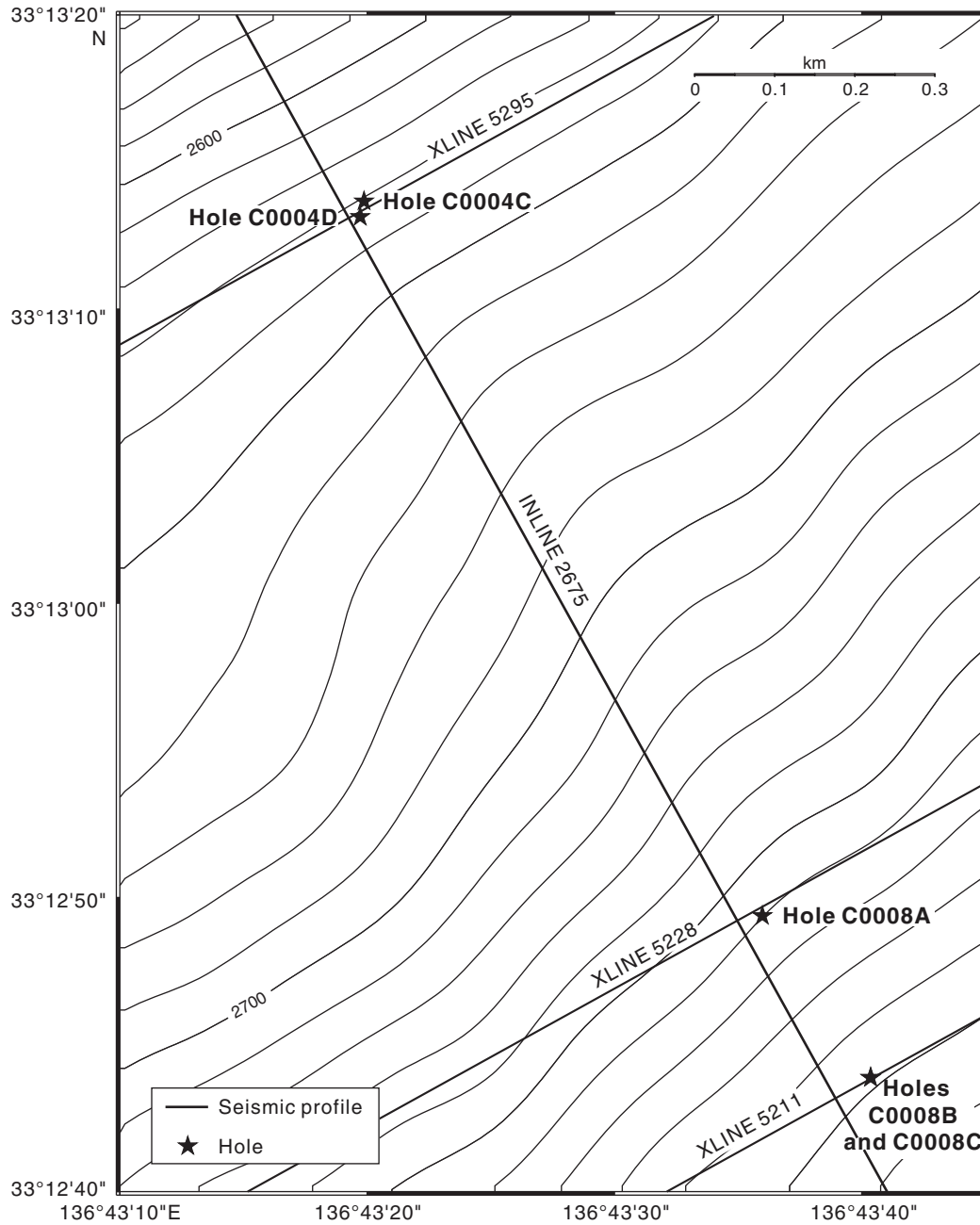
## References

- Bullard, E.C., 1939. Heat flow in South Africa. *Proc. R. Soc. London, Ser. A*, 173:474–502.
- Cowen, J.P., Giovannoni, S.J., Kenig, F., Johnson, H.P., Butterfield, D., Rappé, M.S., Hutnak, M., and Lam, P., 2002. Fluids from aging ocean crust that support microbial life. *Science*, 299(5603):120–123. doi:10.1126/science.1075653
- D'Hondt, S.L., Jørgensen, B.B., Miller, D.J., et al., 2003. *Proc. ODP, Init. Repts.*, 201: College Station, TX (Ocean Drilling Program). doi:10.2973/odp.proc.ir.201.2003
- Dymond, J., and Collier, R., 1996. Particulate barium fluxes and their relationships to biological productivity. *Deep-Sea Res., Part II*, 43(4–6):1283–1308. doi:10.1016/0967-0645(96)00011-2
- Dymond, J., Suess, E., and Lyle, M., 1992. Barium in deep-sea sediment: a geochemical proxy for paleoproductivity. *Paleoceanography*, 7(2):163–181. doi:10.1029/92PA00181
- Eagle, M., Paytan, A., Arrigo, K.R., van Dijken, G., and Murray, R.W., 2003. A comparison between excess barium and barite as indicators of carbon export. *Paleoceanography*, 18(1):1021. doi:10.1029/2002PA000793
- Engelen, B., Ziegelmüller, K., Wolf, L., Köpke, B., Gittel, A., Cypionka, H., Treude, T., Nakagawa, S., Inagaki, F., Lever, M.A., and Steinsbu, B.O., 2008. Fluids from the oceanic crust support microbial activities within the deep biosphere. *Geomicrobiol. J.*, 25(1):56–66. doi:10.1080/01490450701829006

- Ganeshram, R.S., François, R., Commeau, J., and Brown-Leger, S.L., 2003. An experimental investigation of barite formation in seawater. *Geochim. Cosmochim. Acta*, 67(14):2599–2605. doi:10.1016/S0016-7037(03)00164-9
- Gee, J., Staudigel, H., and Tauxe, L., 1989. Contribution of induced magnetization to magnetization of seamounts. *Nature (London, U. K.)*, 342(6246):170–173. doi:10.1038/342170a0
- Gradstein, F.M., Ogg, J.G., and Smith, A. (Eds.), 2004. *A Geologic Time Scale 2004*: Cambridge (Cambridge Univ. Press). <http://www.stratigraphy.org/>
- Hampton, M.A., Lee, H.J., and Locat, J., 1996. Submarine landslides. *Rev. Geophys.*, 34(1):33–59. doi:10.1029/95RG03287
- Inagaki, F., Morono, Y., Masui, N., Terada, T., Imachi, H., Tomaru, H., Ogihara, S., Takeuchi, L., Kotani, R., Ogawa, N., Ohkouchi, N., Yoshioka, H., Uematsu, K., Kobayashi, T., Takai, K., Matsumoto, R., Curewitz, D., Aoi, K., and Horikoshi, K., submitted. Abundant deep sub-seafloor life near methane hydrate fields off Japan.
- Kimura, G., Sreaton, E.J., and Curewitz, D., 2007. NanTroSEIZE Stage 1: NanTroSEIZE shallow megasplay and frontal thrusts. *IODP Sci. Prosp.*, 316. doi:10.2204/iodp.sp.316.2007
- Lunau, M., Lemke, A., Walther, K., Martens-Habben, W., and Simon, M., 2005. An improved method for counting bacteria from sediments and turbid environments by epifluorescence microscopy. *Environ. Microbiol.*, 7(7):961–968. doi:10.1111/j.1462-2920.2005.00767.x
- Moore, G.F., Bangs, N.L., Taira, A., Kuramoto, S., Pangborn, E., and Tobin, H.J., 2007. Three-dimensional splay fault geometry and implications for tsunami generation. *Science*, 318(5853):1128–1131. doi:10.1126/science.1147195
- Moore, G.F., Taira, A., Klaus, A., Becker, L., Boeckel, B., Cragg, B.A., Dean, A., Fergusson, C.L., Henry, P., Hirano, S., Hisamitsu, T., Hunze, S., Kastner, M., Maltman, A.J., Morgan, J.K., Murakami, Y., Saffer, D.M., Sánchez-Gómez, M., Sreaton, E.J., Smith, D.C., Spivack, A.J., Steurer, J., Tobin, H.J., Ujiie, K., Underwood, M.B., and Wilson, M., 2001. New insights into deformation and fluid flow processes in the Nankai Trough accretionary prism: results of Ocean Drilling Program Leg 190. *Geochim., Geophys., Geosyst.*, 2(10):1058. doi:10.1029/2001GC000166
- Moore, G.F., Taira, A., Klaus, A., et al., 2001. *Proc. ODP, Init. Repts.*, 190: College Station, TX (Ocean Drilling Program). doi:10.2973/odp.proc.ir.190.2001
- Nakagawa, S., Inagaki, F., Suzuki, Y., Steinsbu, B.O., Lever, M.A., Takai, K., Engelen, B., Sako, Y., Wheat, C.G., Horikoshi, K., and Integrated Ocean Drilling Program Expedition 301 Scientists, 2006. Microbial community in black rust exposed to hot ridge-flank crustal fluids. *Appl. Environ. Microbiol.*, 72(10):6789–6799. doi:10.1128/AEM.01238-06
- Parkes, R.J., Cragg, B.A., and Wellsbury, P., 2000. Recent studies on bacterial populations and processes in sub-seafloor sediments: a review. *Hydrogeol. J.*, 8(1):11–28. doi:10.1007/PL00010971
- Paull, C.K., Matsumoto, R., Wallace, P.J., and Dillon, W.P. (Eds.), 2000. *Proc. ODP, Sci. Results*, 164: College Station, TX (Ocean Drilling Program). doi:10.2973/odp.proc.sr.164.2000
- Reeburgh, W.S., 1976. Methane consumption in Cariaco Trench waters and sediments. *Earth Planet. Sci. Lett.*, 28(3):337–344. doi:10.1016/0012-821X(76)90195-3
- Shipboard Scientific Party, 2001a. Site 1175. In Moore, G.F., Taira, A., Klaus, A., et al., *Proc. ODP, Init. Repts.*, 190: College Station, TX (Ocean Drilling Program), 1–92. doi:10.2973/odp.proc.ir.190.106.2001
- Shipboard Scientific Party, 2001b. Site 1176. In Moore, G.F., Taira, A., Klaus, A., et al., *Proc. ODP, Init. Repts.*, 190: College Station, TX (Ocean Drilling Program), 1–80. doi:10.2973/odp.proc.ir.190.107.2001
- Shipboard Scientific Party, 2001c. Site 1178. In Moore, G.F., Taira, A., Klaus, A., et al., *Proc. ODP, Init. Repts.*, 190: College Station, TX (Ocean Drilling Program), 1–108. doi:10.2973/odp.proc.ir.190.109.2001
- Taira, A., Hill, I., Firth, J.V., et al., 1991. *Proc. ODP, Init. Repts.*, 131: College Station, TX (Ocean Drilling Program). doi:10.2973/odp.proc.ir.131.1991
- Ujiie, K., Hisamitsu, T., Maltman, A.J., Morgan, J.K., Sánchez-Gómez, M., and Tobin, H.J., 2003. Deformation structures and magnetic fabrics at Site 1178: implication for deformation history recorded in accreted sediments at an evolved portion of the Nankai accretionary prism. In Mikada, H., Moore, G.F., Taira, A., Becker, K., Moore, J.C., and Klaus, A. (Eds.), *Proc. ODP, Sci. Results*, 190/196: College Station, TX (Ocean Drilling Program), 1–15. doi:10.2973/odp.proc.sr.190196.202.2003
- Underwood, M.B., Moore, G.F., Taira, A., Klaus, A., Wilson, M.E.J., Fergusson, C.L., Hirano, S., Steurer, J., and the Leg 190 Shipboard Scientific Party, 2003. Sedimentary and tectonic evolution of a trench-slope basin in the Nankai subduction zone of southwest Japan. *J. Sediment. Res.*, 73(4):589–602. doi:10.1306/092002730589
- Zhao, X., Roperch, P., and Stokking, L.B., 1994. Magnetostratigraphy of the north Aoba Basin. In Greene, H.G., Collot, J.-Y., Stokking, L.B., et al., *Proc. ODP, Sci. Results*, 134: College Station, TX (Ocean Drilling Program), 457–474. doi:10.2973/odp.proc.sr.134.025.1994
- Zijderveld, J.D.A., 1967. AC demagnetization of rocks: analysis of results. In Collinson, D.W., Creer, K.M., and Runcorn, S.K. (Eds.), *Methods in Palaeomagnetism*: New York (Elsevier), 254–286.

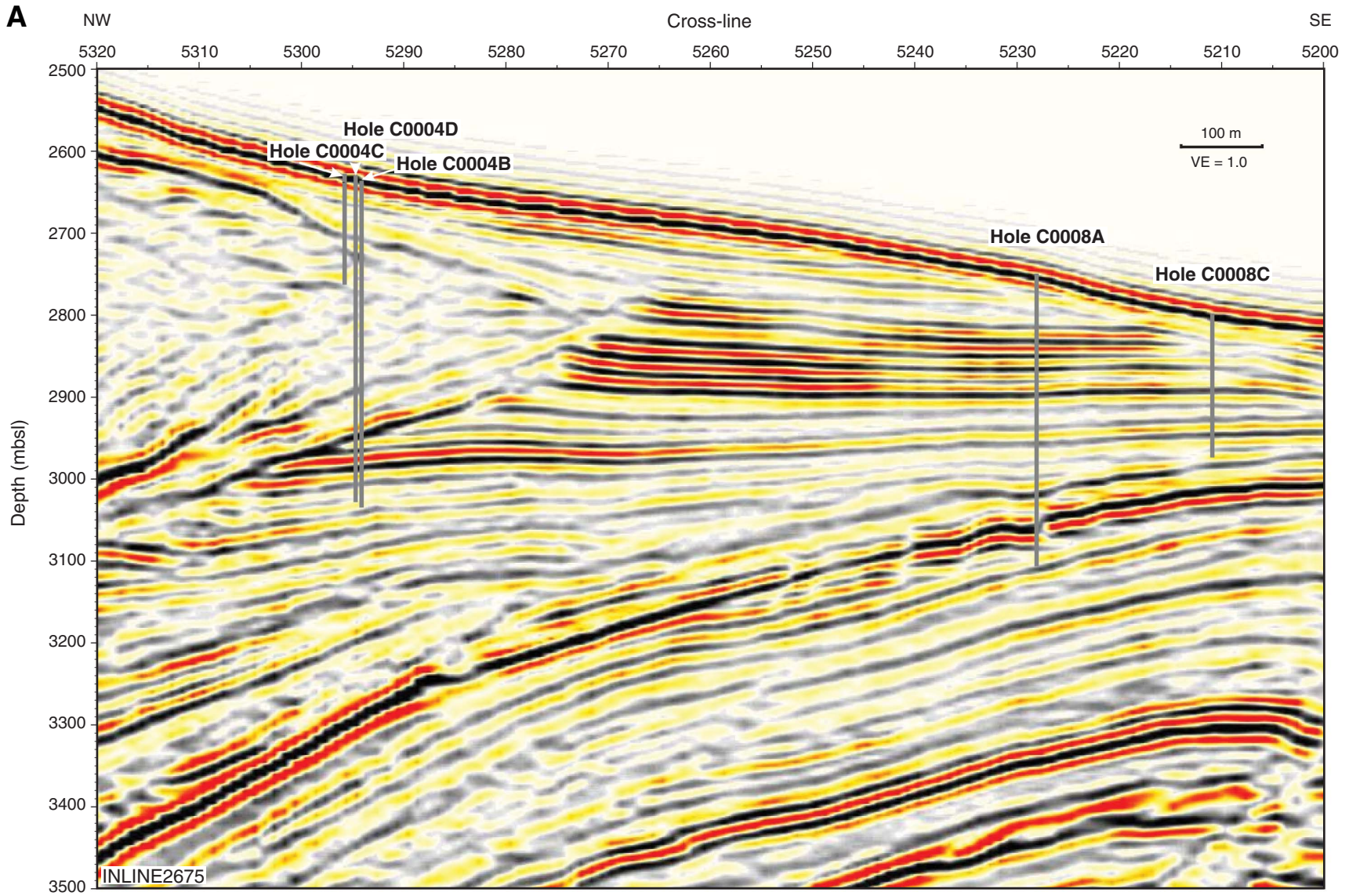
Publication: 11 March 2009  
MS 314315316-133

Figure F1. Site C0004 drill hole locations. Solid lines = three-dimensional seismic profile coverage.





**Figure F2.** 3-D seismic profile crossing Site C0004 and nearby Site C0008 (Moore et al., 2007; see Moore et al.). A. Inline 2675. VE = vertical exaggeration. (Continued on next page.)





**Figure F3.** Core recovery and sand and silt distribution, Holes C0004C and C0004D. **A.** Core recovery and lithologic units, Holes C0004C and C0004D. CSF = core depth below seafloor. (**Continued on next page.**)

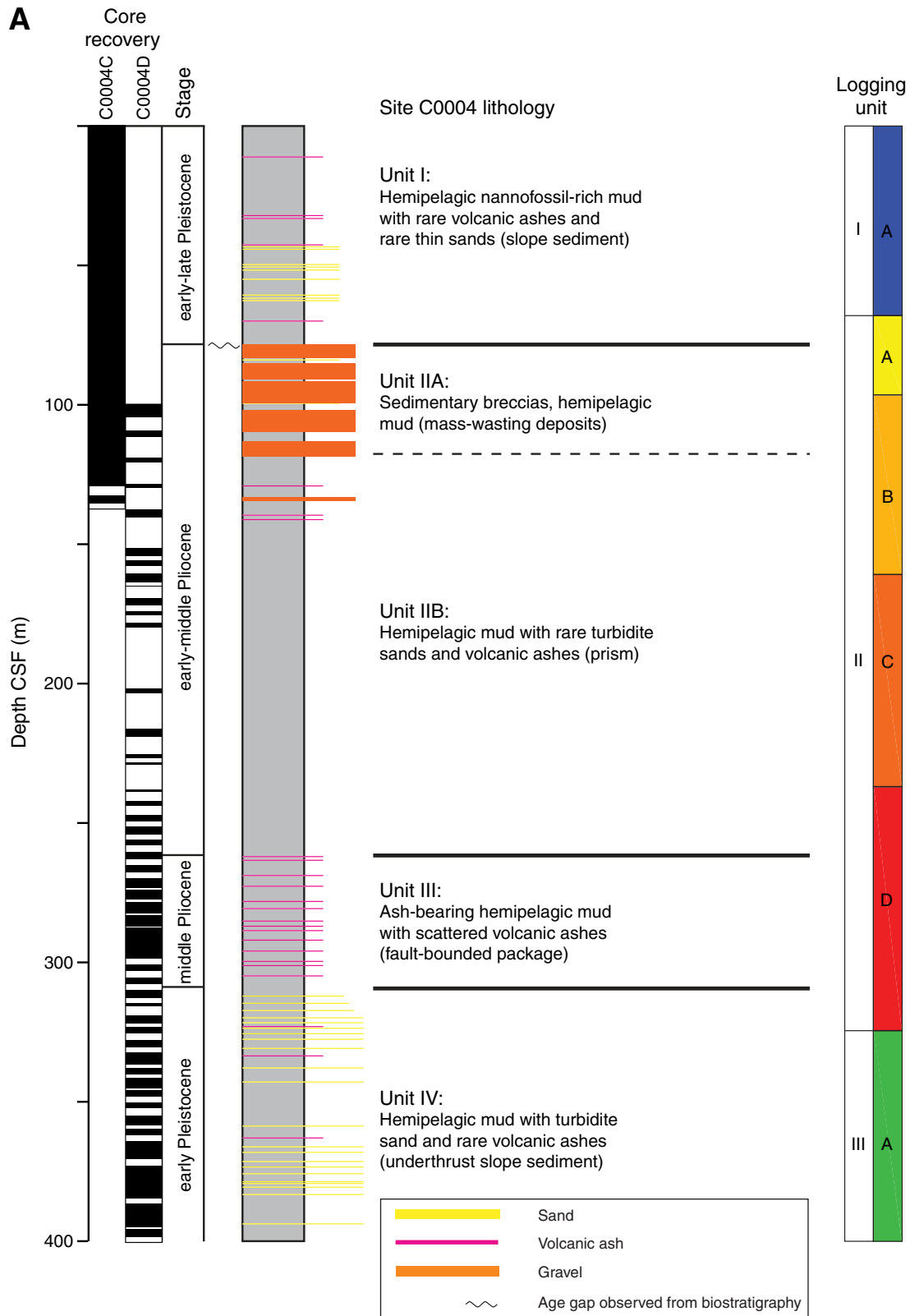
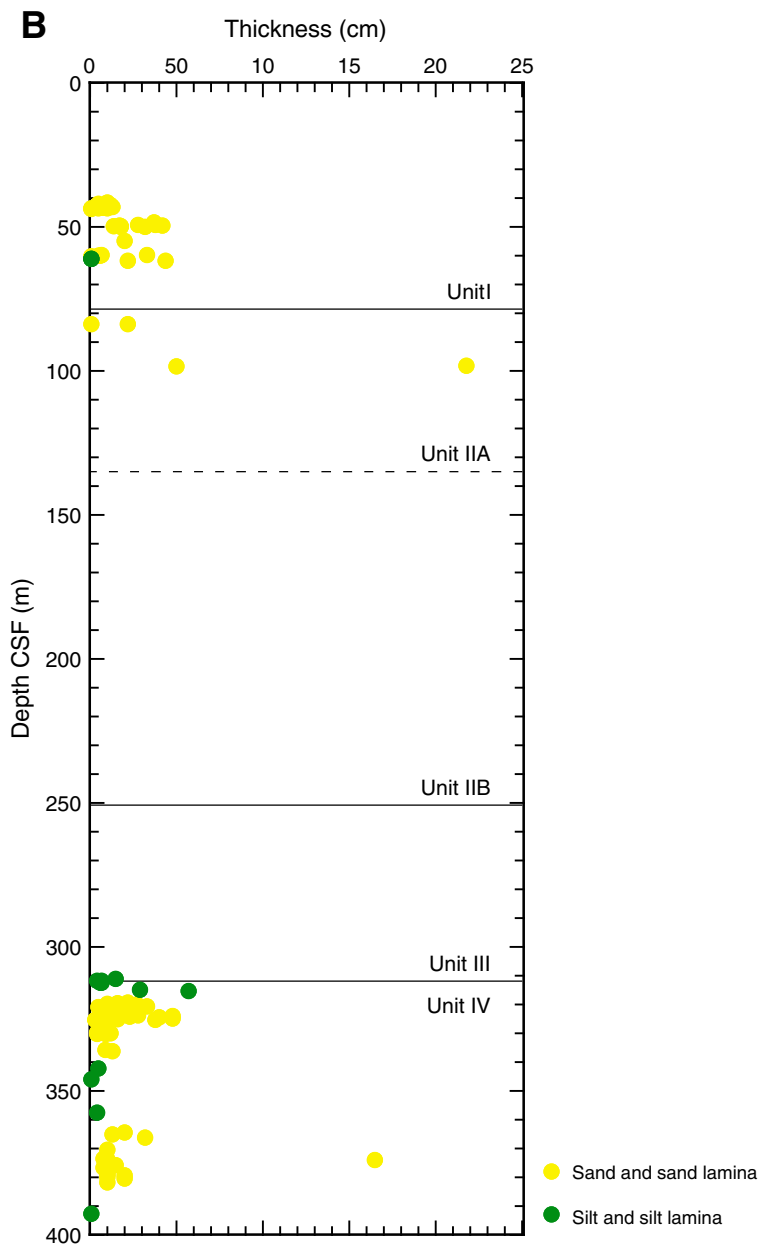
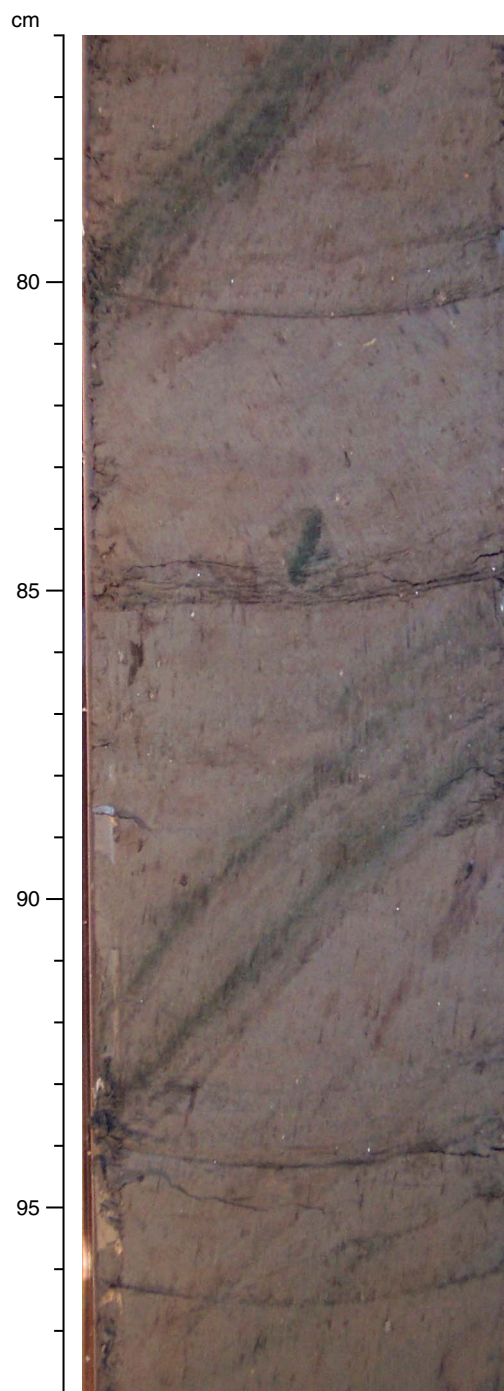


Figure F3 (continued). B. Distribution of sand and silt.



**Figure F4.** Photograph of typical appearance of Unit I. Green color banding defining bedding tilted at 40° (interval 316-C0004C-9H-2, 80–95 cm; 75.1 m CSF).



**Figure F5.** Debris flow sediments interlaminated with horizontally bedded material containing layer-parallel trace fossils (interval 316-C0004C-1H-1, 0–80 cm). A. Core photo. B. X-ray CT image. C. Graphic representation.

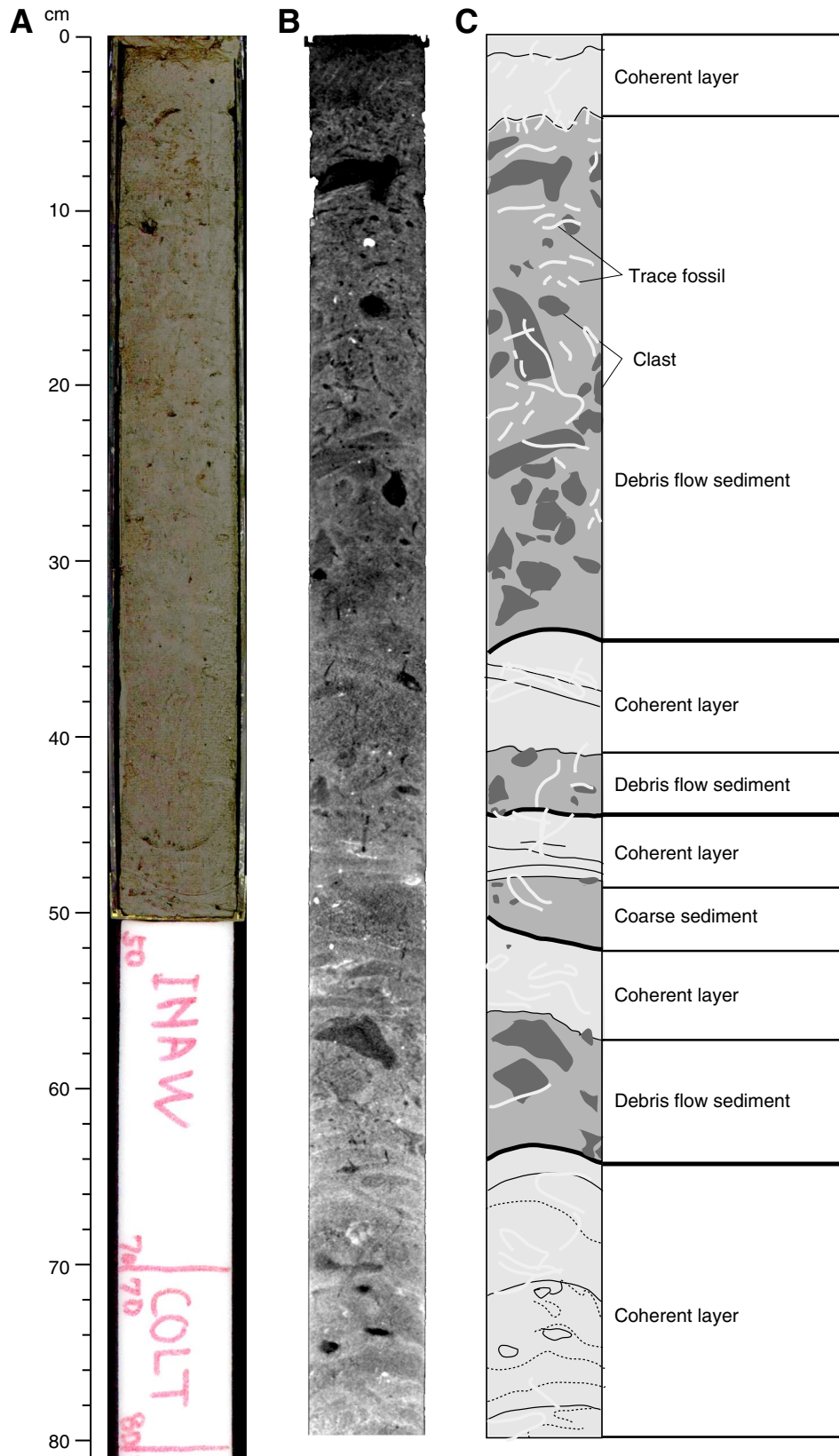
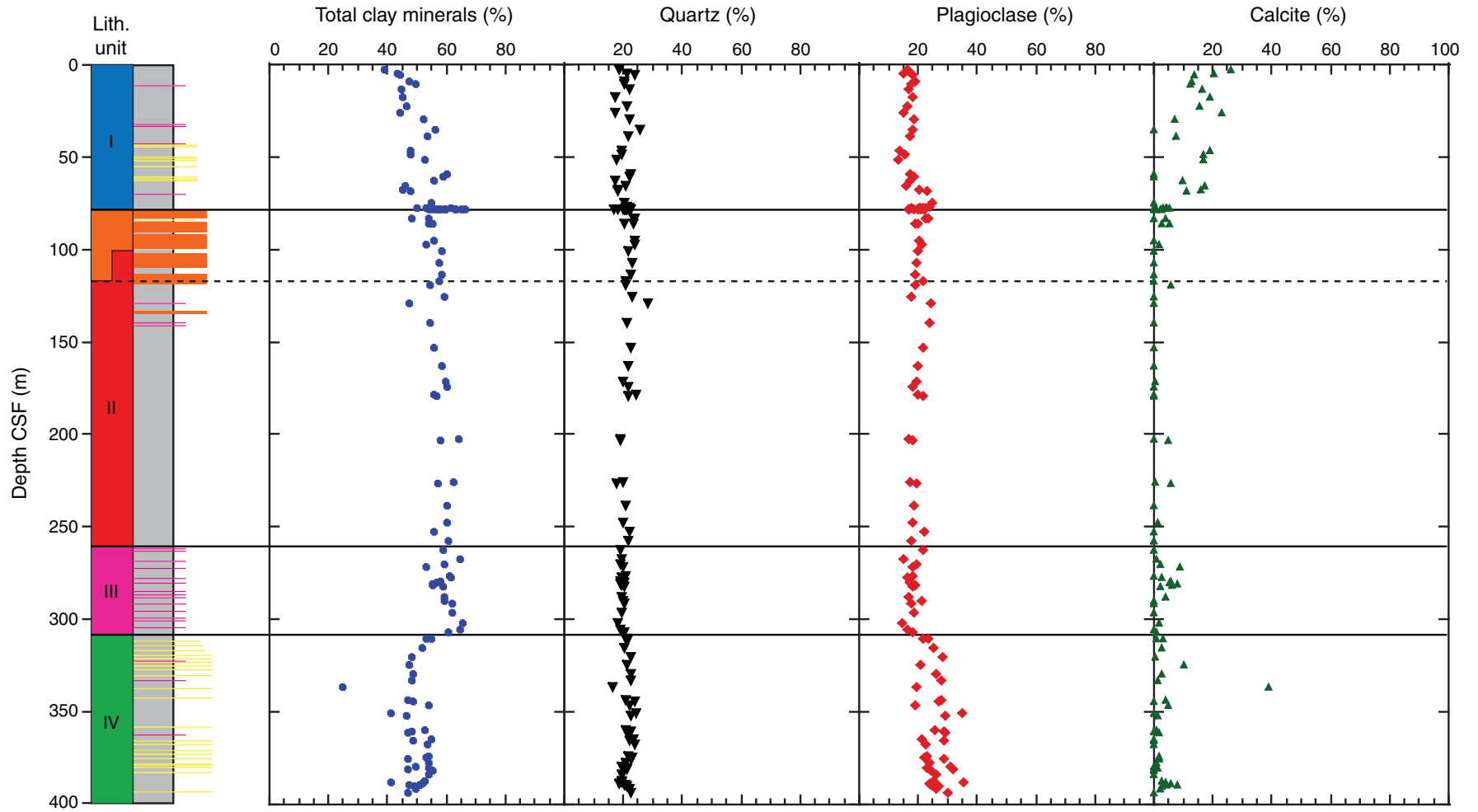
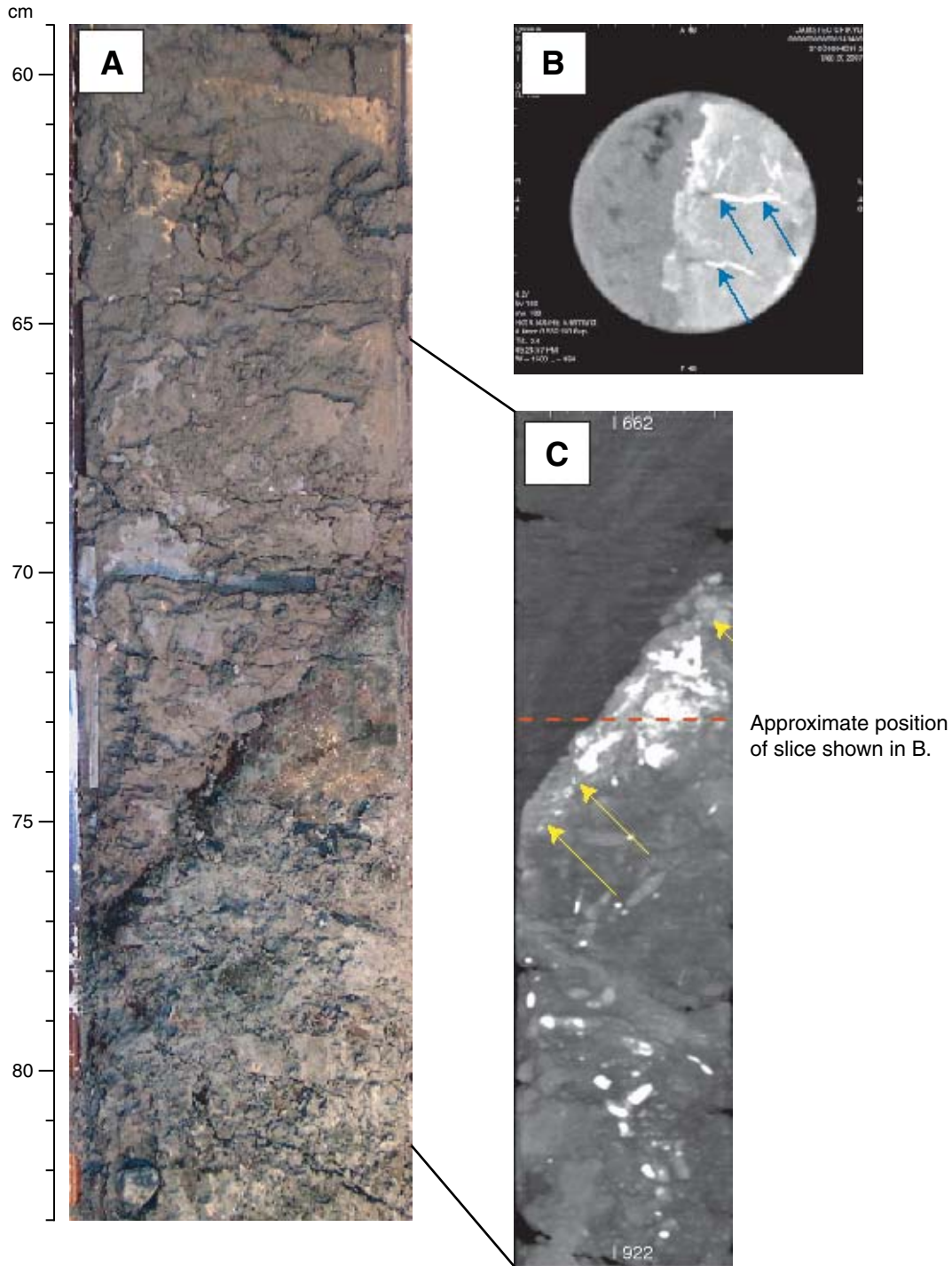




Figure F6. XRD data, Holes C0004C and C0004D. CSF = core depth below seafloor.



**Figure F7.** Unconformity between Units I and II (interval 316-C0004C-9H-5, 59–83). **A.** Visible light image. **B.** CT image of horizontal slice, looking down on partially pyrite-filled near-vertical fractures (blue arrows) in the breccia just below the unconformity. **C.** Semitransparent rendering of CT image showing variable density of mineralized breccia at the unconformity. The brightest regions correspond to pyrite mineralization and the medium bright region in the 5 mm just below the contact (yellow arrows) corresponds to an as-yet unidentified mineral that imparts a dark coloration to the rock.



**Figure F8.** X-ray fluorescence (XRF) scanning data for Ca and Fe across the unconformity (interval 316-C0004C-9H-5, 57–100 cm; 78.06 m CSF)

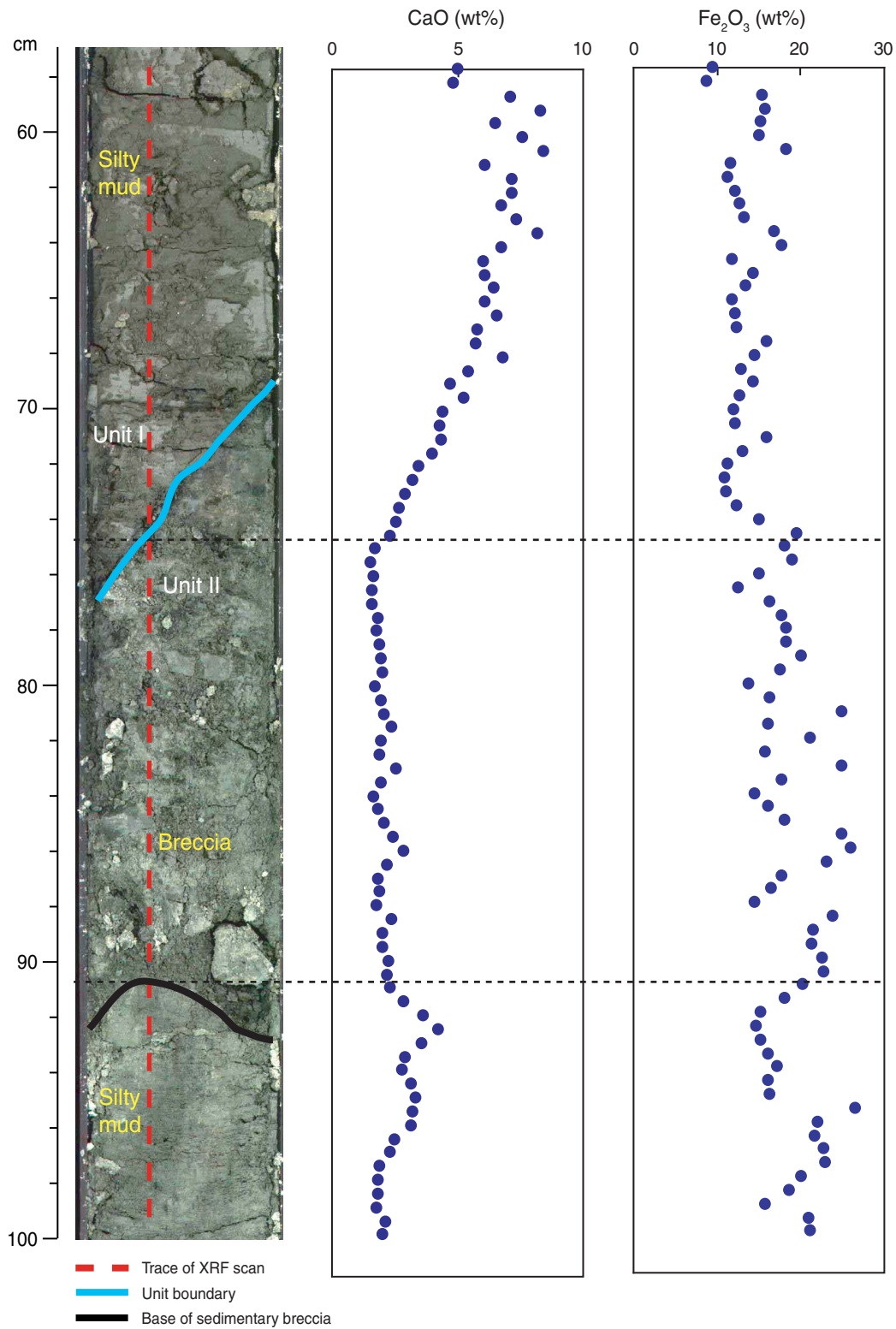


**Figure F9.** Volcanic ash occurrence. **A.** Depth distribution of ash layers, Holes C0004C and C0004D. **B.** Ash bed in Section 316-C0004D-31R-2. **C.** Typical ash bed, Section 316-C0004D-32R-1, 32 cm. CSF = core depth below seafloor.

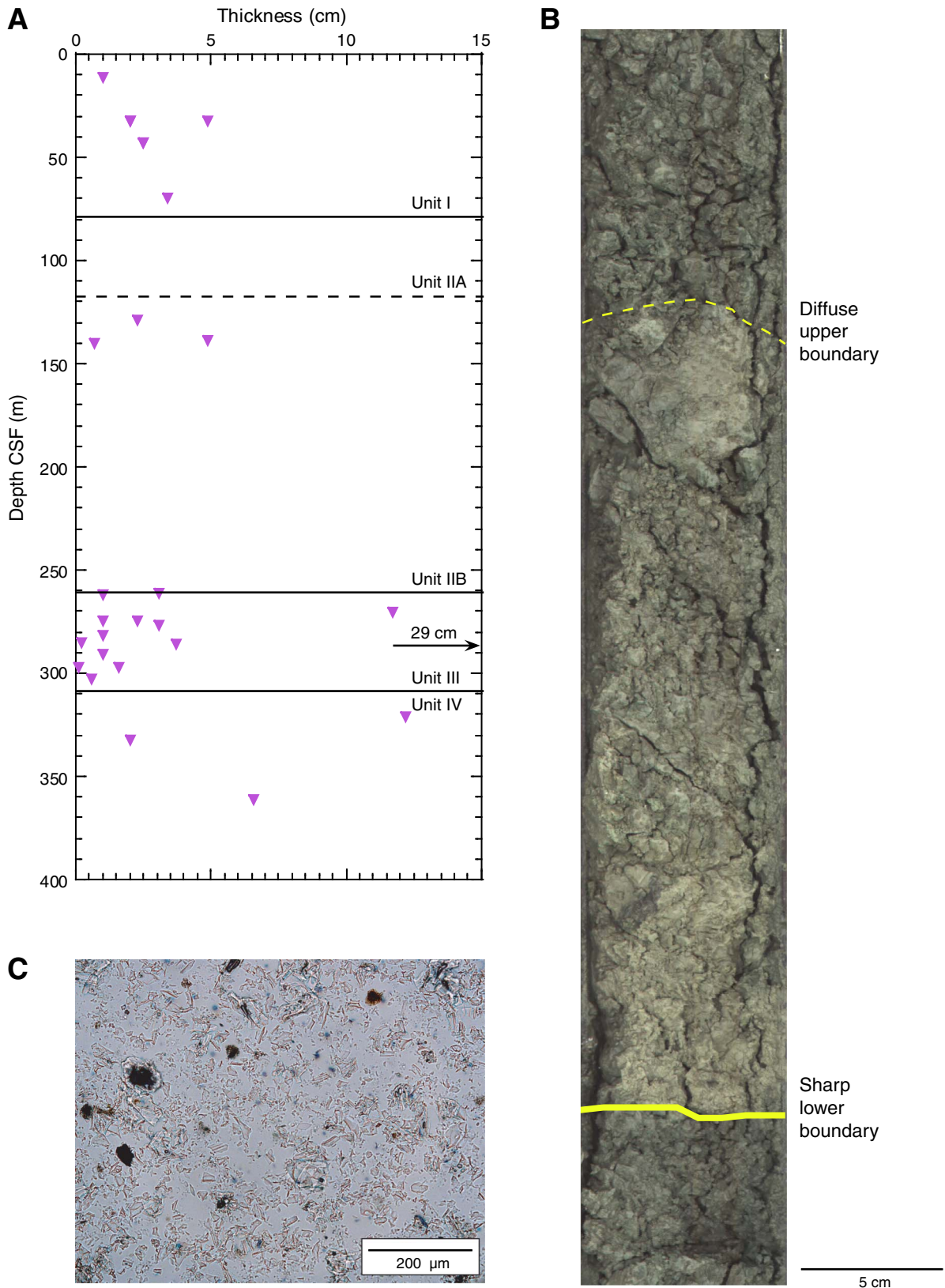


**Figure F10.** Photomicrograph of cubic-form pyrite at the unconformity (Section 316-C0004C-9H-5, 77 cm).

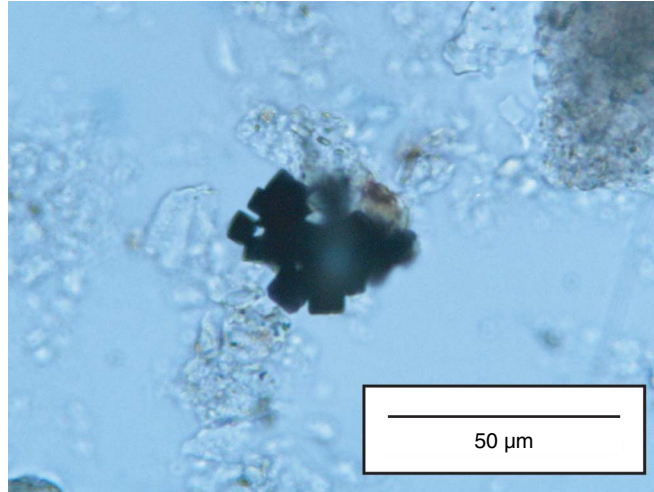


**Figure F11.** Close-up photograph of thin sandy/silty beds of Unit IV, Hole C0004D. CSF = core depth below seafloor.

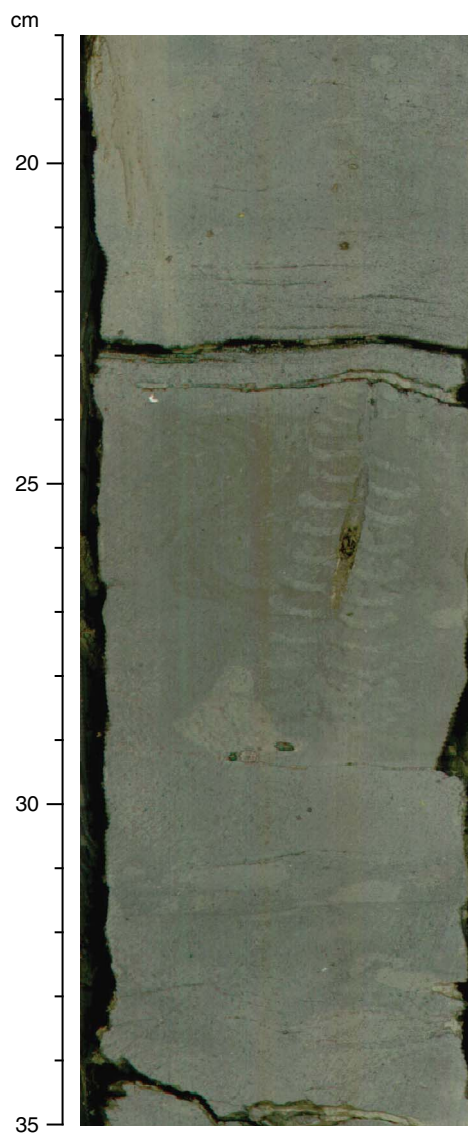


**Figure F12.** Photomicrograph of red-brown organic detritus of terrestrial origin (Section 316-C0004C-39R-1, 53 cm).

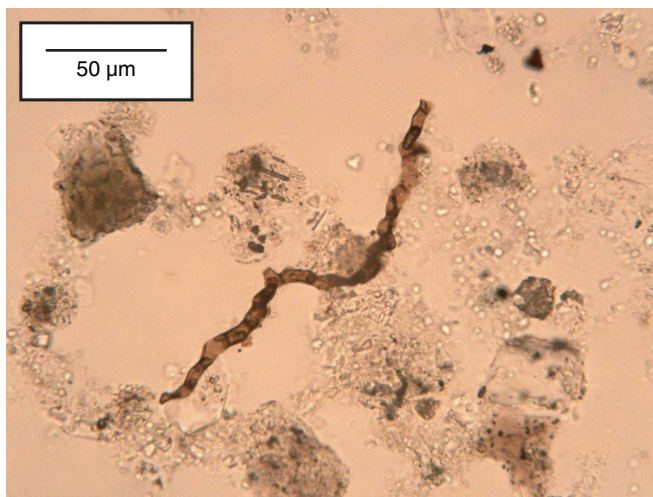


**Figure F13.** Computed tomography (CT) number vs. depth, Holes C0004C and C0004D. Average value for each core obtained from ~70 measurements at 4–10 cm intervals. CSF = core depth below seafloor.

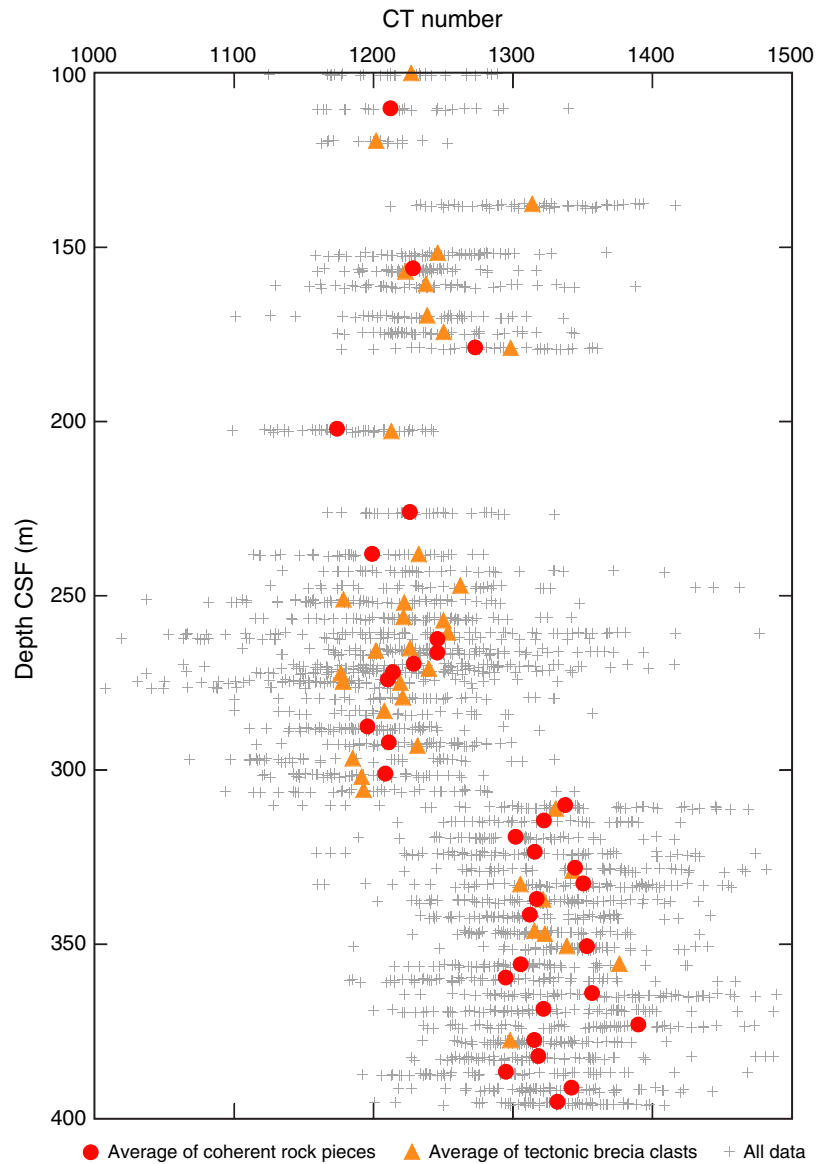


**Figure F14.** Distribution of bedding dip angles and deformation structures with depth. Shaded band = fractured/brecciated zone associated with the splay fault. Two inversions of biostratigraphic ages occur near the upper and lower boundaries of the fractured/brecciated zone. Note the relatively small number of structural measurement in the prism sediments at 100–256 m core depth below seafloor (CSF) because of drilling-induced brecciation and poor core recovery.

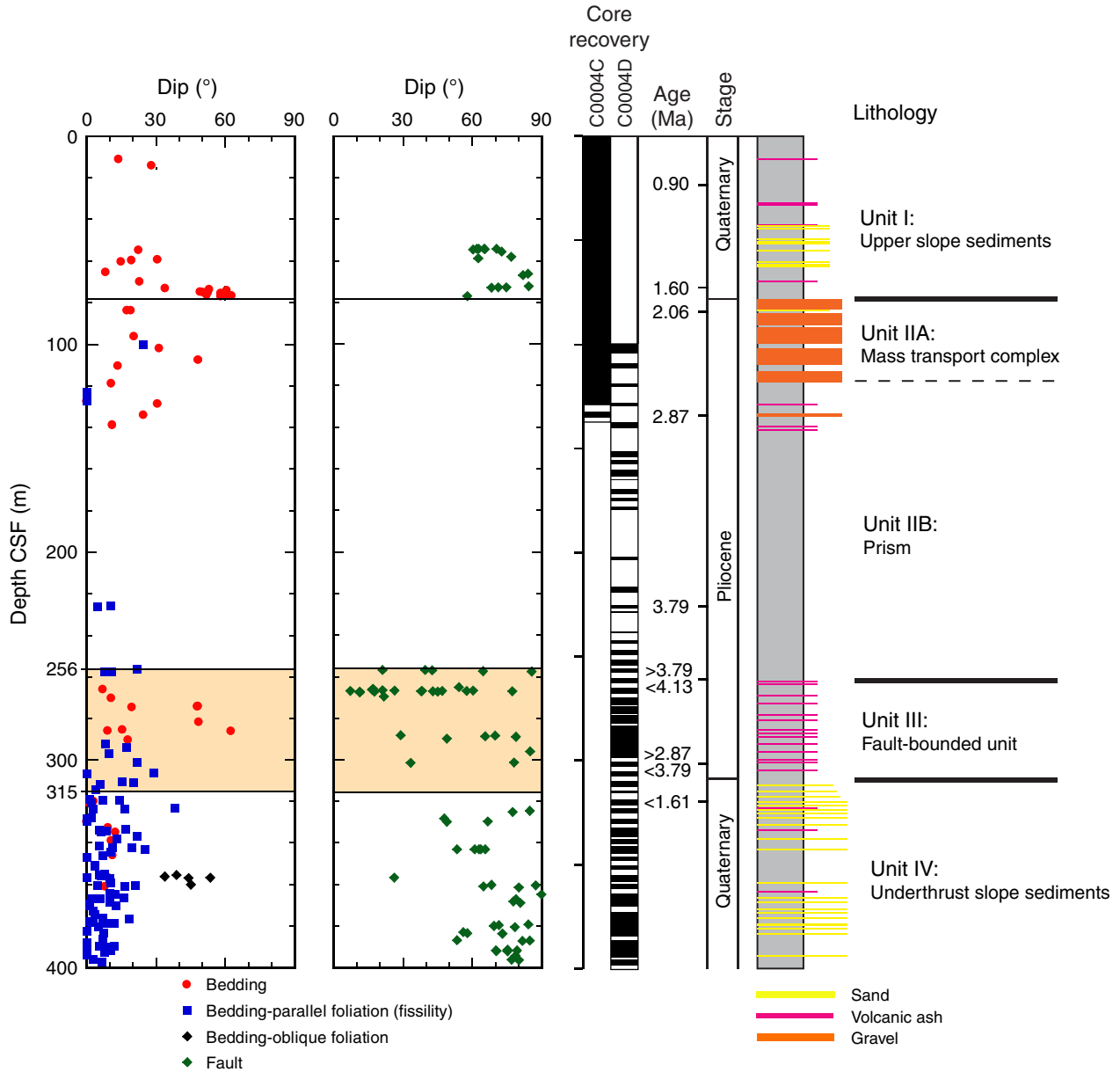
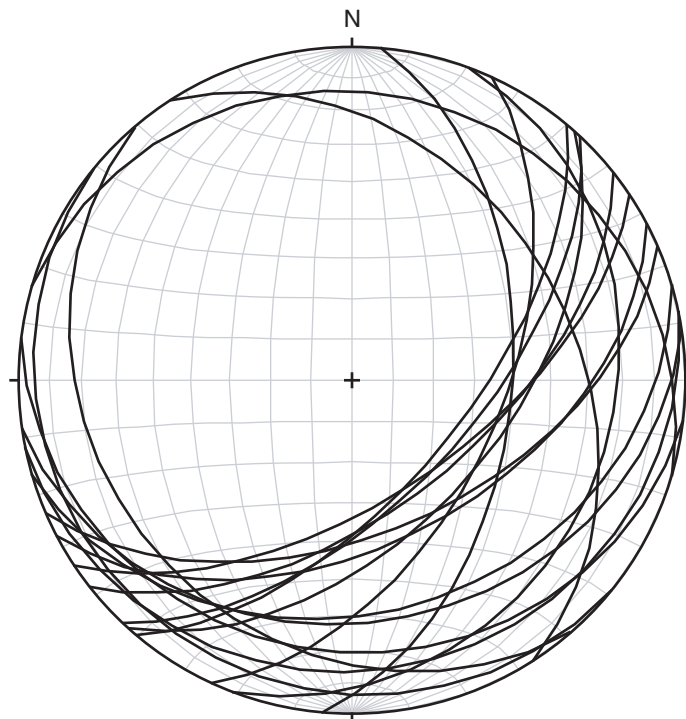


Figure F15. Lower-hemisphere equal-area projections of bedding surfaces in slope sediments.



**Figure F16.** Normal faults in slope sediments. A. Interval 316-C0004C-7H-2, 31–43 cm. B. Interval 316-C0004C-8H-8, 75–86 cm.

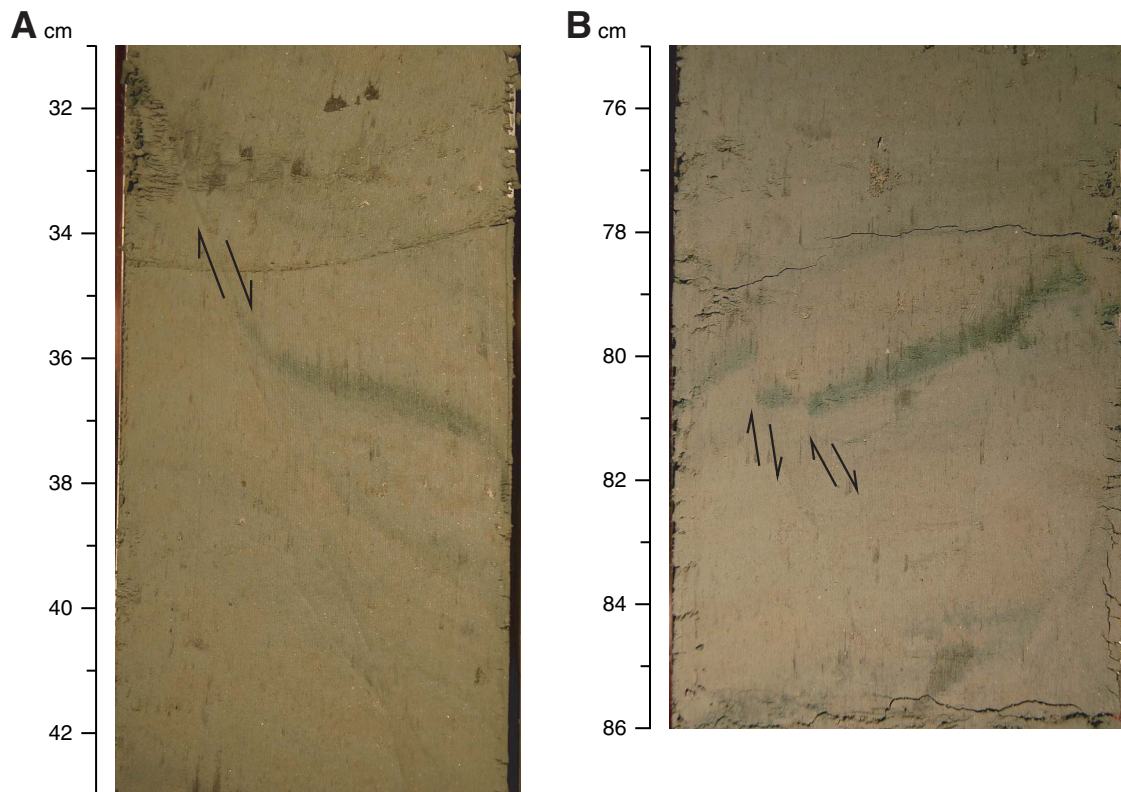
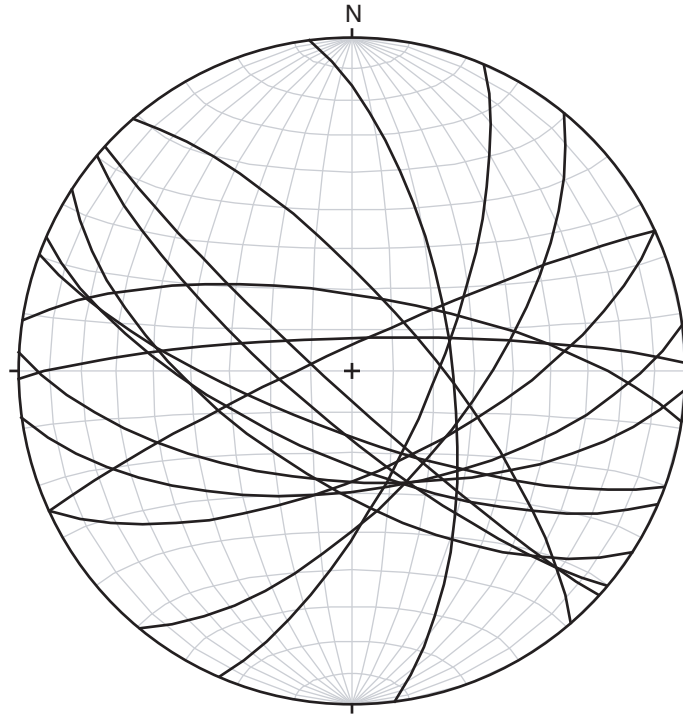
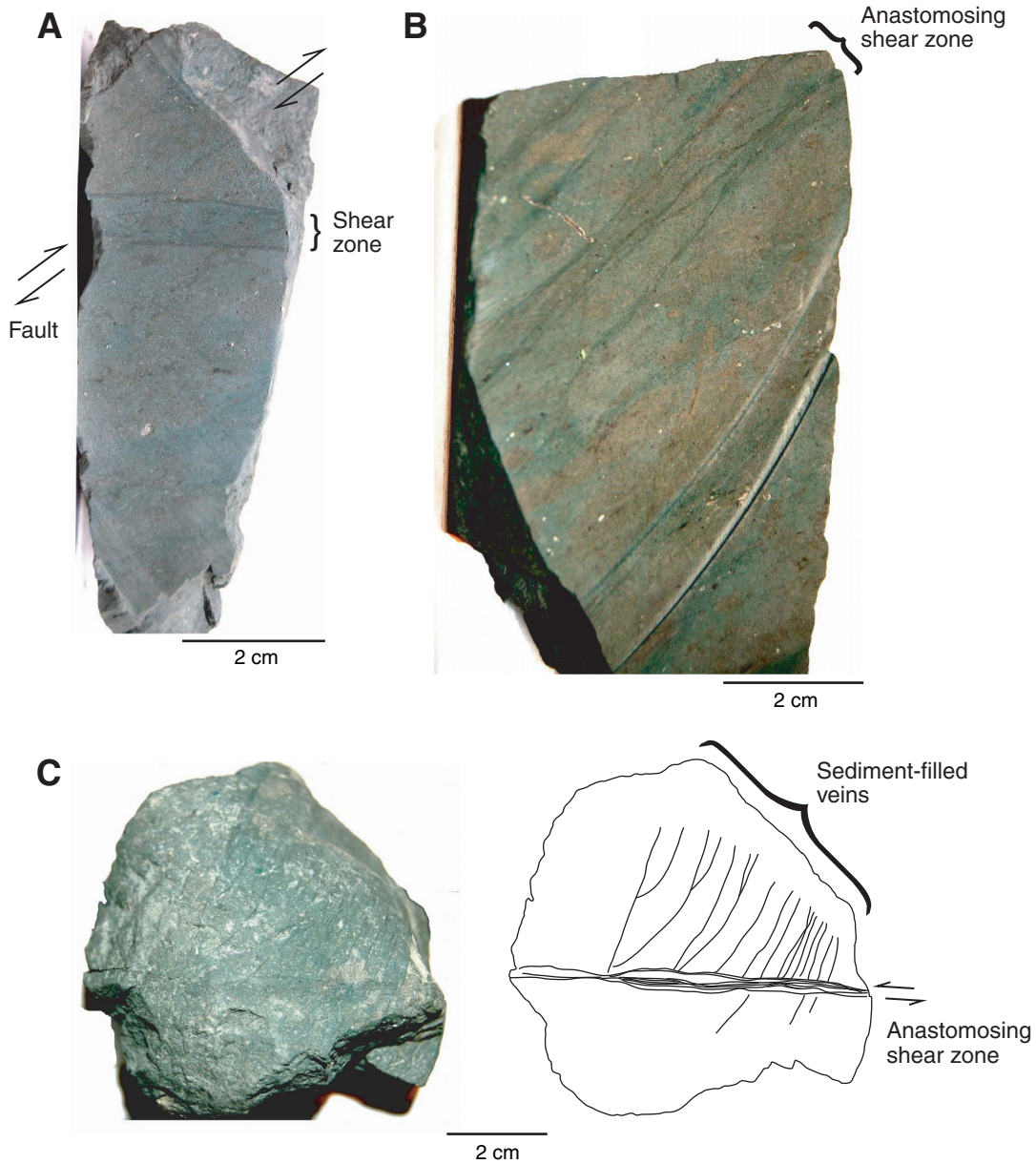


Figure F17. Lower-hemisphere equal-area projections of normal faults in slope sediments.



**Figure F18.** Faults, shear zones, and sediment-filled veins in prism sediments. **A.** Shear zones displaced by a fault with a reverse shear sense (interval 316-C0004D-13R-1, 77–85 cm). **B.** Anastomosing shear zones (interval 316-C0004D-13R-CC, 9–21 cm). **C.** Sediment-filled veins displaced by an anastomosing shear zone (interval 316-C0004D-12R-1, 50 cm). A sketch is also shown on the right.



**Figure F19.** Computed tomography (CT) images of shear zones. Note the relatively high CT number in shear zones with respect to the surrounding material. **A.** Shear zone (interval 316-C0004D-12R-1, 52.2 cm). **B.** Fragment in drilling-induced breccia in which two shear zones are developed (interval 316-C0004D-21R-1, 0–23 cm).

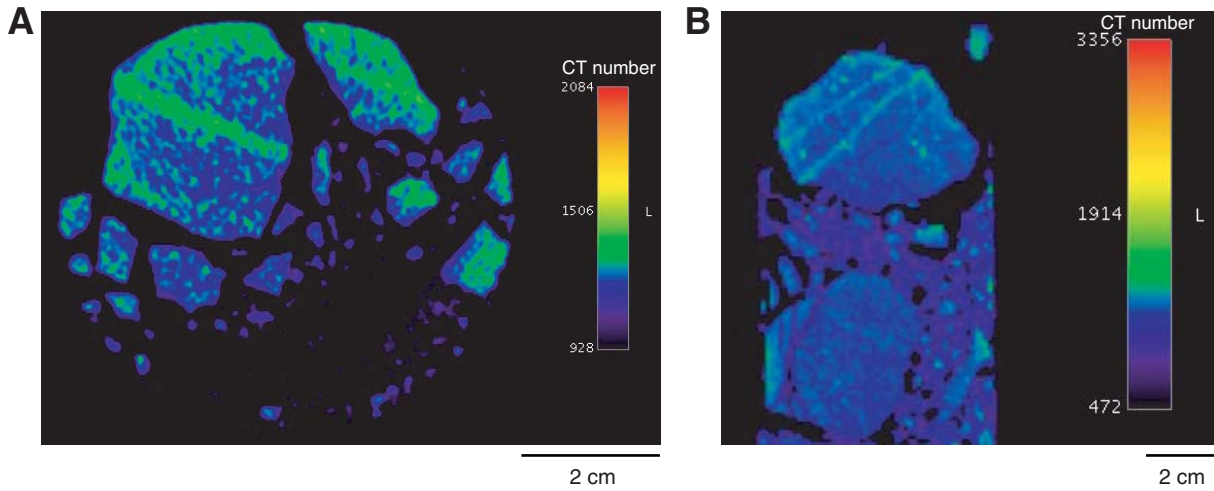


**Figure F20.** Distribution of structural elements in the splay fault zone. Plot of core recovery in fault zone is shown to the right. Core recovery is defined as percent volume of solid rock acquired relative to volume drilled in a single coring run. Calculation of solid volume assumes drilling-induced breccia has a 35% porosity that is filled with drilling mud and air. CSF = core depth below seafloor.

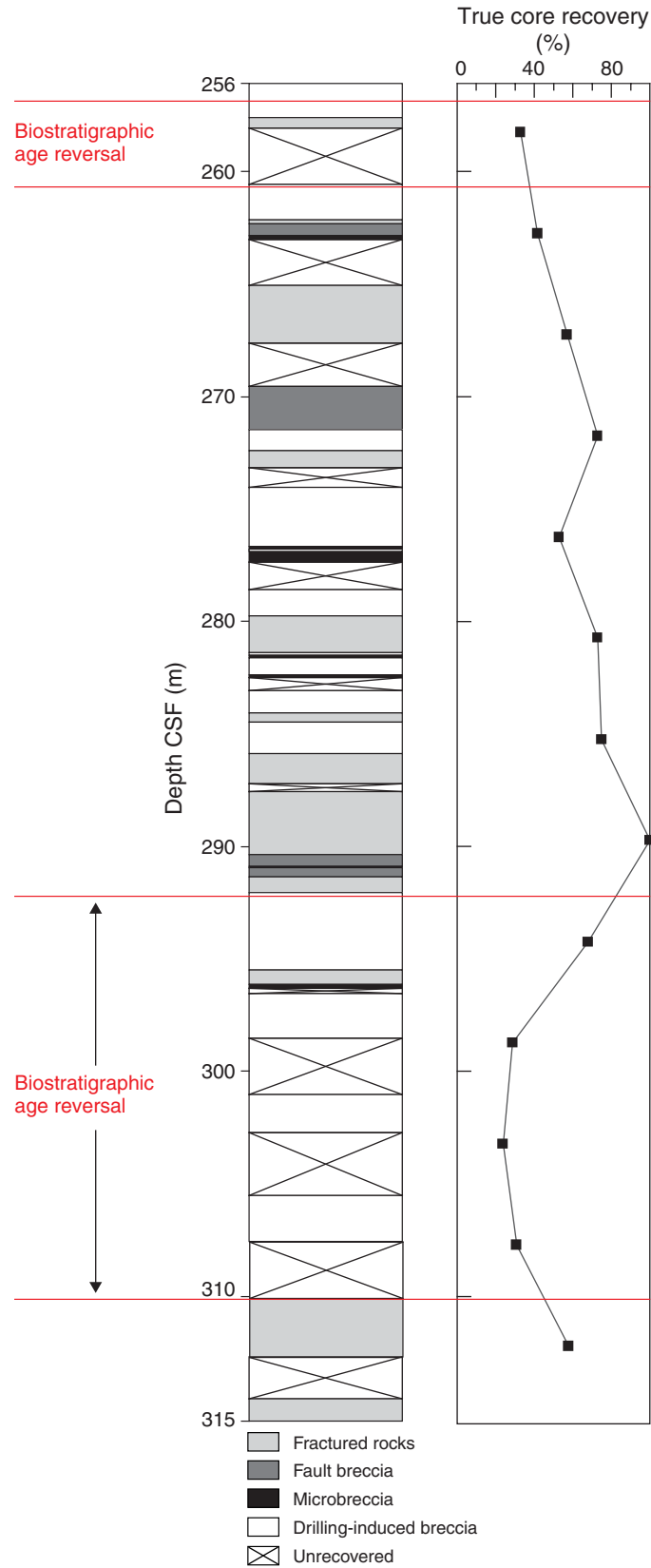


**Figure F21.** Appearance of fractured rock. **A.** Fractured rock in the core (interval 316-C0004D-26R-2, 10–33 cm). **B.** Fractured rock in the computed tomography (CT) image (interval 316-C0004D-28R-3, 0–65 cm).

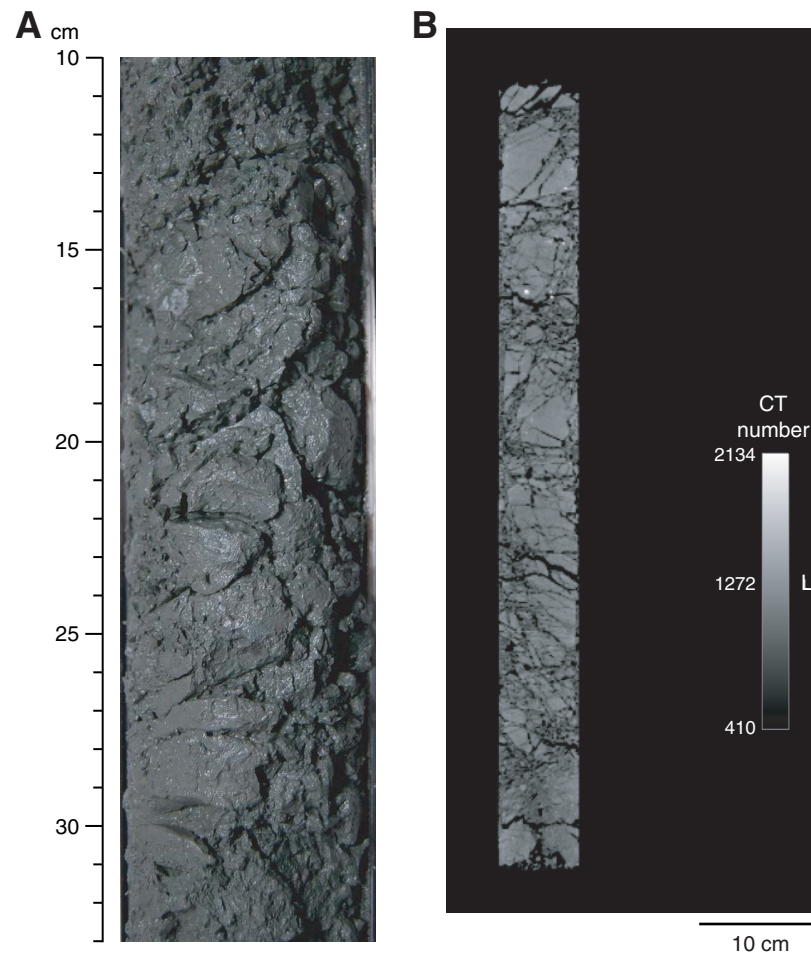


**Figure F22.** Lower-hemisphere equal-area projections of fracture surfaces. **A.** Fracture surfaces (great circles). **B.** Fractures on which the sense of shear can be determined. Fracture surfaces (great circles) with striae (dots) and slip vectors (arrows) show displacement of hanging wall relative to footwall.

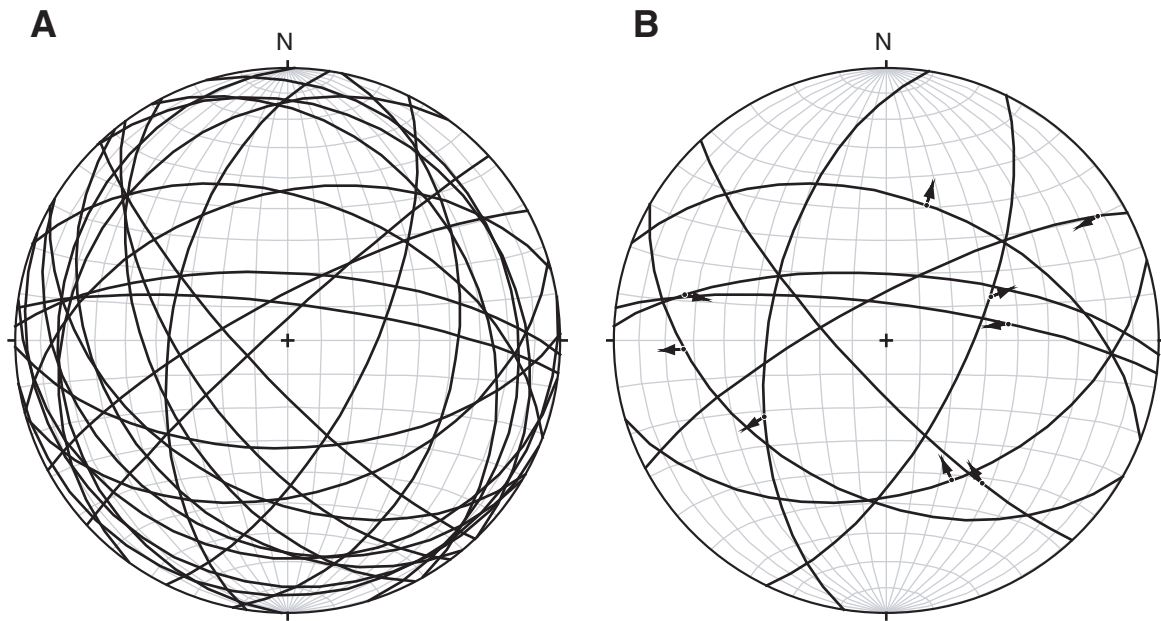


**Figure F23.** Core photograph of fractured and brecciated mudstone and ash. Note the preservation of an ash layer (double arrow) (interval 316-C0004D-31R-2, 99–131 cm).

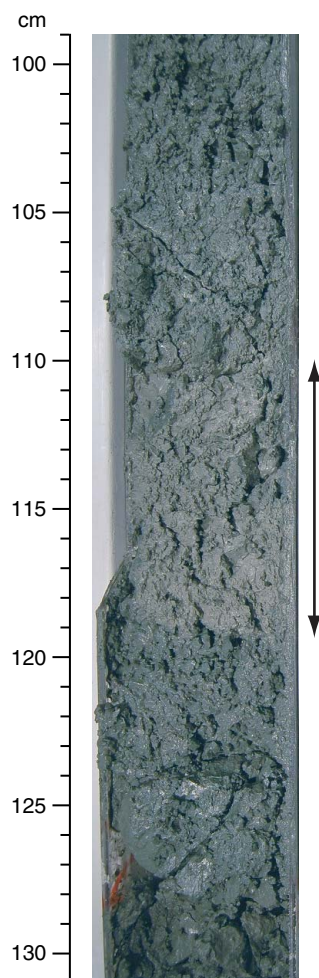
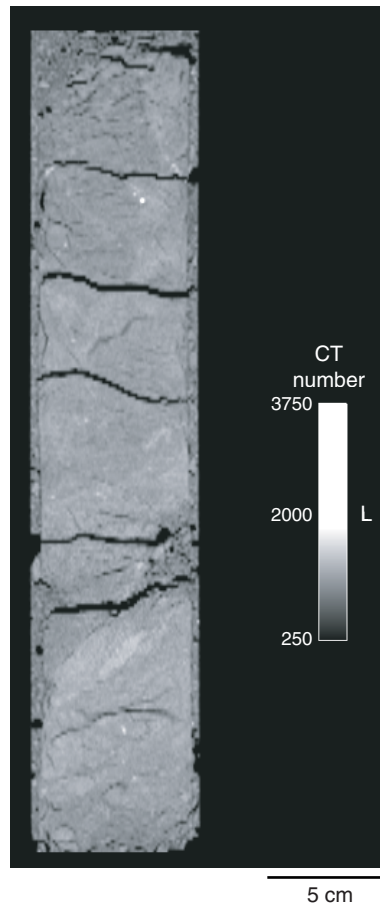
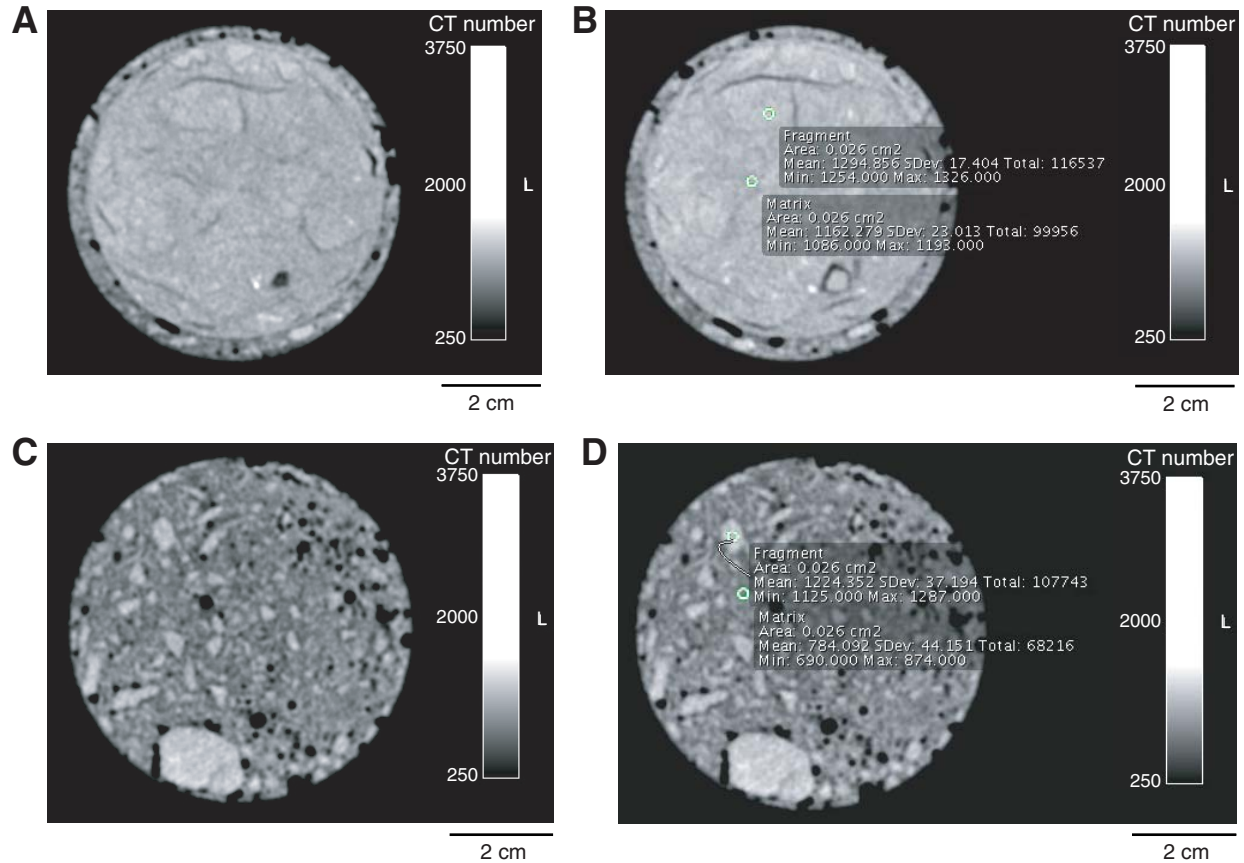


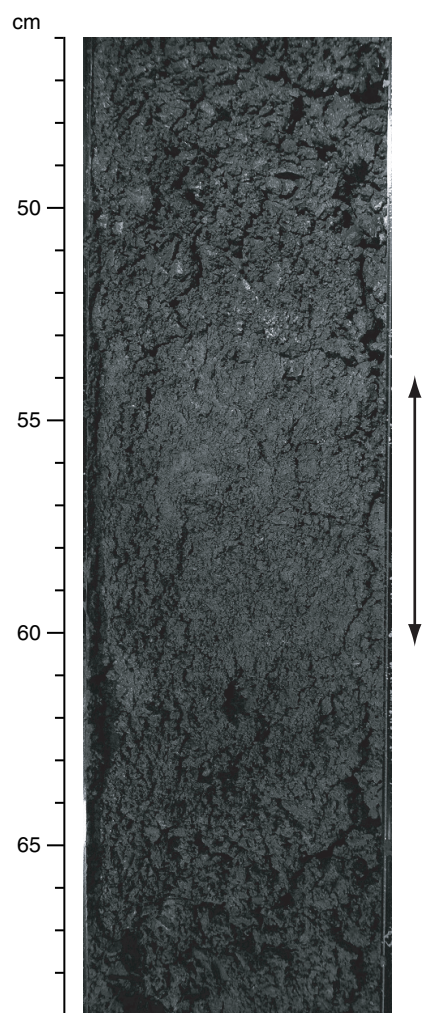
Figure F24. Computed tomography (CT) image of fault breccia (interval 316-C0004D-28R-2, 17–49 cm).



**Figure F25.** Representative appearance of fault breccia and drilling-induced breccia in computed tomography (CT) images. **A.** Slice of fault breccia cut perpendicular to core axis (interval 316-C0004D-28R-2, 45.13 cm). **B.** Same as A with CT numbers of matrix and fragment. Note the small contrast in CT number between matrix and fragment (1162 versus 1294). **C.** Slice of drilling-induced breccia cut perpendicular to core axis (interval 316-C0004D-28R-2, 49.75 cm). **D.** Same as C with CT numbers of matrix and fragment. Note the large contrast in CT numbers between matrix and fragment (784 vs. 1224).



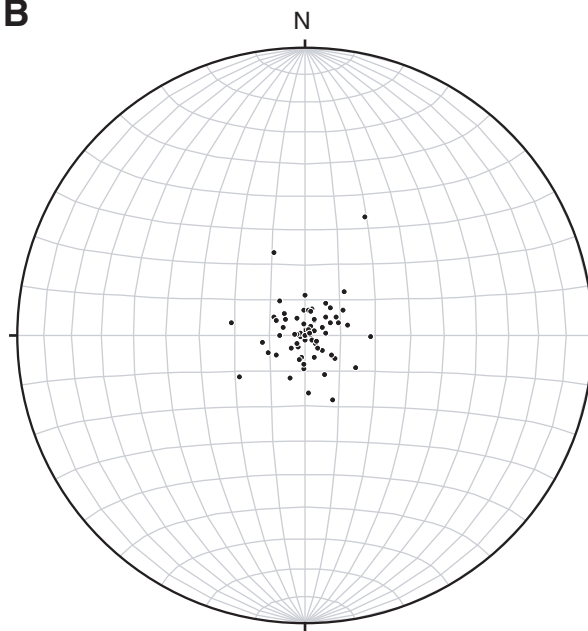
**Figure F26.** Photograph of microbreccia (double arrow) bounded above and below by fault breccia (interval 316-C0004D-32R-3, 46–69 cm).



**Figure F27.** Horizontal to gently dipping bedding in underthrust sediments. **A.** Fissility in siltstone (interval 316-C0004D-56R-1, 126–135 cm). **B.** Lower-hemisphere equal-area projections of poles to bedding and fissility in underthrust sediments.

**A**

2 cm

**B**

**Figure F28.** Lower-hemisphere equal-area projections of faults in underthrust sediments. **A.** Poles to fault planes. **B.** Faults on which the sense of shear can be determined. Fault planes (great circles) with striae (dots) and slip vectors (arrows) show displacement of hanging wall relative to footwall.

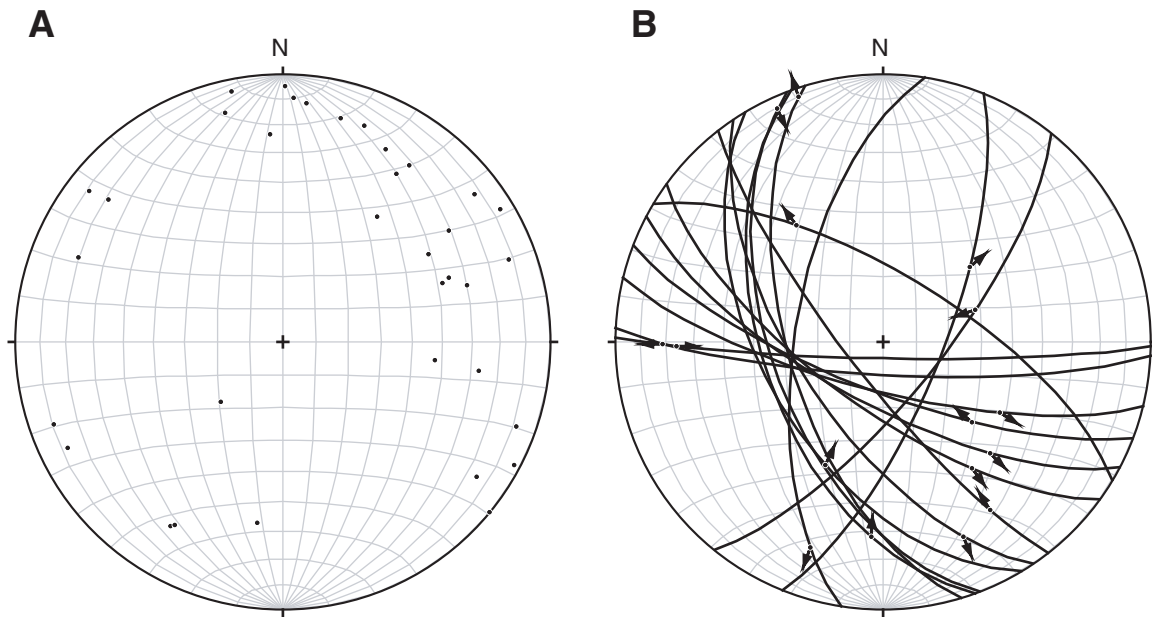
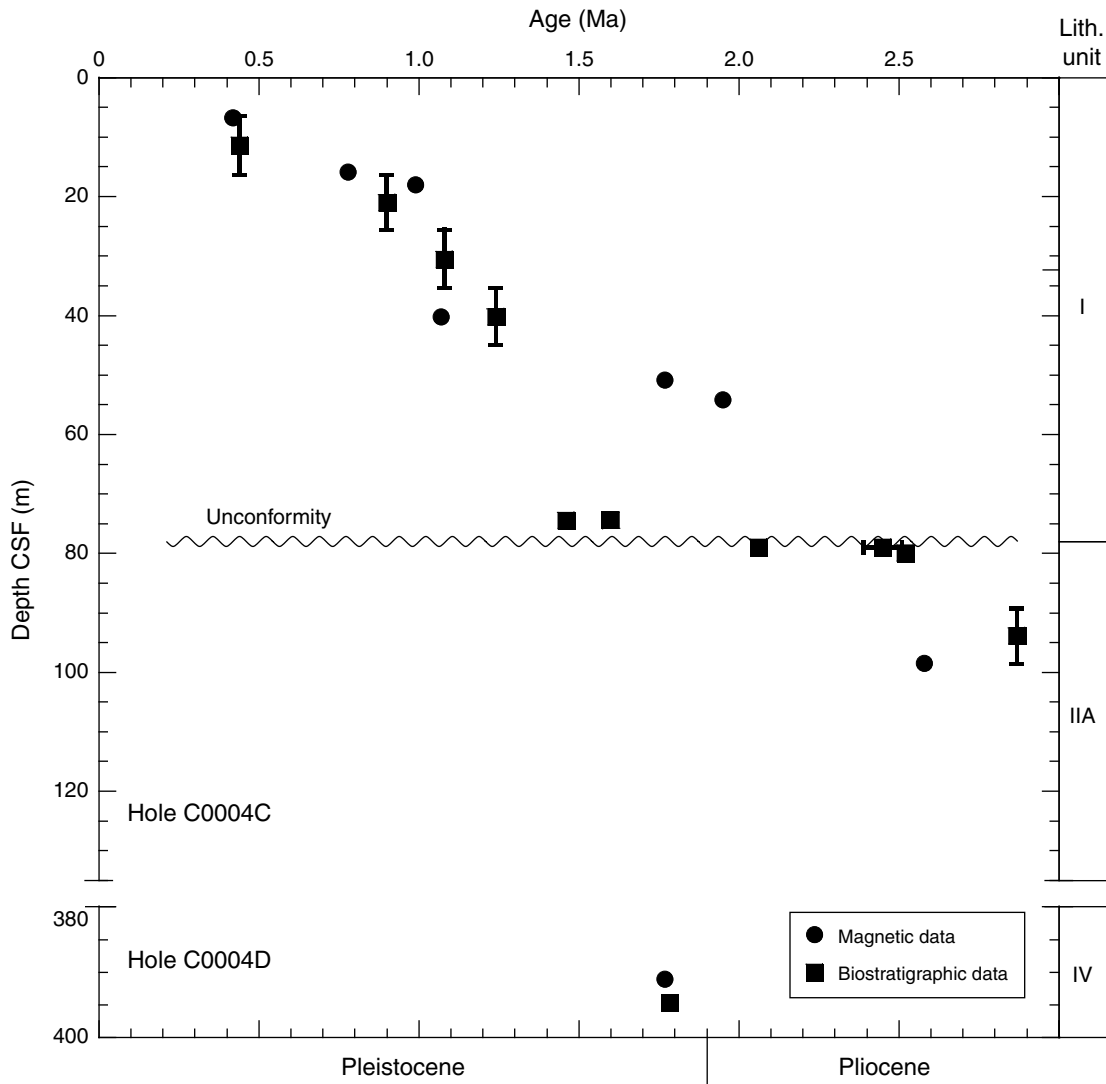
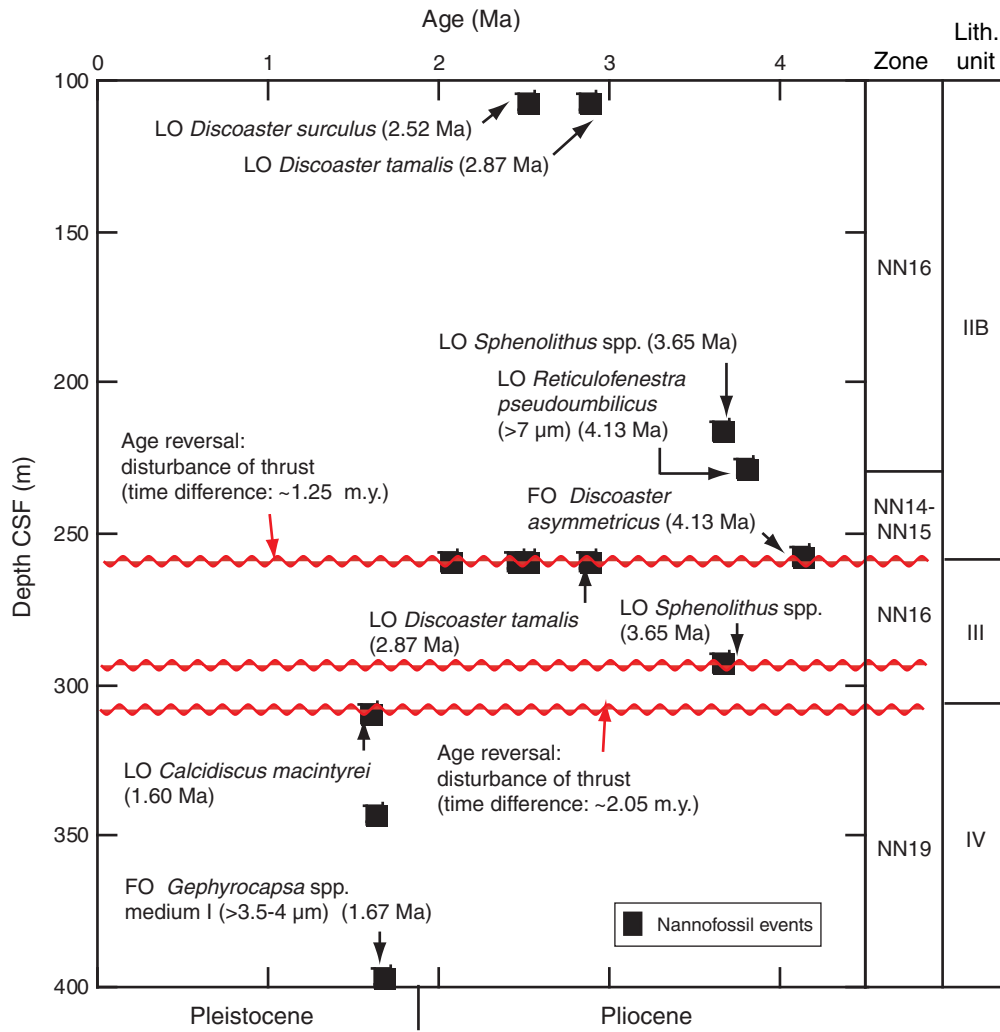


Figure F29. Depth vs. age profiles, Holes C0004C and C0004D. Paleomagnetic data are listed in Table T10. CSF = core depth below seafloor.



**Figure F30.** Nannofossil biostratigraphic ages vs. depth, Hole C0004D. CSF = core depth below seafloor. FO = first occurrence, LO = last occurrence.



**Figure F31.** Downhole synthesis of radiolarian zones in Hole C0004 and preservation (based on spongy and highly silicified shells), correlated with lithologic units. Stages are based on nannofossil occurrence. CSF = core depth below seafloor. LO = last occurrence.

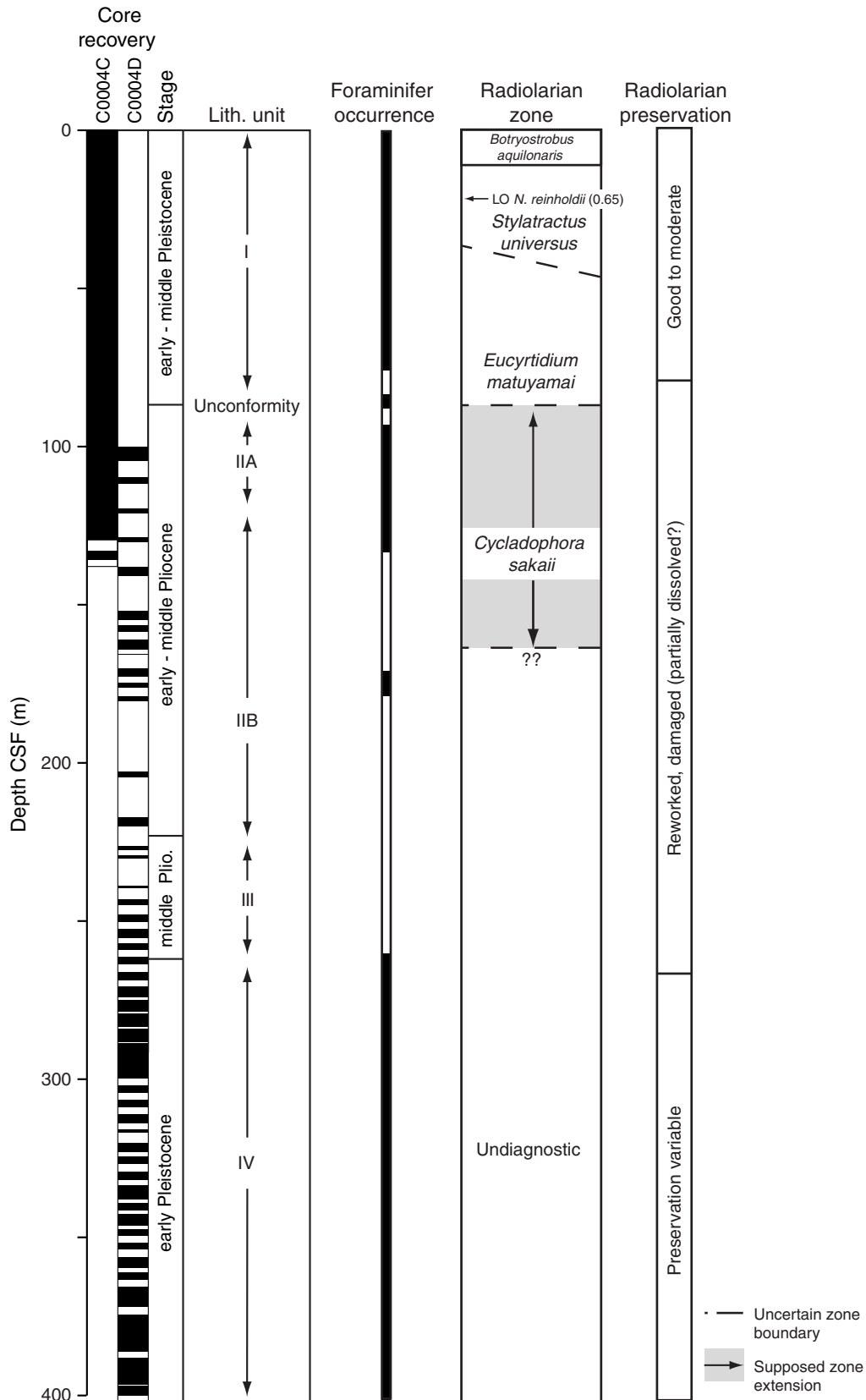


**Figure F32.** Magnetic susceptibility and remanent magnetization before (green) and after (purple, red, and blue) 40 mT alternating-field (AF) demagnetization. (A) Magnetic susceptibility, (B) intensity, (C) inclination, and (D) declination of archive halves, Hole C0004C. NRM inclinations are biased toward high positive inclinations, suggesting that drilling-induced magnetization is present. AF demagnetization to 40 mT can effectively remove drilling-induced magnetization, as indicated by changes in inclination and intensity. CSF = core depth below seafloor.

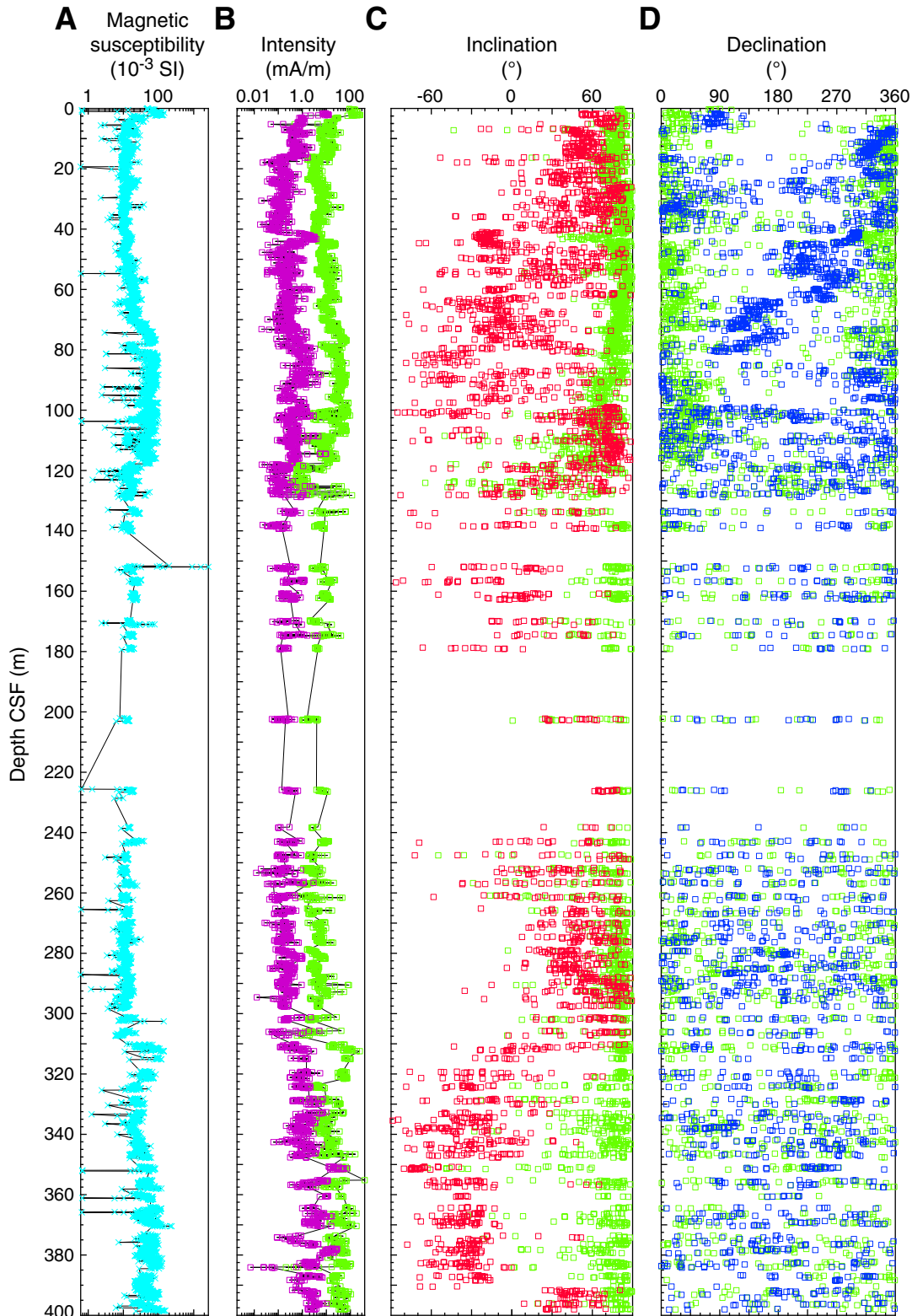


**Figure F33.** Vector endpoint and stereonet magnetization directions showing the results of AF and thermal demagnetization for sediments from (A) Sample 316-C0004C-10H-4, 45–47 cm, (B) Sample 316-C0004C-9H-3, 90–92 cm, and (C) Sample 316-C0004D-52R-2, 39–41 cm, showing removal of a normal component of magnetization due to drilling and isolation of a more stable reversed component that is decaying toward the origin of the vector plot. Black and white squares = projection of magnetization vector endpoint on the horizontal and vertical planes, respectively. NRM = natural remanent magnetization.

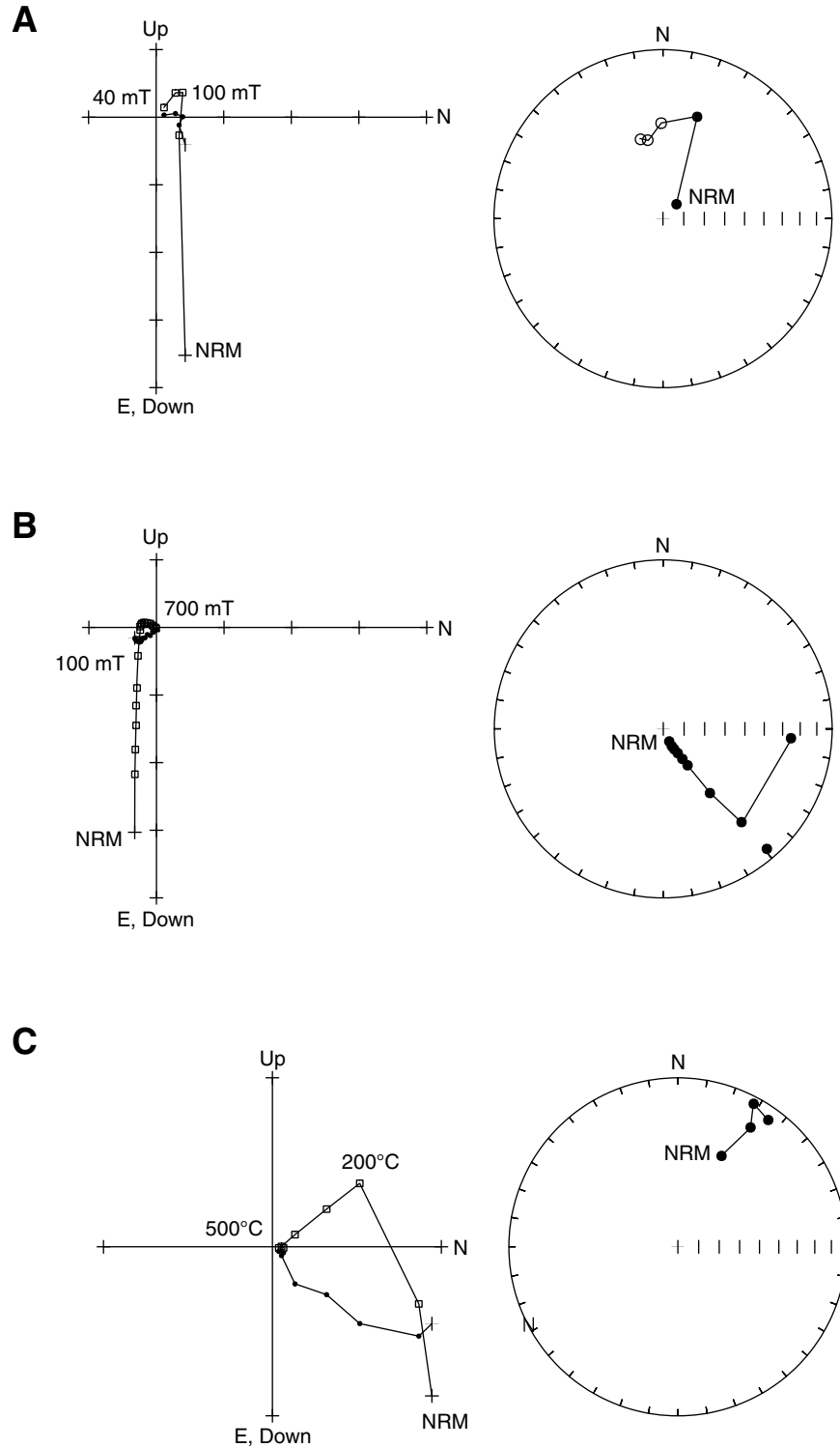


**Figure F34.** Variation of stable magnetic inclination and declination for sediments at 37–47 m core depth below seafloor (CSF), Hole C0004C. Note that after demagnetization at 40 mT, the reversal indicated by the difference in inclination polarity is confirmed by the nearly 180° change in declination, adding confidence to the polarity determination.

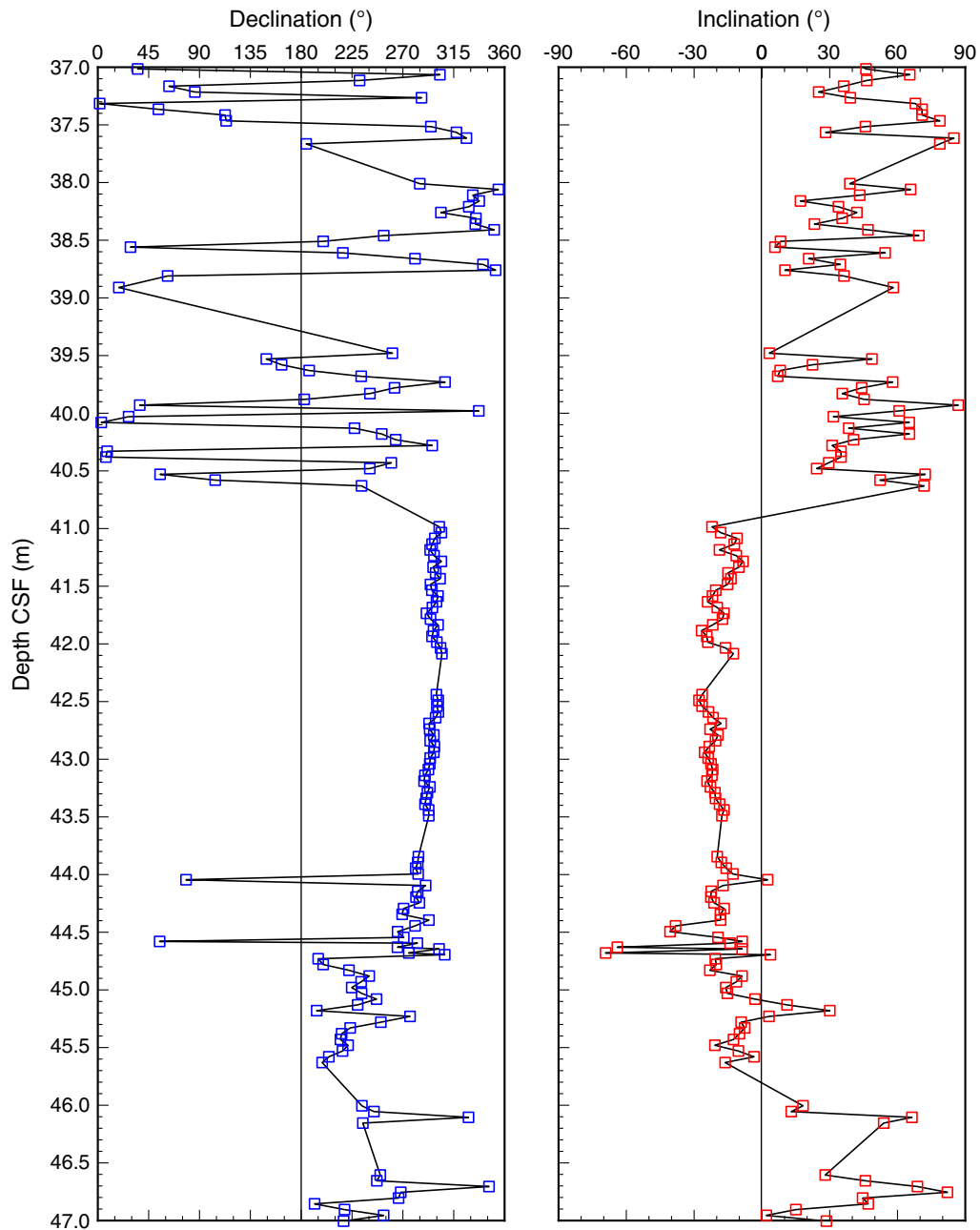


**Figure F35.** Nannofossil event markers, Hole C0004D. CSF = core depth below seafloor. Solid black line = top of Zones NN15–NN14.

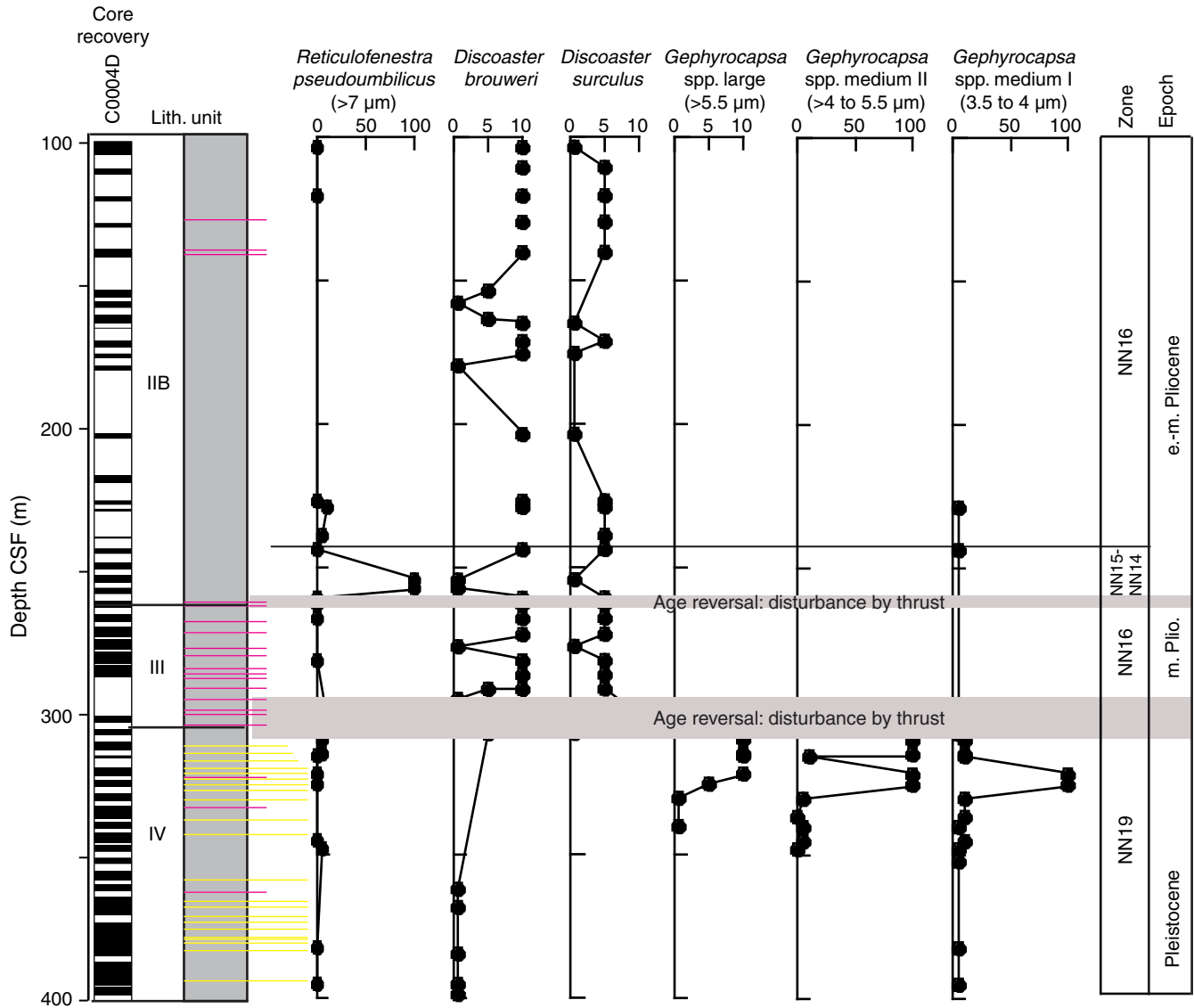


**Figure F36.** Downhole variation in stable magnetic inclination, inferred polarity, and biostratigraphic zones for sediments, Site C0004. Black areas = normal polarity, white areas = reversed polarity, hatched area = mixed polarity, questioned area = no data available. CSF = core depth below seafloor. AF = alternating field.

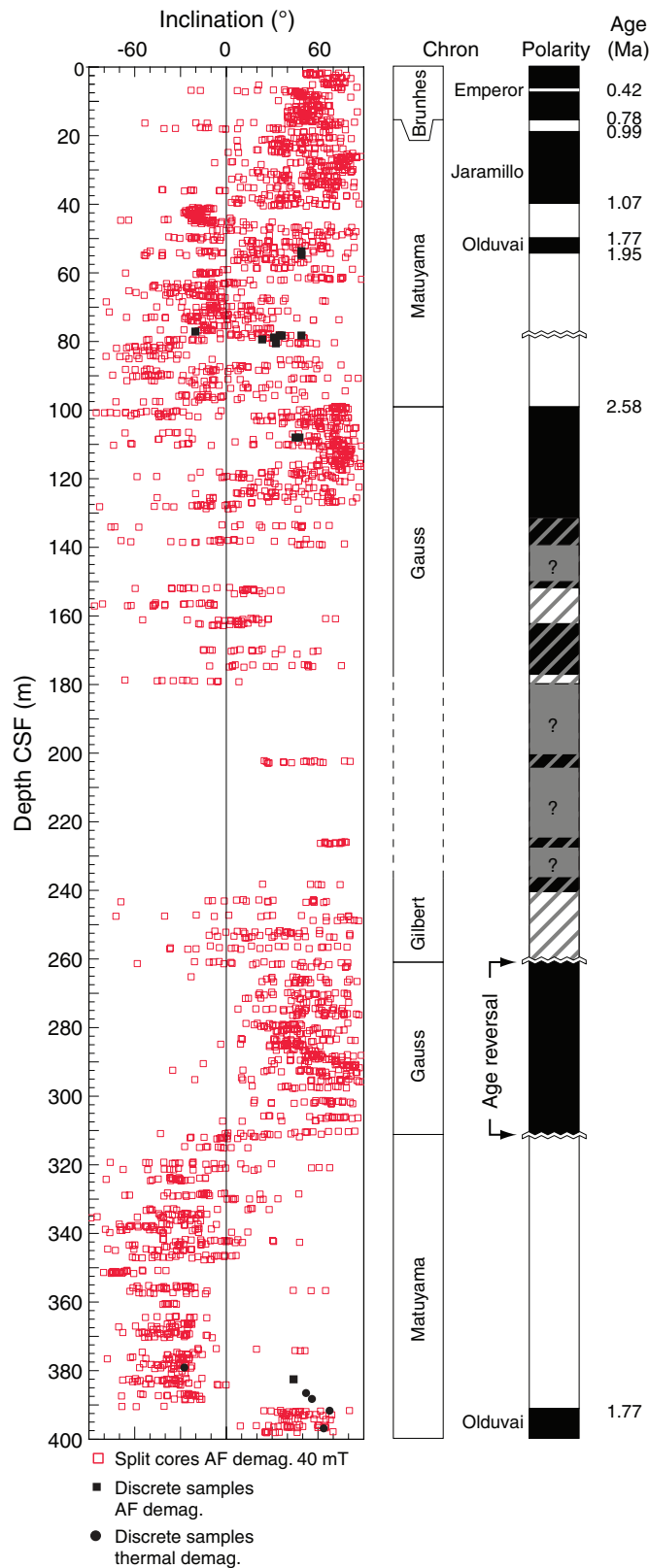




**Figure F37.** Concentrations of (A) salinity, (B) chloride, (C) sodium, and (D) Na/Cl in interstitial water samples, Site C0004. Salinity is calculated from refractive index. CSF = core depth below seafloor. SW = seawater values.

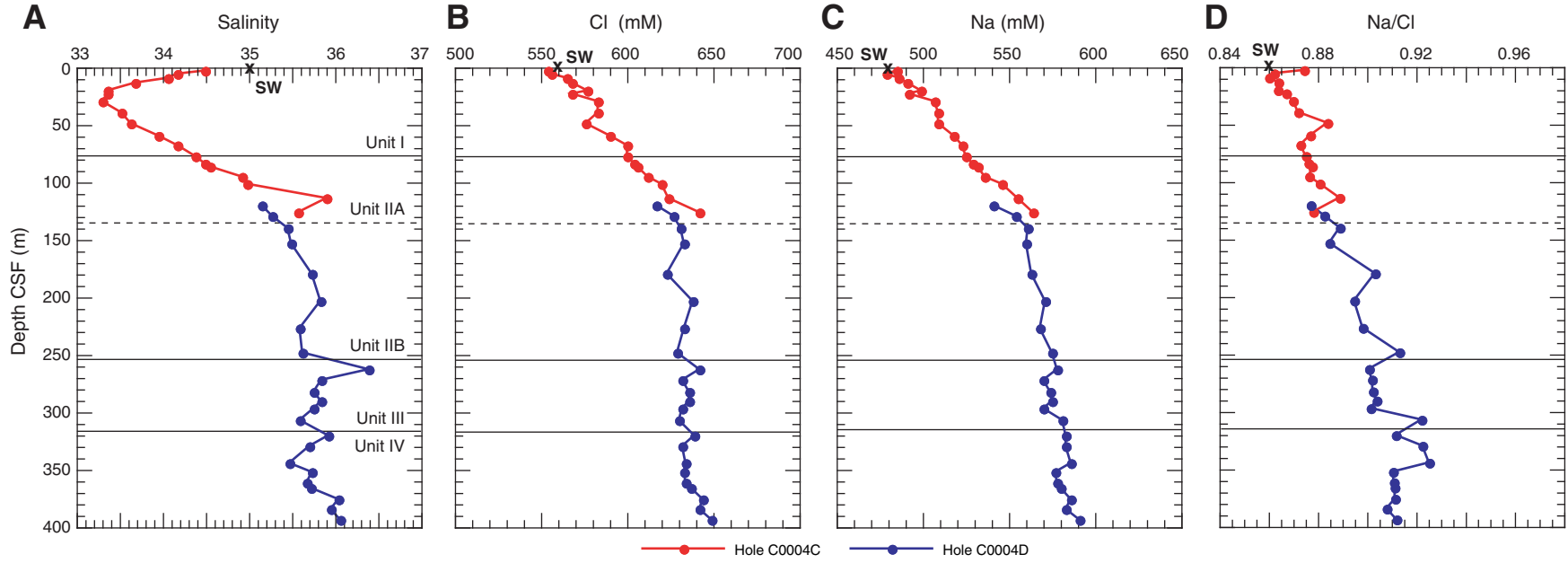




**Figure F38.** Concentrations of (A) sulfate, (B) alkalinity, (C) calcium, (D) magnesium, (E) pH, (F) barium, and (G) sulfate and methane (Hole C0004C only) from interstitial water samples, Site C0004. CSF = core depth below seafloor. SW = seawater values. Plotted Ba data generated on the shipboard ICP-AES.

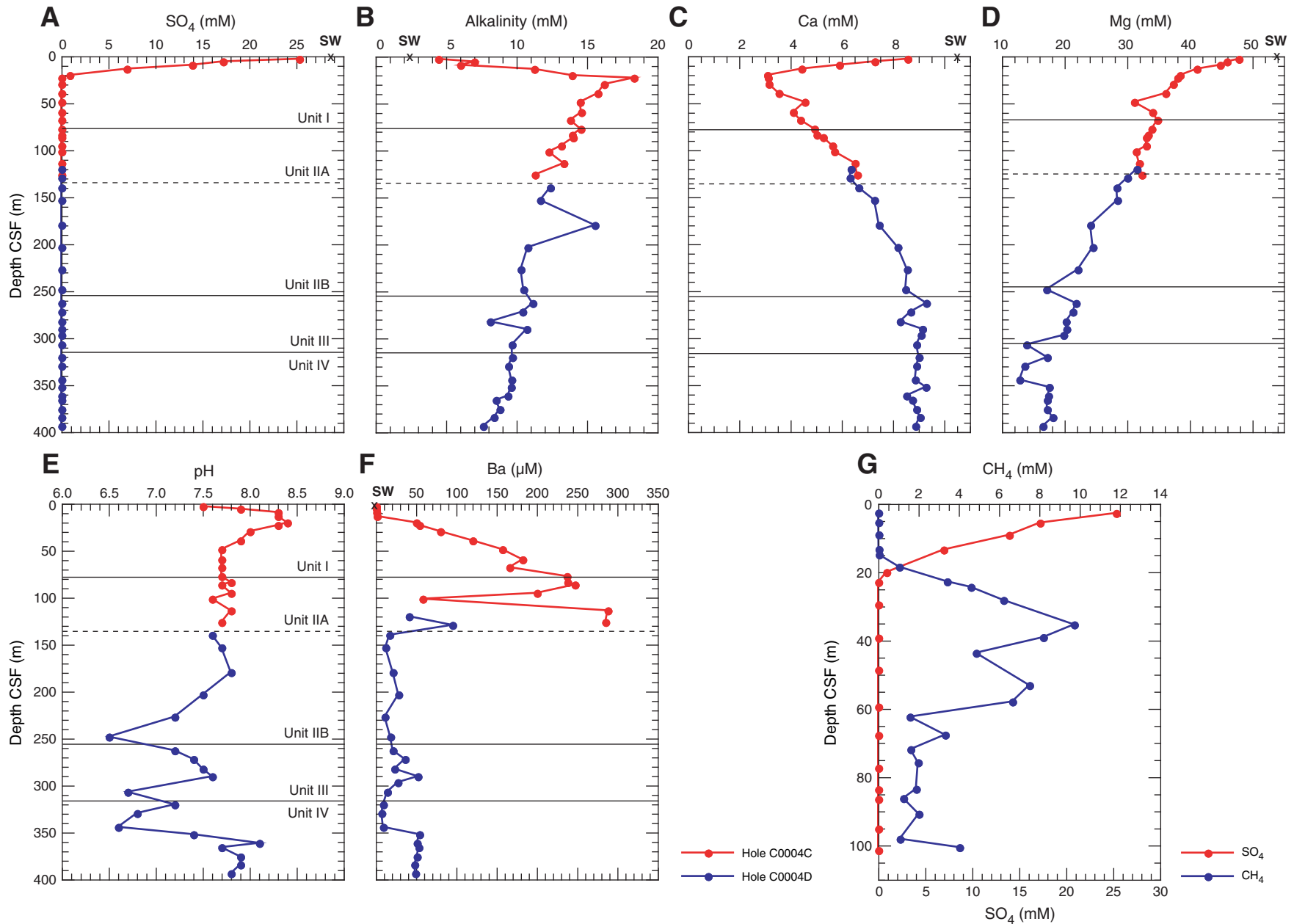




**Figure F39.** Concentrations of (A) ammonium, (B) phosphate, (C) bromide, and (D) manganese from interstitial water samples, Site C0004. CSF = core depth below seafloor. SW = seawater values.

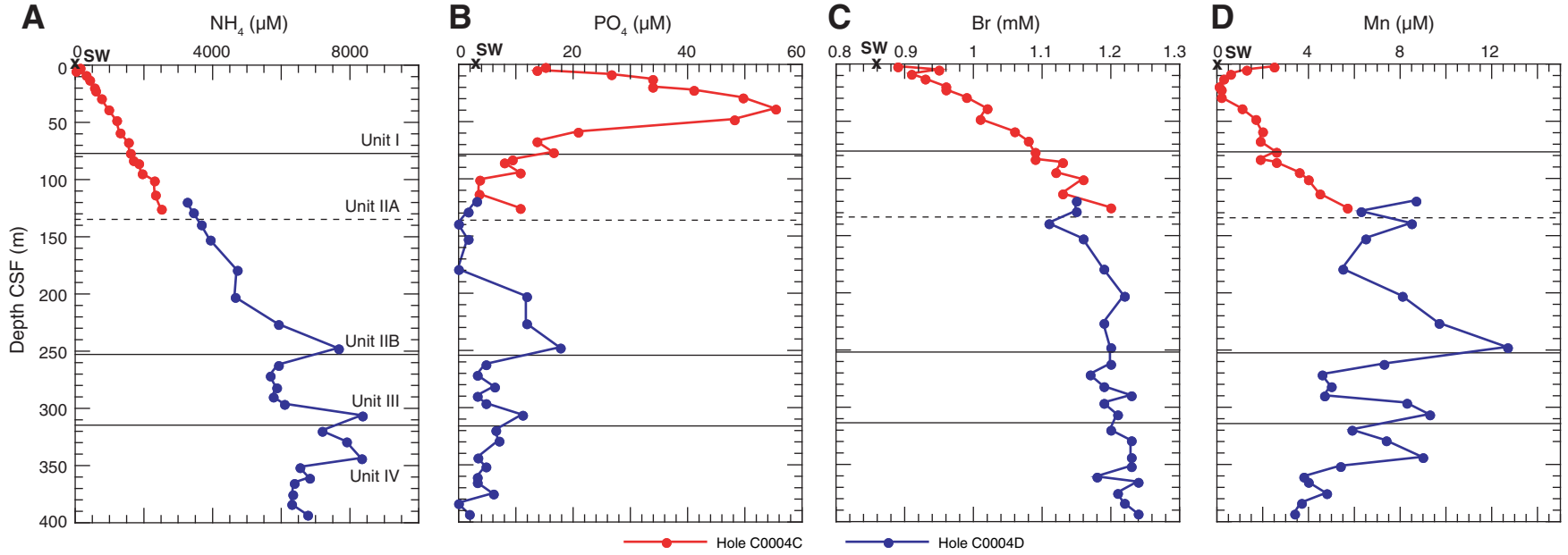




**Figure F40.** Concentrations of (A) lithium, (B) silica, (C) boron, (D) strontium, (E) potassium, (F) rubidium, and (G) cesium in interstitial water samples, Site C0004. CSF = core depth below seafloor. SW = seawater values.

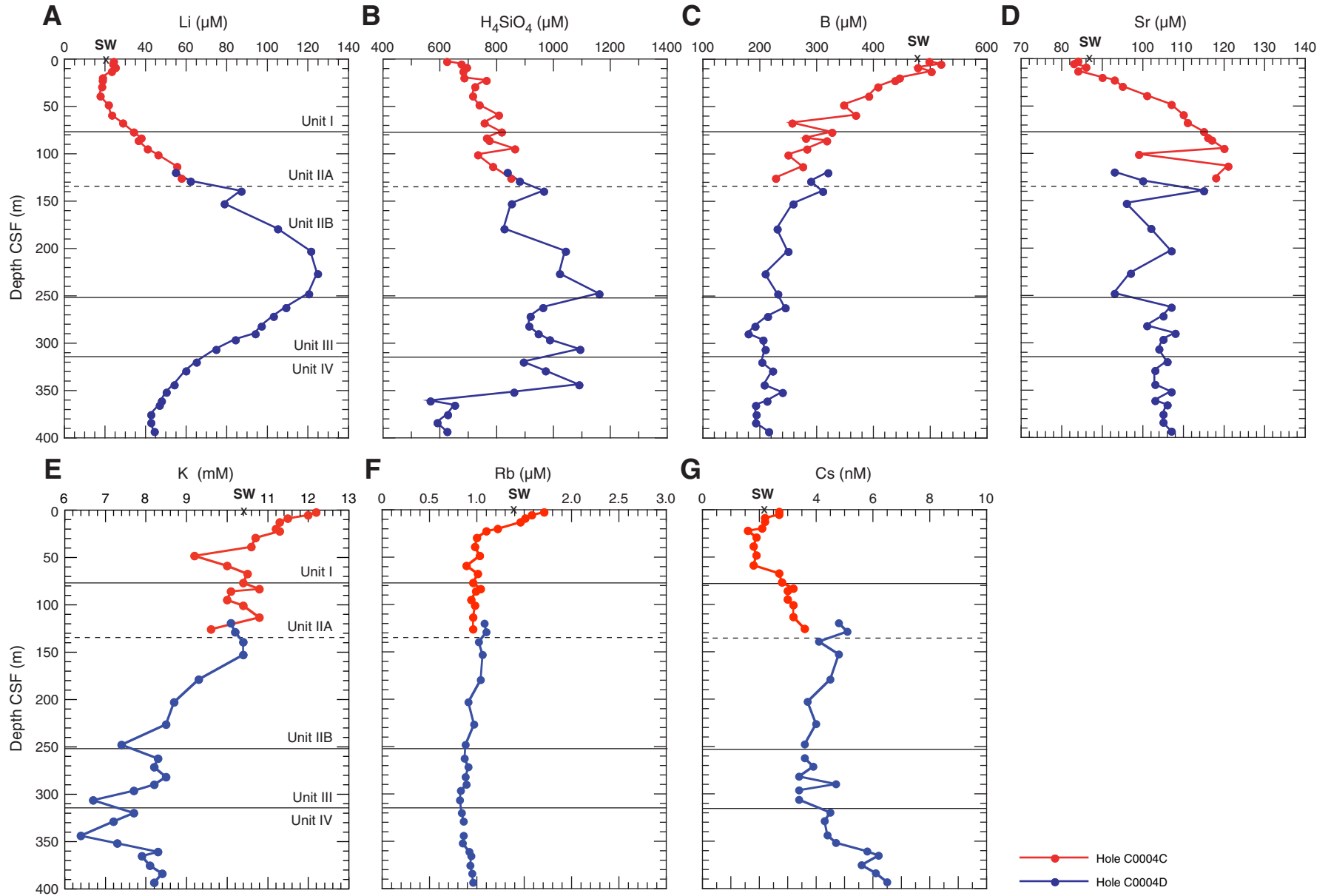




**Figure F41.** Concentrations of (A) iron, (B) copper, (C) zinc, and (D) vanadium from interstitial water samples, Site C0004. CSF = core depth below seafloor. SW = seawater values.

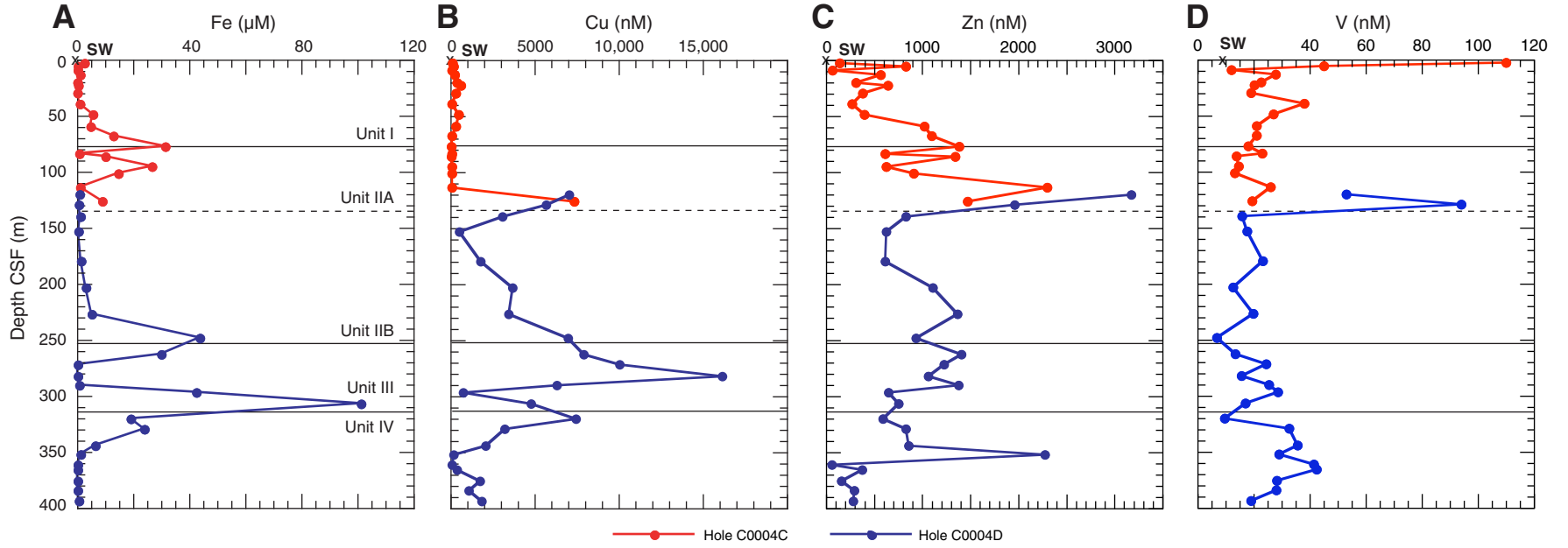




**Figure F42.** Concentrations of (A) molybdenum, (B) lead, (C) uranium, and (D) yttrium from interstitial water samples, Site C0004. CSF = core depth below seafloor. SW = seawater values.

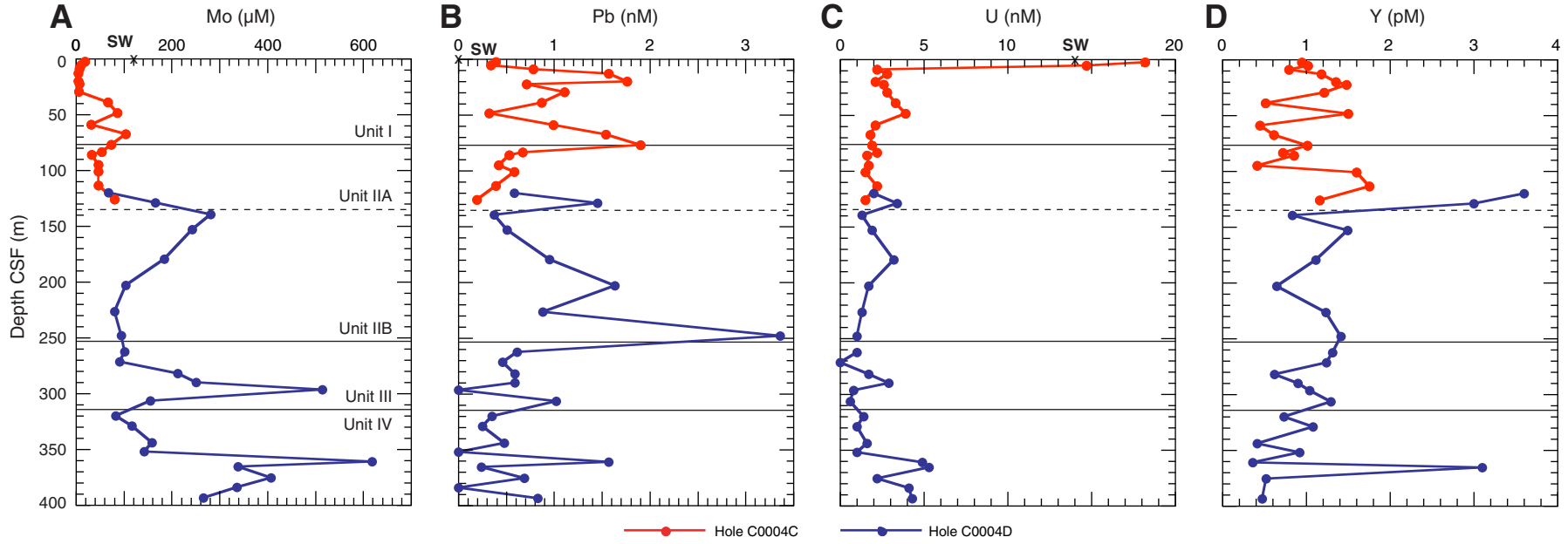


**Figure F43.**  $\delta^{18}\text{O}$  isotope ratios from interstitial water samples, Site C0004. CSF = core depth below seafloor. SW = seawater value.

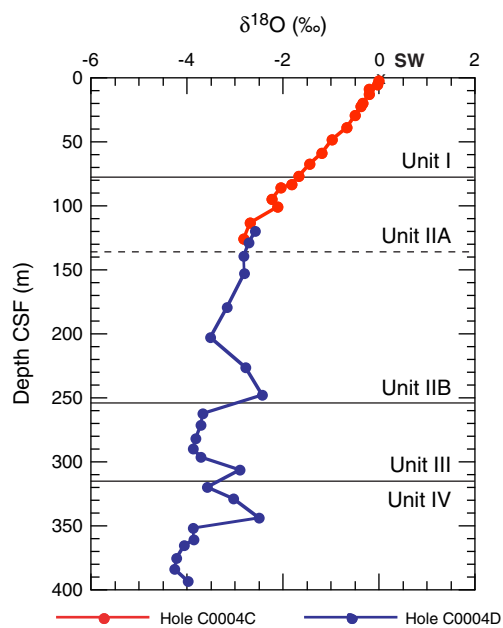


**Figure F44.** Change in alkalinity (corrected for authigenic carbonate precipitation) vs. change in sulfate in uppermost 50 m of Unit I, Site C0004. Blue line = expected values for microbially mediated sulfate reduction-organic matter degradation, red line = expected values for anaerobic oxidation of methane (AOM).

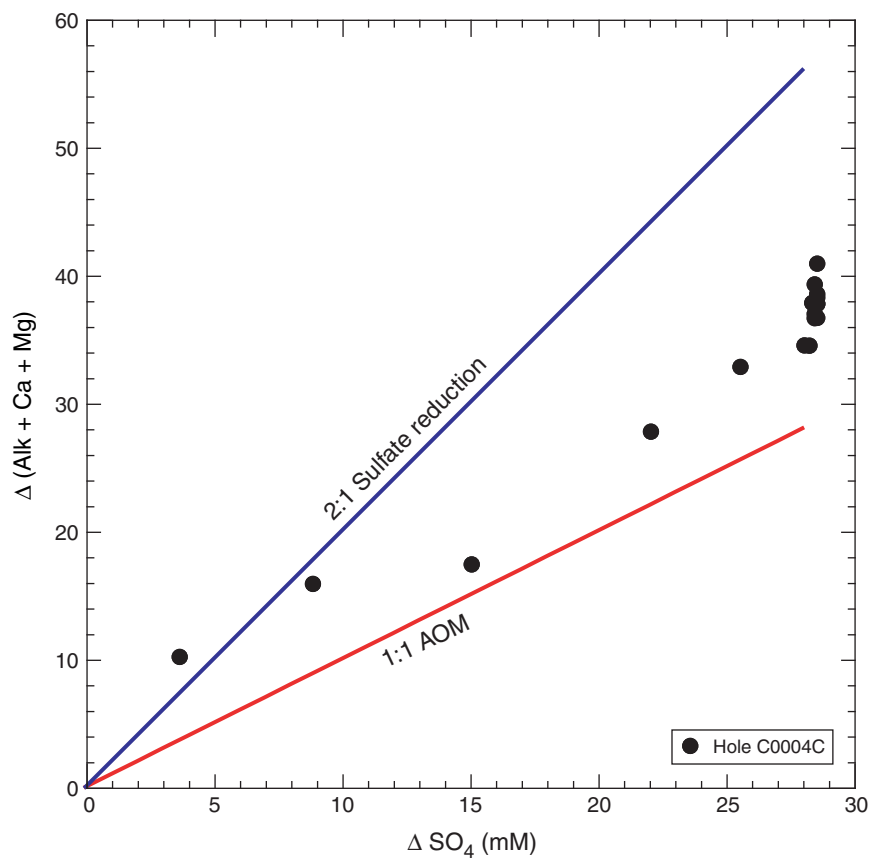


**Figure F45.** Dissolved ethane and methane concentrations calculated from headspace samples (see Table T17), as well as values of  $C_1/C_2$  in sediments, Site C0004. CSF = core depth below seafloor.

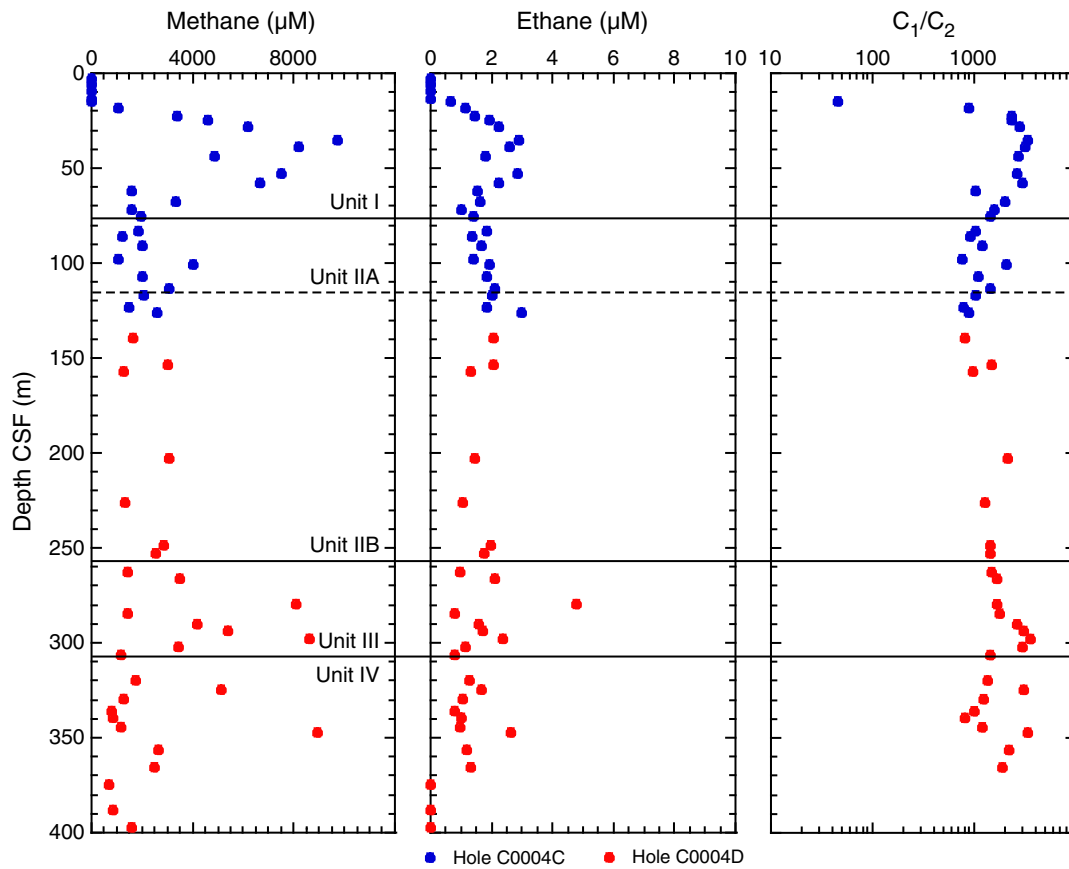




**Figure F46.** Calcium carbonate ( $\text{CaCO}_3$ ), total organic carbon (TOC), total nitrogen (TN), carbon to nitrogen (C/N) ratio, and total sulfur (TS) in sediments, Site C0004. CSF = core depth below seafloor.

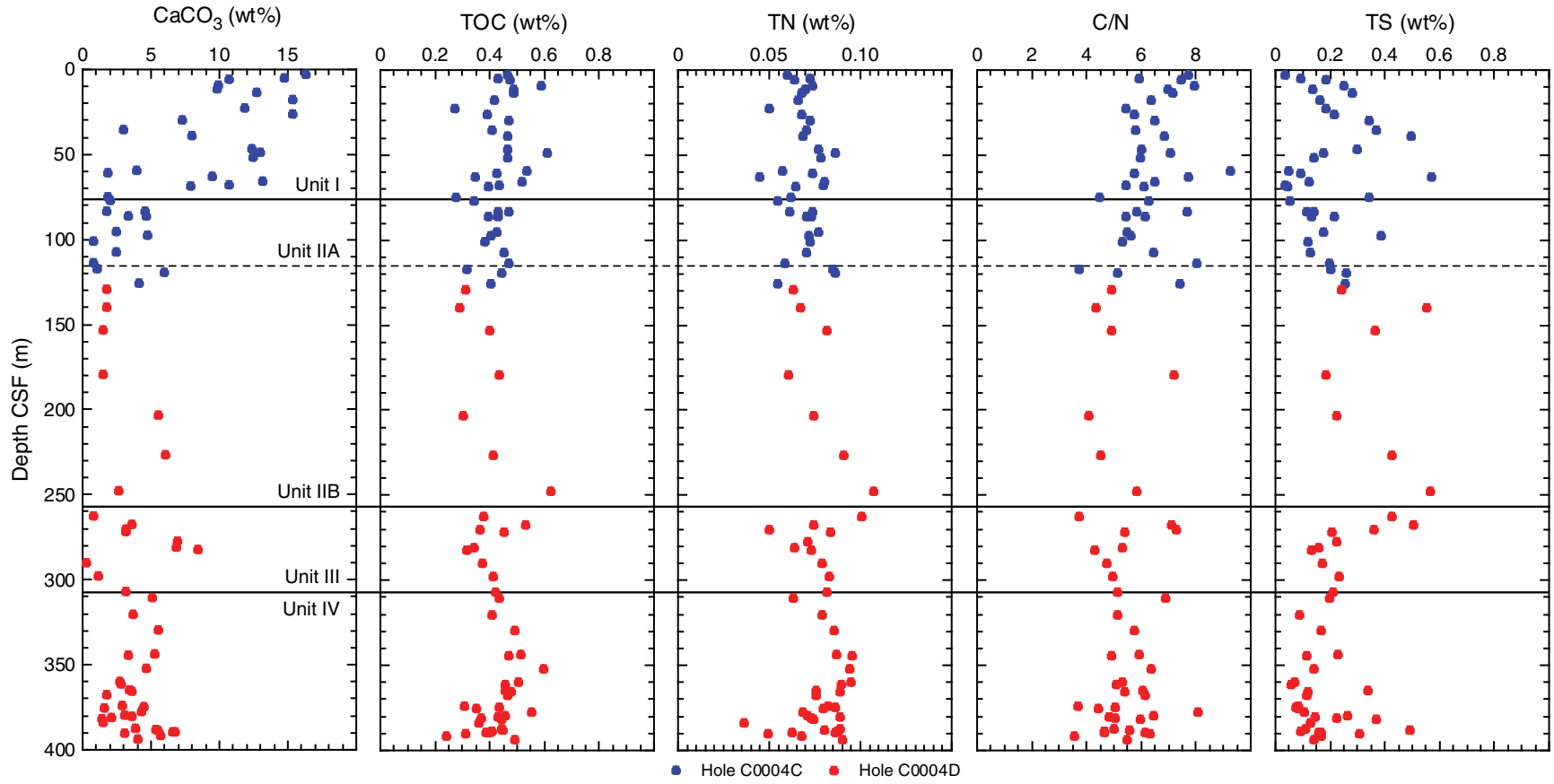


**Figure F47.** Microbial cell abundance enumerated by microscopic direct count of SYBR Green I-stained cells. CSF = core depth below seafloor.

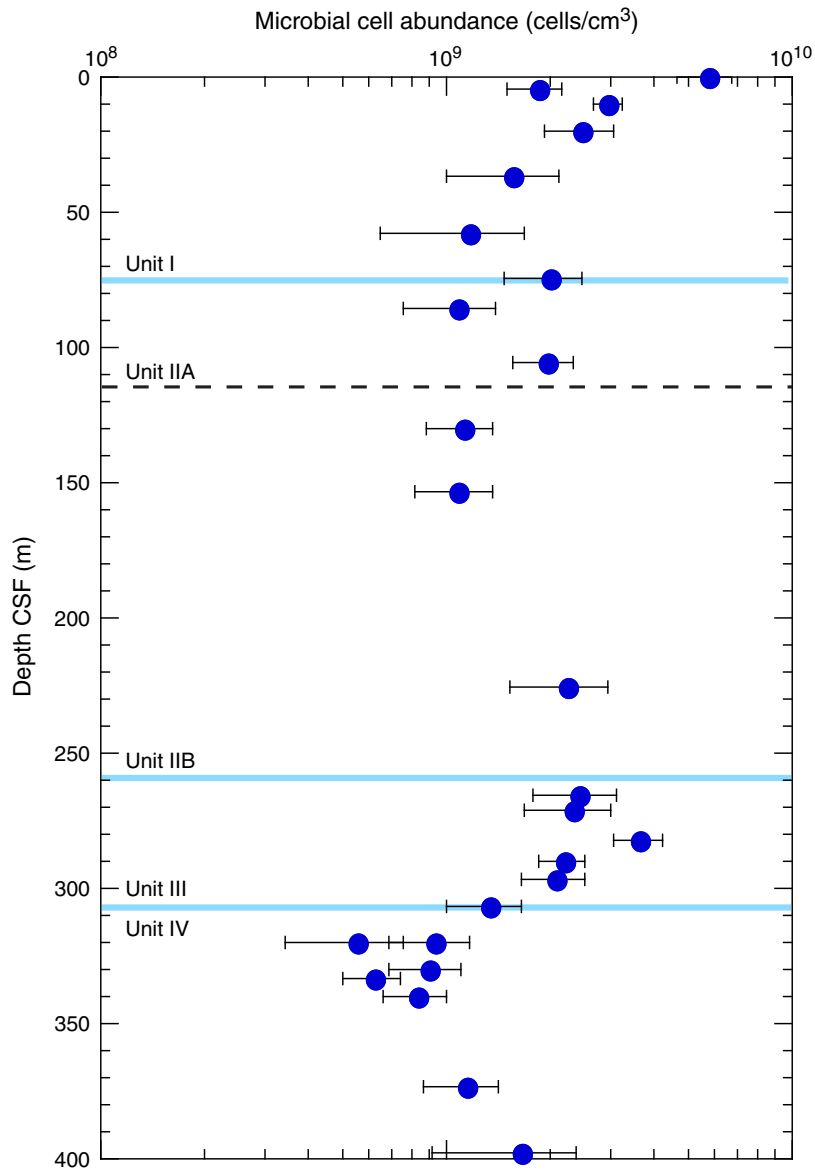


**Figure F48.** Fluorescent microscopic image of SYBR Green I-stained cells detected from sediments from the splay fault zone (Section 316-C0004D-28R-2, 271.1 m CSF).

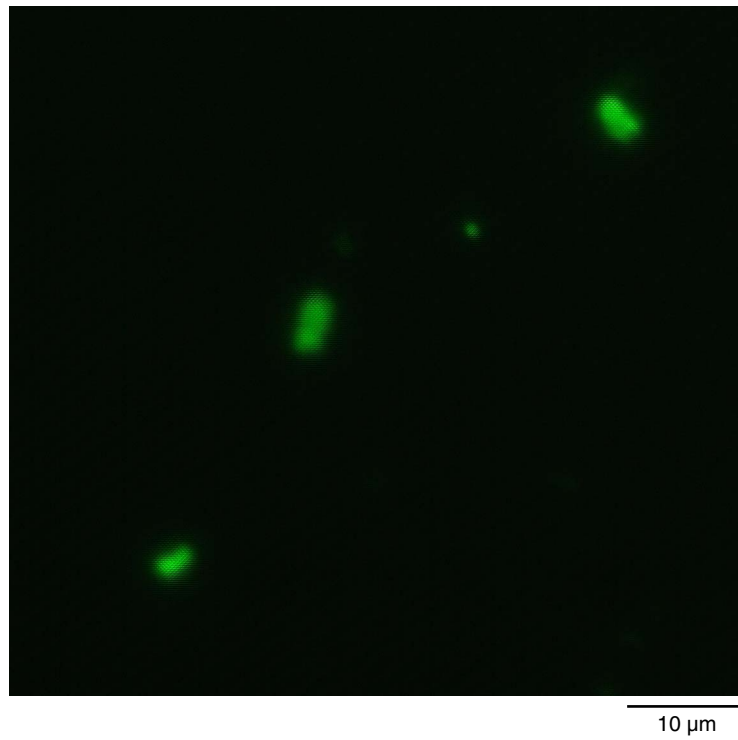


**Figure F49.** Density and porosity measurements, Holes C0004C and C0004D. **A.** Gamma ray attenuation (GRA) density measured using a multisensor core logger (MSCL) system on whole-round core sections (gray dots) and wet bulk density measured on discrete samples using moisture and density (MAD) methods (red dots). **B.** Grain density measured on discrete samples using MAD methods. **C.** MSCL porosity (gray dots) and MAD porosity (red dots). CSF = core depth below seafloor. Orange area = fractured and brecciated interval.

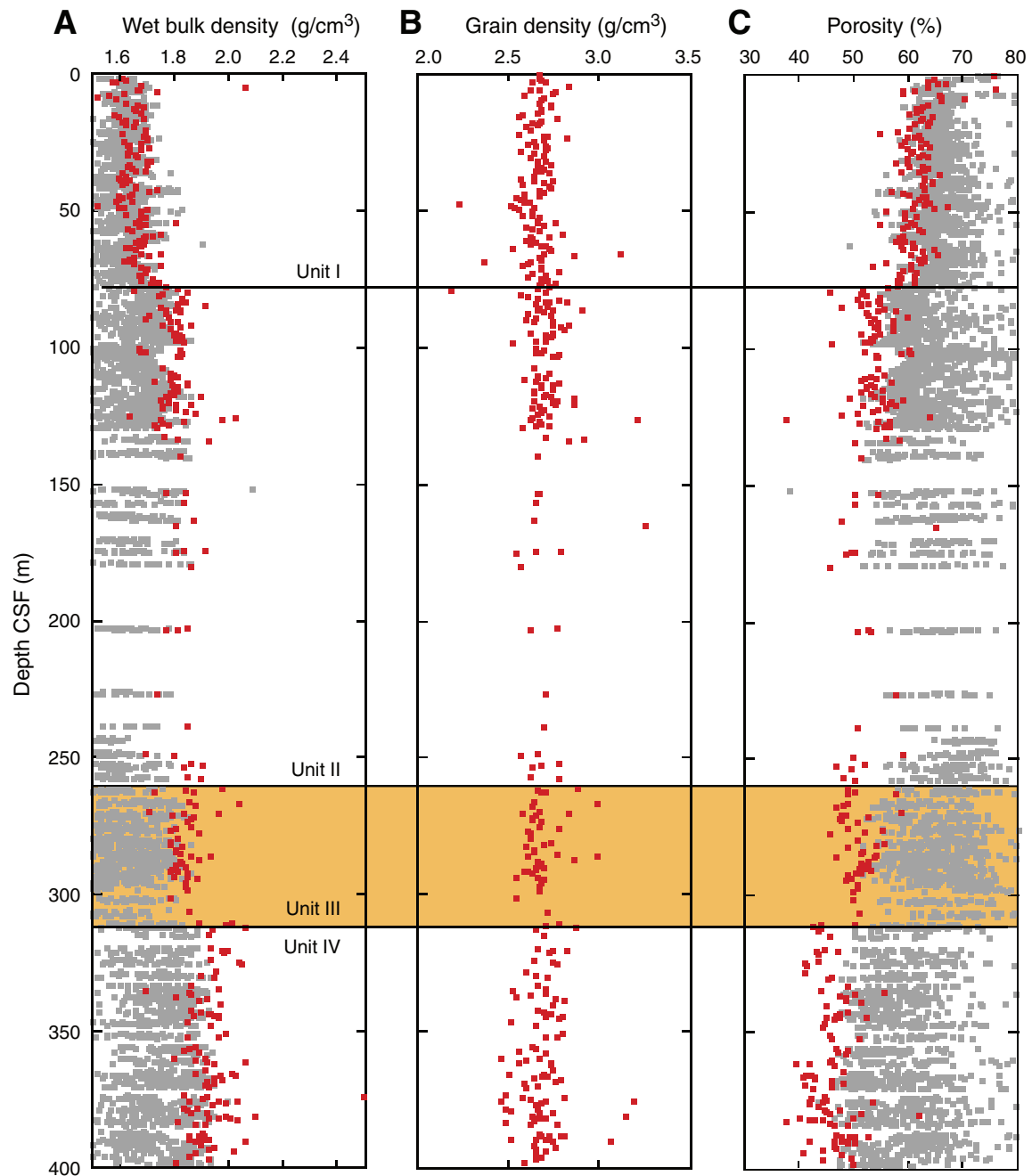




**Figure F50.** Measurements on discrete samples. **A.** *P*-wave velocity. One-sided error bar is associated with partial drying and was estimated experimentally (cf “**Expedition 316 methods**” chapter). **B.** Anisotropy of *P*-wave velocity. Three types of anisotropy are displayed. The in-plane anisotropy (between the two directions perpendicular to the core axis), transverse anisotropy (between core axis and its normal plane), and total anisotropy, calculated from the eigenvalues (7 measurements setup). **C.** Electrical conductivity. **D.** Anisotropy of electrical conductivity. CSF = core depth below seafloor.

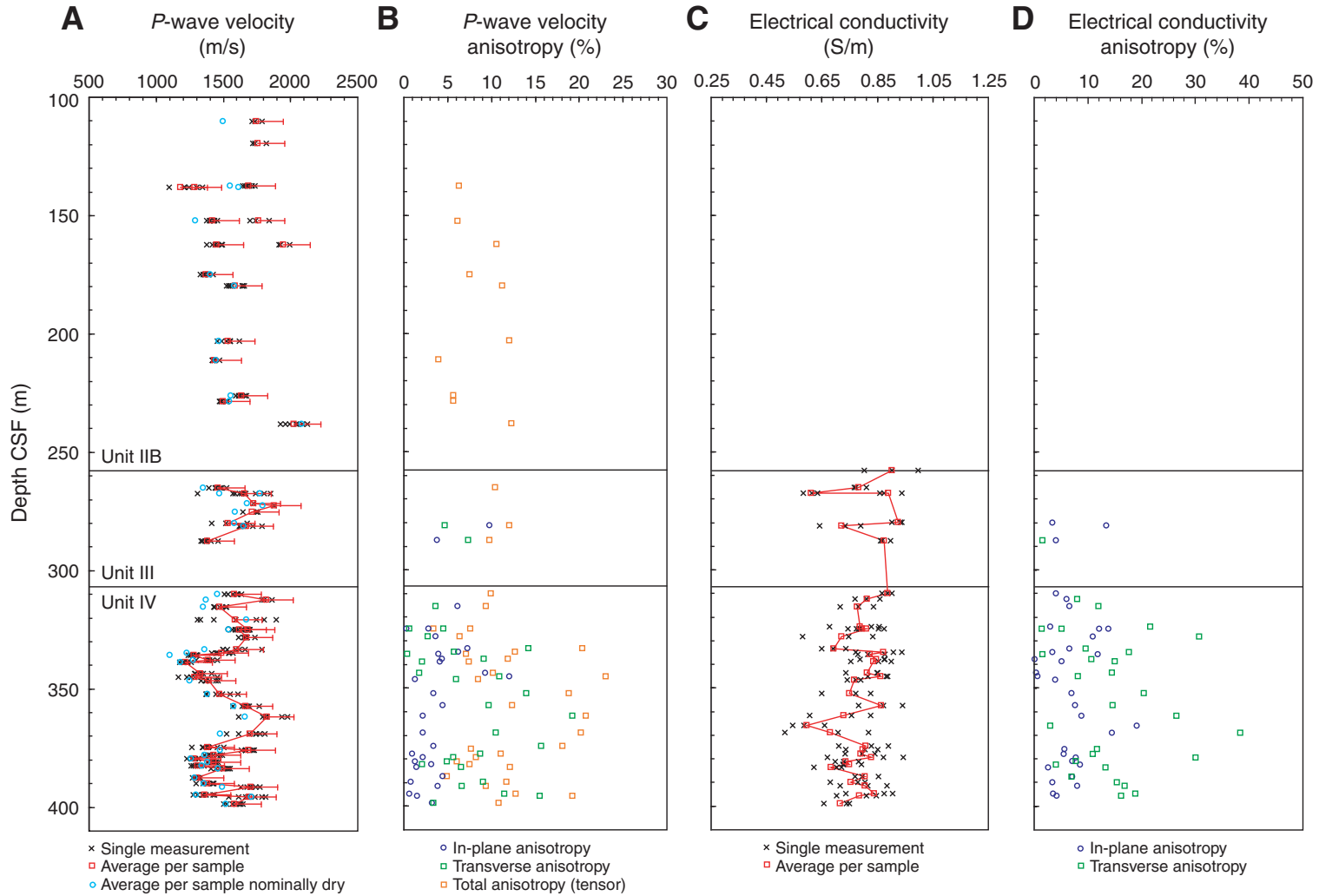


**Figure F51.** Thermal data, Site C0004. **A.** Thermal conductivity. Circles = Unit I, squares = Unit II, diamonds = Unit III, vertical lines = unit averages. **B.** Equilibrium temperatures (circles) and projected temperatures (line). The best-fit linear gradient to the equilibrium temperatures is 52°C/km. **C.** Temperature as a function of thermal resistance. The best-fit slope gives a heat flow value of 55 mW/m<sup>2</sup> and a bottom water temperature of 1.9°C. CSF = core depth below seafloor.

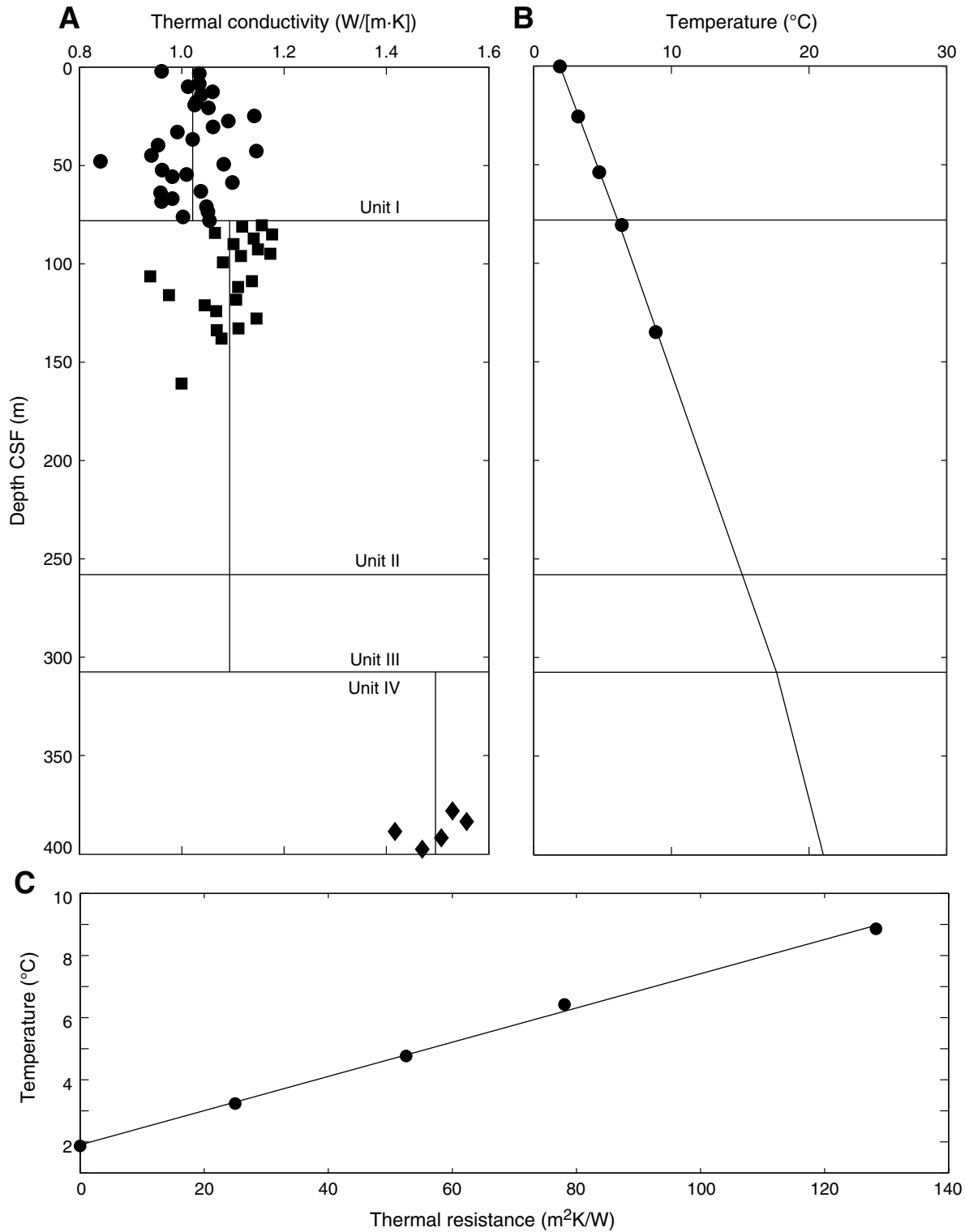


**Figure F52.** Temperature time series measured during the deployment of the APCT3 at Site C0004 (blue line). A. 25.4 m CSF. B. 53.9 m CSF. C. 80.8 m CSF. D. 135.0 m CSF. Unshaded area = data used for equilibrium temperature fit, red line = theoretical equilibrium curve, triangle = beginning of fit, inverted triangle = end of fit, dashed red line with circles = estimate of equilibrium temperature. Note frictional heating at penetration (dashed vertical line) and at pull out.

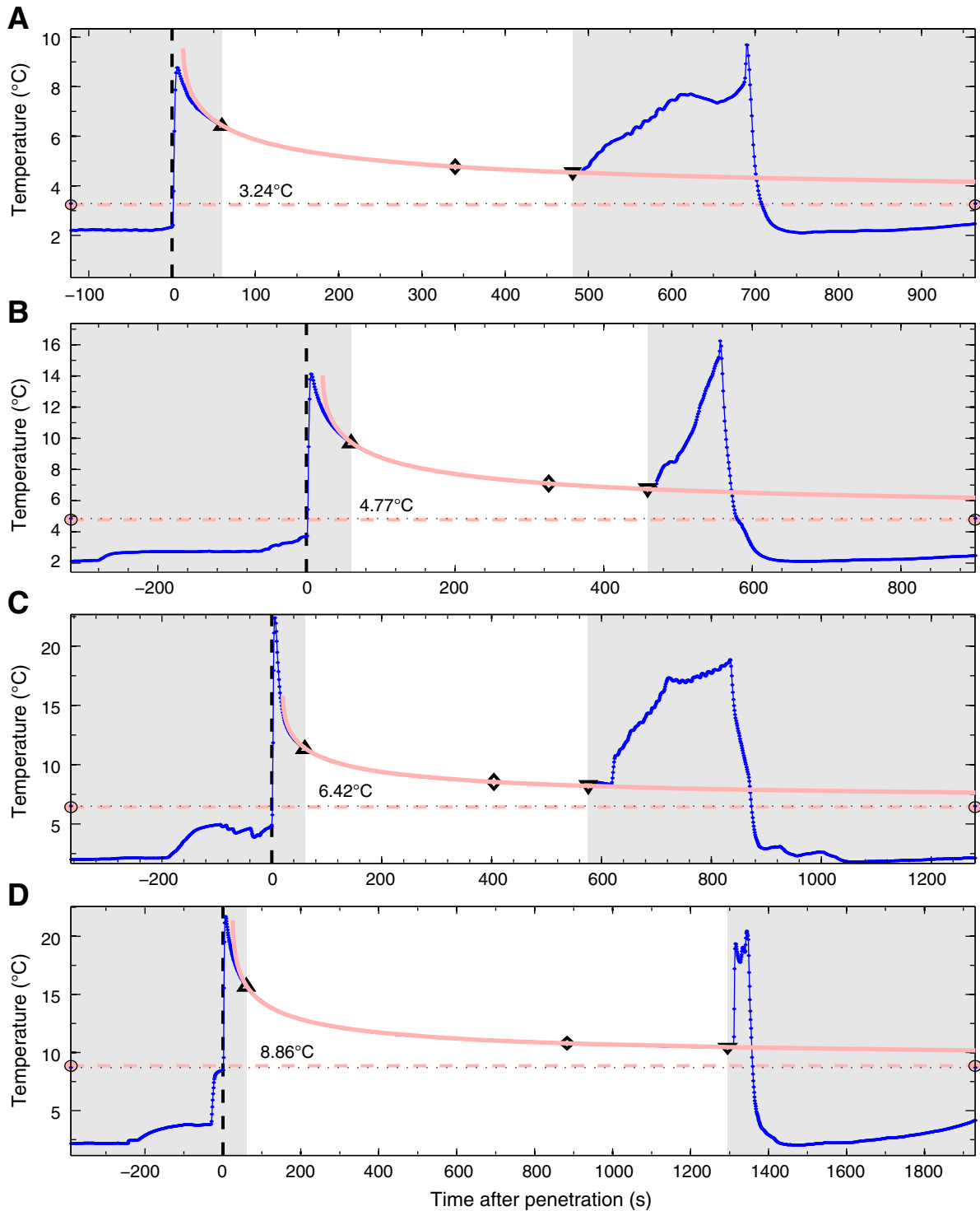


**Figure F53.** Shear strength measurements, Hole C0004C. Shear strength varies over this range of depths with the penetrometer indicating higher values than the semiautomated vane shear apparatus. CSF = core depth below seafloor.

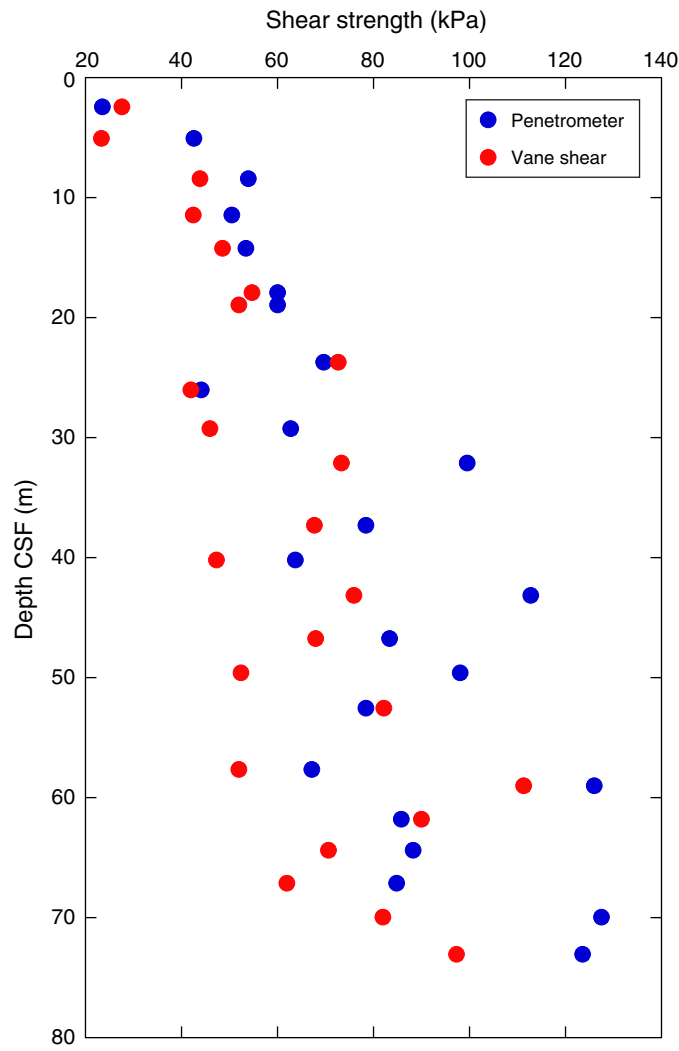


Figure F54.  $L^*$ ,  $a^*$ , and  $b^*$  values, Site C0004. CSF = core depth below seafloor.

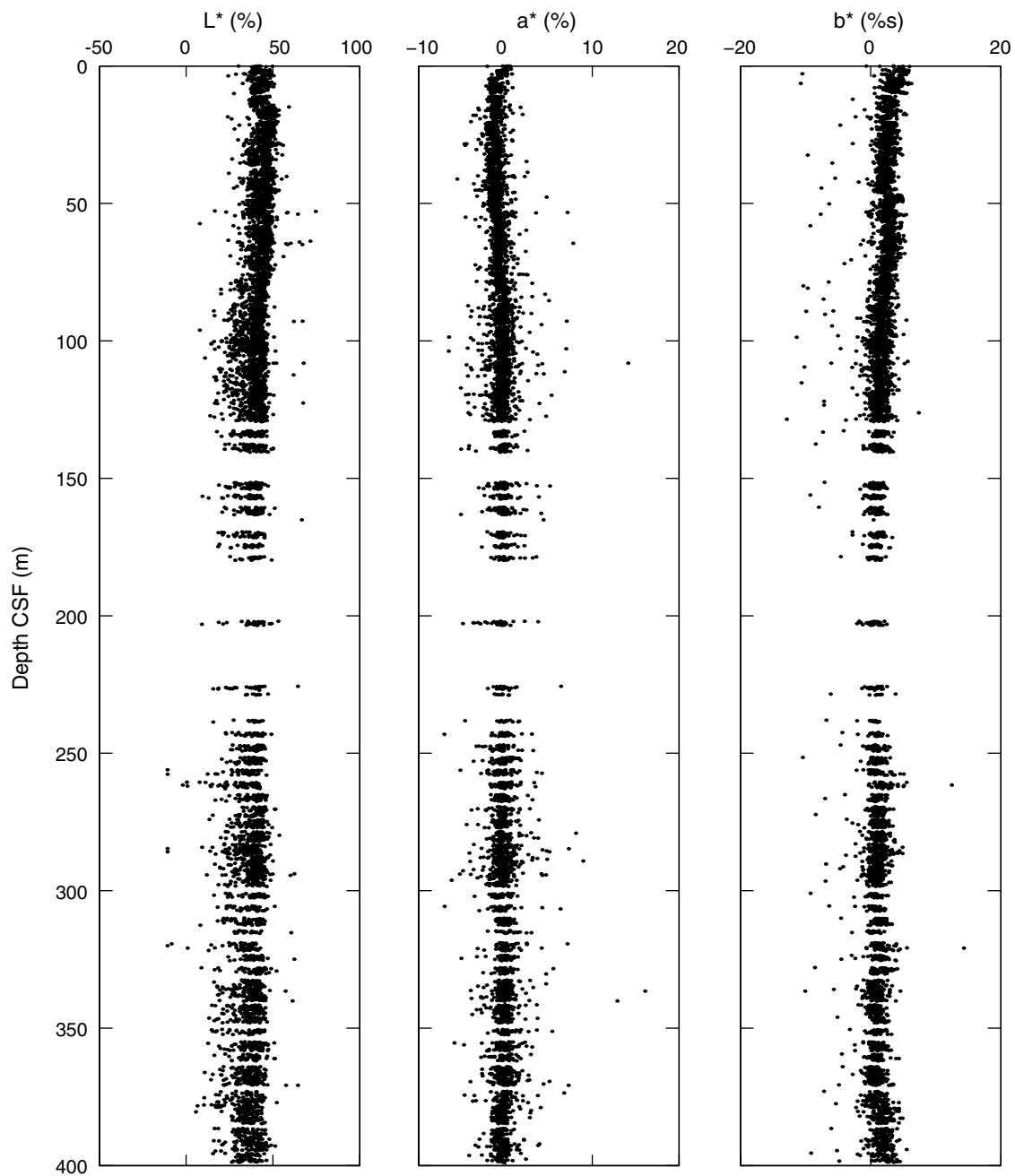
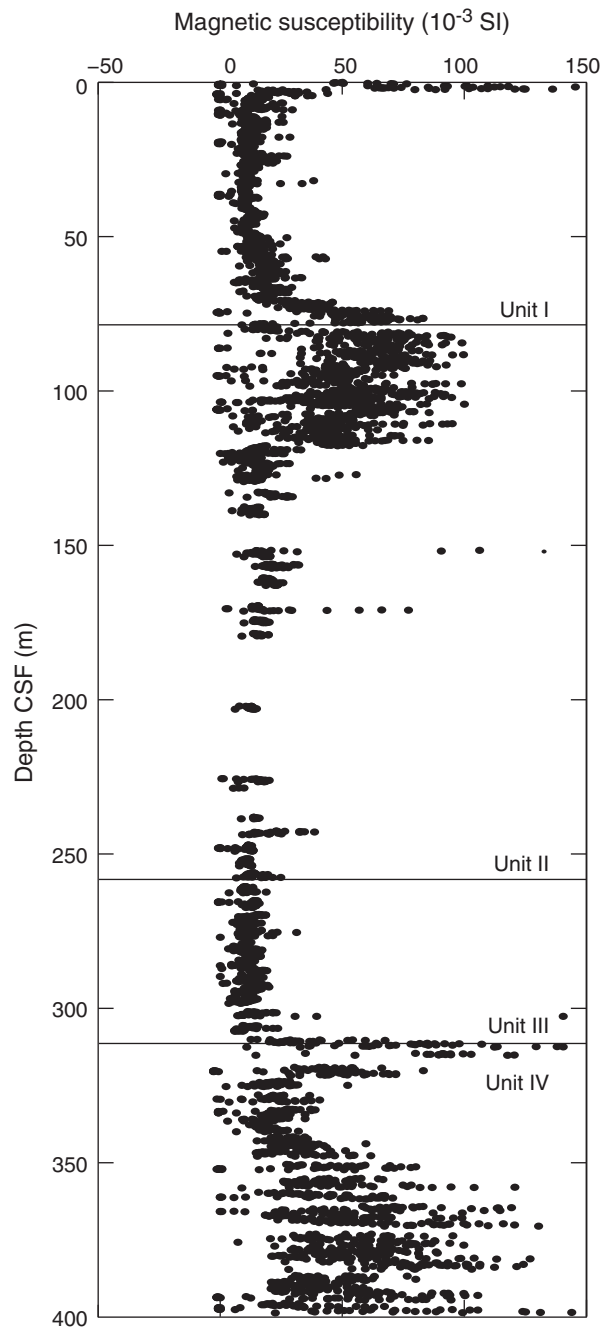
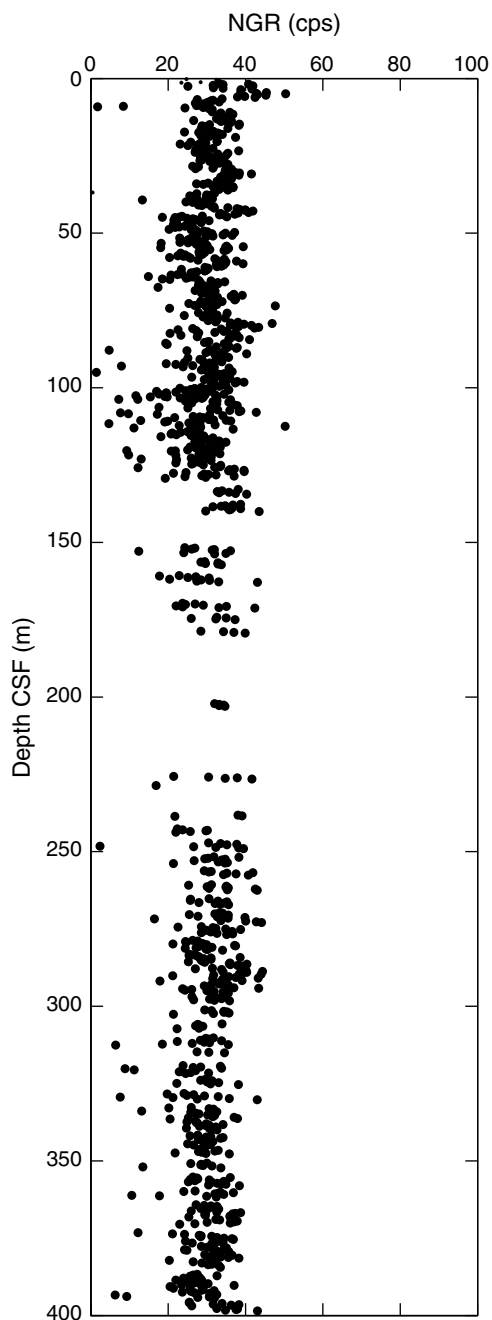


Figure F55. Magnetic susceptibility, Site C0004. CSF = core depth below seafloor.



**Figure F56.** Natural gamma ray (NGR) values with depth, Holes C0004C and C0004D. CSF = core depth below seafloor, cps = counts per second.



**Figure F57.** Correlation between LWD data of Hole C0004B and MSCL-W data of Holes C0004C and C0004D. Numbers below holes are water depth (meters below mean sea level). Correlation positions are given in Table T23. CSF = core depth below seafloor. NGR = natural gamma ray, GR\_RAB = gamma ray by resistivity-at-the-bit tool, sonic = sonic velocity.

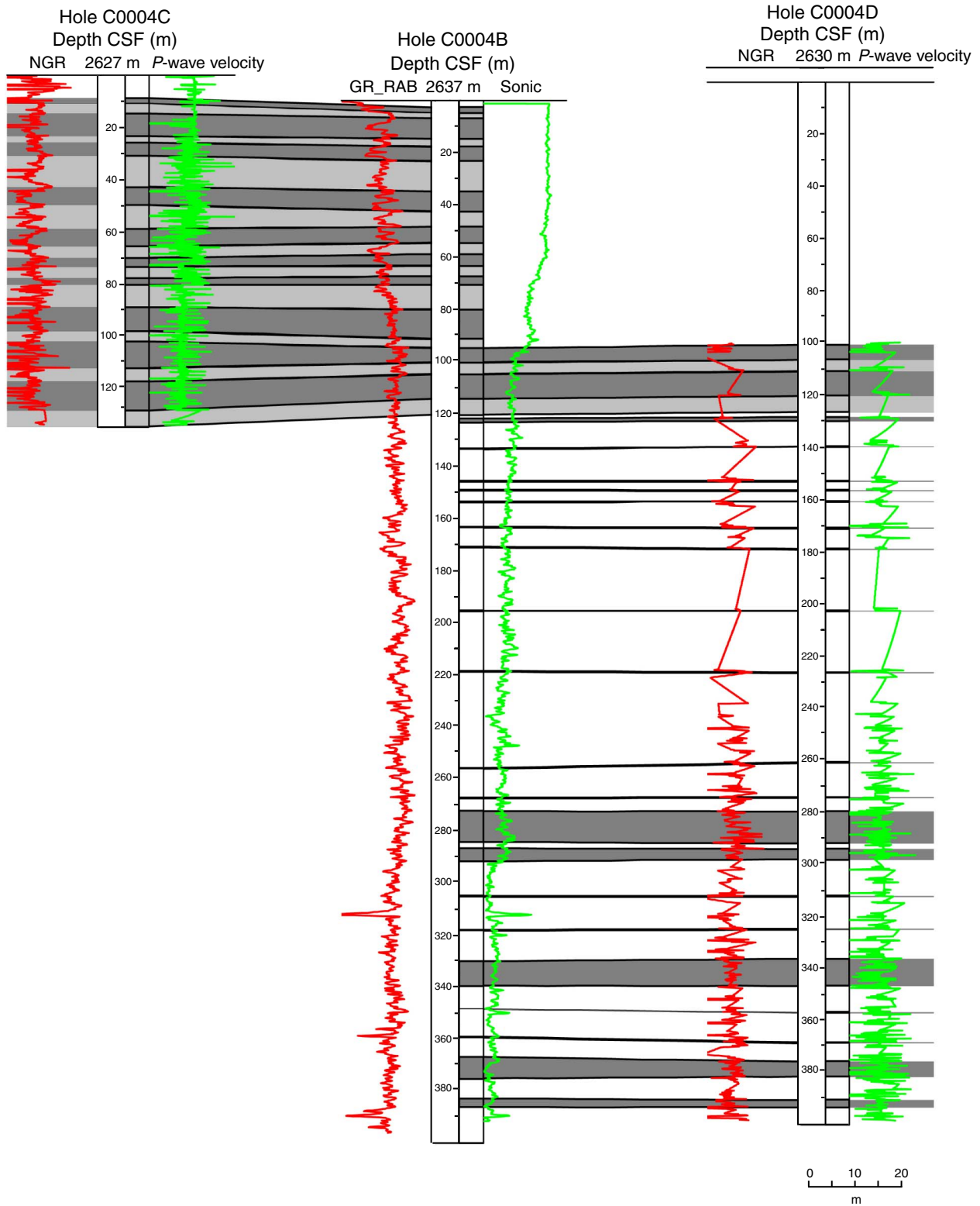


Table T1. Coring summary, Hole C0004C. (See table note.)

Hole C0004C										
Latitude: 33°13.2278'N										
Longitude: 136°43.3312'E										
Seafloor (drillers measurement from rig floor, m): 2655.5										
Distance between rig floor and sea level (m): 28.5										
Water depth (drillers measurement from sea level, m): 2627.0										
Total depth (drillers depth below rig floor, m): 2790.5										
Total penetration (core depth below seafloor, m): 135.0										
Total length of cored section (m): 131.28										
Total core recovered (m): 135.23										
Core recovery (%): 103.01										
Total number of cores: 18										
Core	Date (Dec 2007)	Local time		Depth DRF (m)		Depth CSF (m)		Advanced (m)	Recovered (m)	Recovery (%)
		Shot	On deck	Top	Bottom	Top	Bottom			
316-C0004C-										
1H	20	0541	0557	2655.62	2662.00	0.00	6.38	6.38	6.38	100.00
2H	20	0653	0721	2662.00	2671.50	6.38	15.88	9.50	10.06	105.89
3H	20	0752	0825	2671.50	2681.00	15.88	25.38	9.50	9.57	100.74
4H	20	0859	0918	2681.00	2690.50	25.38	34.88	9.50	9.76	102.74
5H	20	1001	1020	2690.50	2700.00	34.88	44.38	9.50	9.64	101.42
6H	20	1107	1138	2700.00	2709.50	44.38	53.88	9.50	10.16	106.95
7H	20	1220	1304	2709.50	2719.00	53.88	63.38	9.50	10.05	105.79
8H	20	1354	1441	2719.00	2728.50	63.38	72.88	9.50	10.14	106.74
9H	20	1534	1619	2728.50	2736.46	72.88	80.84	7.96	7.96	100.00
10H	20	1743	1808	2736.46	2740.42	80.84	84.80	3.96	3.96	100.00
11H	20	1902	1938	2740.42	2744.84	84.80	89.22	4.42	4.42	100.00
12X	20	2133	2213	2744.84	2754.34	89.22	98.72	9.50	9.60	101.05
13X	20	2334	0016	2754.34	2763.84	98.72	108.22	9.50	9.66	101.68
14X	21	0129	0157	2763.84	2773.34	108.22	117.72	9.50	9.91	104.32
15X	21	0323	0354	2773.34	2782.84	117.72	127.22	9.50	9.90	104.21
16H	21	0419	0447	2782.84	2784.58	127.22	128.96	1.74	1.74	100.00
17H	21	0535	0602	2788.30	2788.80	132.68	133.18	0.50	0.50	100.00
18H	21	0649	0732	2788.80	2790.62	133.18	135.00	1.82	1.82	100.00

Note: DRF = drillers depth below rig floor, CSF = core depth below seafloor.

Table T2. Coring summary, Hole C0004D. (See table note.) (Continued on next page.)

**Hole C0004D**

Latitude: 33°13.2190'N  
 Longitude: 136°43.3287'E  
 Seafloor (drillers measurement from rig floor, m): 2659.0  
 Distance between rig floor and sea level (m): 28.5  
 Water depth (drillers measurement from sea level, m): 2630.5  
 Total depth (drillers depth below rig floor, m): 3059.00  
 Total penetration (core depth below seafloor, m): 400.00  
 Total length of cored section (m): 300.0  
 Total core recovered (m): 130.76  
 Core recovery (%): 43.59  
 Total number of cores: 56

Core	Date (Dec 2007)	Local time		Depth DRF (m)		Depth CSF (m)		Advanced (m)	Recovered (m)	Recovery (%)
		Shot	On deck	Top	Bottom	Top	Bottom			
316-C0004D-										
1R	22	0700	1115	2759.0	2768.5	100.00	109.50	9.50	4.02	42.32
2R	22	1257	1342	2768.5	2778.0	109.50	119.00	9.50	1.52	16.00
3R	22	1449	1526	2778.0	2787.5	119.00	128.50	9.50	1.60	16.84
4R	22	1603	1643	2787.5	2796.5	128.50	137.50	9.00	0.96	10.67
5R	22	1728	1805	2796.5	2806.0	137.50	147.00	9.50	2.91	30.63
6R	22	1825	1910	2806.0	2810.5	147.00	151.50	4.50	0.00	0.00
7R	22	1937	2114	2810.5	2815.0	151.50	156.00	4.50	2.44	54.22
8R	22	2212	2244	2815.0	2819.5	156.00	160.50	4.50	1.51	33.56
9R	22	2319	2359	2819.5	2824.0	160.50	165.00	4.50	2.76	61.33
10R	23	0030	0105	2824.0	2828.5	165.00	169.50	4.50	0.11	2.33
11R	23	0624	0658	2828.5	2833.0	169.50	174.00	4.50	2.20	48.89
12R	23	0725	0800	2833.0	2837.5	174.00	178.50	4.50	1.30	28.89
13R	23	1207	1354	2837.5	2847.0	178.50	188.00	9.50	1.34	14.11
14R	23	1427	1512	2847.0	2856.5	188.00	197.50	9.50	0.00	0.00
15R	23	1555	1636	2856.5	2861.0	197.50	202.00	4.50	0.00	0.00
16R	23	1929	2005	2861.0	2865.5	202.00	206.50	4.50	1.53	34.00
17R	23	2111	2150	2865.5	2875.0	206.50	216.00	9.50	0.00	0.00
18R	23	2230	2307	2875.0	2884.5	216.00	225.50	9.50	0.00	0.00
19R	24	0010	0042	2884.5	2887.5	225.50	228.50	3.00	1.57	52.33
20R	24	0207	0242	2887.5	2897.0	228.50	238.00	9.50	0.38	4.00
21R	24	0357	0425	2897.0	2901.5	238.00	242.50	4.50	0.76	16.89
22R	24	0521	0550	2901.5	2906.0	242.50	247.00	4.50	1.39	30.89
23R	24	0642	0714	2906.0	2910.5	247.00	251.50	4.50	2.30	51.11
24R	24	0748	0810	2910.5	2915.0	251.50	256.00	4.50	2.55	56.67
25R	24	0850	0912	2915.0	2919.5	256.00	260.50	4.50	1.95	43.33
26R	24	0957	1024	2919.5	2924.0	260.50	265.00	4.50	2.41	53.56
27R	24	1108	1140	2924.0	2928.5	265.00	269.50	4.50	2.56	56.89
28R	24	1208	1246	2928.5	2933.0	269.50	274.00	4.50	3.58	79.56
29R	24	1313	1344	2933.0	2937.5	274.00	278.50	4.50	3.26	72.44
30R	24	1406	1442	2937.5	2942.0	278.50	283.00	4.50	3.88	86.22
31R	24	1509	1543	2942.0	2946.5	283.00	287.50	4.50	4.15	92.22
32R	24	1625	1705	2946.5	2951.0	287.50	292.00	4.50	4.45	98.89
33R	24	1728	1805	2951.0	2955.5	292.00	296.50	4.50	4.21	93.56
34R	24	1848	1922	2955.5	2960.0	296.50	301.00	4.50	1.97	43.78
35R	24	1945	2031	2960.0	2964.5	301.00	305.50	4.50	1.64	36.44
36R	25	0407	0433	2964.5	2969.0	305.50	310.00	4.50	2.02	44.78
37R	25	0510	0540	2969.0	2973.5	310.00	314.50	4.50	2.61	58.00
38R	25	0613	0640	2973.5	2978.0	314.50	319.00	4.50	0.97	21.56
39R	25	0700	0722	2978.0	2982.5	319.00	323.50	4.50	2.96	65.78
40R	25	0826	0851	2982.5	2987.0	323.50	328.00	4.50	2.02	44.89
41R	25	0912	0935	2987.0	2991.5	328.00	332.50	4.50	2.62	58.22
42R	25	0953	1011	2991.5	2996.0	332.50	337.00	4.50	4.24	94.22
43R	25	1035	1052	2996.0	3000.5	337.00	341.50	4.50	3.13	69.56
44R	25	1111	1130	3000.5	3005.0	341.50	346.00	4.50	3.90	86.67
45R	25	1150	1224	3005.0	3009.5	346.00	350.50	4.50	2.08	46.22
46R	25	1250	1324	3009.5	3014.0	350.50	355.00	4.50	1.97	43.78
47R	25	1349	1422	3014.0	3018.5	355.00	359.50	4.50	3.34	74.22
48R	25	1449	1540	3018.5	3023.0	359.50	364.00	4.50	2.43	54.00
49R	25	1610	1644	3023.0	3027.5	364.00	368.50	4.50	4.45	98.89
50R	25	1708	1746	3027.5	3032.0	368.50	373.00	4.50	2.29	50.89
51R	25	1807	1839	3032.0	3036.5	373.00	377.50	4.50	4.12	91.56
52R	25	1900	1933	3036.5	3041.0	377.50	382.00	4.50	4.17	92.67
53R	25	1958	2031	3041.0	3045.5	382.00	386.50	4.50	2.71	60.22
54R	25	2059	2132	3045.5	3050.0	386.50	391.00	4.50	4.51	100.22

Table T2 (continued).

Core	Date (Dec 2007)	Local time		Depth DRF (m)		Depth CSF (m)		Advanced (m)	Recovered (m)	Recovery (%)
		Shot	On deck	Top	Bottom	Top	Bottom			
55R	25	2159	2233	3050.0	3054.5	391.00	395.50	4.50	3.76	83.56
56R	25	2300	2334	3054.5	3059.0	395.50	400.00	4.50	3.26	72.44

Note: DRF = drillers depth below rig floor, CSF = core depth below seafloor.

Table T3. Summary of lithologic units, Holes C0004C and C0004D. (See table note.)

Unit	Core, section, interval (cm)		Depth CSF (m)		Thickness (m)	Stratigraphic age	Lithologic description	Processes of formation
	Top	Bottom	Top	Bottom				
I	316-C0004C- 1H-1, 0	316-C0004C- 9H-5, 70	0.00	78.06	78.06	Quaternary	Nannofossil-rich mud with rare volcanic ash layers and rare very thin sand layers	Hemipelagic settling, rare volcanic ash falls, and very thin bedded turbidites
IIA	9H-5, 70	15X-1, 0	78.06	117.72	39.66	Pliocene	Sedimentary breccias, mud	Mass flow breccias redeposited on the slope with hemipelagic settling
IIB	316-C0004D- 1R-1, 0	316-C0004D- 25R-CC, 0.29	100.00	258.01	158.01	Pliocene	Mud with rare turbidite sand layers and volcanic ash layers	Hemipelagic settling with rare volcanic ash layers
III	25R-CC, 0.29	36R-CC, 0.05	258.01	307.52	49.51	Pliocene (younger than Subunit IIB)	Mud with scattered volcanic ash layers	Hemipelagic settling with some volcanic ash layers
IV	36R-CC, 0.05	56R-CC, 0.15	307.52	398.79	91.27	Quaternary	Mud with turbidite sand layers and rare volcanic layers	Hemipelagic settling with thin-bedded turbidites and rare volcanic ash falls

Note: CSF = core depth below seafloor.



Table T4. XRD data, Holes C0004C and C0004D. (See table notes.) (Continued on next two pages.)

Unit	Core, section, interval (cm)	Core type	Depth CSF (m)	Peak intensity (counts/step)				Integrated peak area (total counts)				Abundance calculated from SVD normalization factor										
				Clay	Quartz	Plagioclase	Calcite	Clay	Quartz	Plagioclase	Calcite	Calculated abundance (wt%)				Normalized abundance (wt%)						
												Clay	Quartz	Plagioclase	Calcite	Corrected calcite	Absolute total	Clay	Quartz	Plagioclase	Calcite	Relative total
316-C0004C-																						
I	1H-2, 119–120.5	WR	2.61	44	825	186	552	2,429	26,968	11,302	18,471	31.8	15.0	13.4	21.1	21.1	81.4	39.0	18.5	16.5	25.9	100
	1H-5, 92.5–94	WR	5.17	58	1,106	191	464	3,055	33,021	11,448	16,426	37.7	18.5	13.2	17.8	17.8	87.1	43.3	21.2	15.1	20.4	100
	1H-5, 117–118.5	WR	5.41	75	1,207	204	393	3,047	37,062	13,496	12,231	38.7	20.8	15.8	12.1	12.1	87.4	44.3	23.8	18.1	13.8	100
	2H-4, 0–1.5	W	9.20	66	961	183	321	3,221	31,868	13,714	11,556	40.8	17.7	16.3	11.2	11.2	86.1	47.5	20.5	19.0	13.1	100
	2H-5, 35–36.5	WR	10.98	77	1,023	195	328	3,617	33,153	13,685	11,891	44.7	18.4	16.1	11.3	11.3	90.5	49.4	20.3	17.8	12.5	100
	2H-6, 119.5–121	W	13.26	65	996	170	386	3,087	33,756	12,434	13,609	38.6	18.9	14.5	14.0	14.0	85.9	44.9	21.9	16.9	16.3	100
	3H-2, 25–26.5	WR	17.54	73	793	349	476	3,194	28,619	13,754	16,054	40.9	15.8	16.5	17.2	17.2	90.5	45.3	17.4	18.3	19.1	100
	3H-8, 20–21.5	WR	22.96	72	1,048	214	355	3,375	34,005	12,699	13,662	41.6	19.0	14.8	13.9	13.9	89.2	46.7	21.3	16.6	15.5	100
	4H-1, 58.5–60	WR	25.97	59	830	181	525	3,125	27,049	11,330	18,024	38.7	15.0	13.3	20.0	20.0	86.9	44.5	17.2	15.3	23.0	100
	4H-4, 20–21.5	WR	29.61	87	1,061	223	216	3,629	34,081	13,702	7,861	44.6	18.9	16.1	6.0	6.0	85.6	52.1	22.1	18.8	7.1	100
	5H-1, 63–64.5	WR	35.51	74	1,122	248	103	4,073	39,734	13,522	3,303	48.4	22.1	15.5	-0.4	0.0	86.0	56.3	25.7	18.0	0.0	100
	5H-4, 0–1.5	WR	39.07	62	1,095	196	254	3,723	32,913	12,576	7,999	44.8	18.2	14.6	6.2	6.2	83.8	53.4	21.8	17.4	7.4	100
	6H-2, 63.5–65	WR	46.44	67	913	152	425	3,397	29,495	10,198	15,035	40.3	16.4	11.5	15.9	15.9	84.1	47.9	19.5	13.7	18.9	100
	6H-4, 0–1.5	WR	48.48	78	994	193	379	3,495	31,294	11,742	14,565	42.3	17.4	13.5	15.1	15.1	88.3	47.9	19.7	15.3	17.1	100
	6H-7, 15–16.5	WR	51.76	88	863	169	424	4,066	28,666	10,609	14,746	47.2	15.8	11.9	15.0	15.0	90.0	52.5	17.6	13.3	16.7	100
	7H-6, 0–1.5	WR	59.34	74	970	194	100	4,484	35,229	12,939	2,733	52.2	19.5	14.8	-1.3	0.0	86.5	60.4	22.5	17.1	0.0	100
	7H-7, 129–130.5	WR	60.85	87	1,084	189	86	4,124	33,566	13,420	2,396	49.1	18.5	15.6	-1.4	0.0	83.2	59.0	22.2	18.8	0.0	100
	7H-9, 15–16.5	WR	62.52	66	718	183	308	3,645	24,829	11,422	8,781	43.6	13.6	13.4	7.6	7.6	78.1	55.8	17.3	17.1	9.7	100
	8H-2, 68–69.5	WR	65.46	61	975	207	437	3,162	31,190	11,540	13,992	38.8	17.4	13.4	14.6	14.6	84.1	46.1	20.7	15.9	17.3	100
	8H-4, 0–1.5	WR	67.63	59	735	224	402	2,778	26,714	13,776	12,644	36.8	14.7	16.8	13.1	13.1	81.4	45.2	18.1	20.6	16.2	100
	8H-5, 91–92.5	WR	68.76	54	744	228	260	2,753	25,361	14,552	9,006	37.0	13.9	17.9	8.4	8.4	77.2	47.9	18.0	23.2	10.9	100
	9H-2, 68–69.5	WR	74.97	63	953	249	82	3,618	31,981	17,562	2,374	47.2	17.5	21.5	-1.2	0.0	86.2	54.8	20.3	25.0	0.0	100
	9H-4, 0–1.5	WR	77.14	59	846	214	87	3,237	29,835	15,242	3,232	41.9	16.4	18.5	0.4	0.4	77.1	54.3	21.2	24.0	0.5	100
	9H-5, 57–58	W	77.93	84	1,183	200	32	4,959	35,450	14,336	1,294	57.9	19.4	16.5	-3.6	0.0	93.9	61.7	20.7	17.6	0.0	100
	9H-5, 58–60	A	77.94	57	1,007	199	125	3,459	31,486	14,741	5,562	43.7	17.3	17.7	3.2	3.2	82.0	53.3	21.2	21.6	3.9	100
	9H-5, 60–62	A	77.96	67	942	212	127	2,951	30,941	14,270	5,807	38.4	17.1	17.2	3.9	3.9	76.7	50.1	22.3	22.5	5.1	100
	9H-5, 62–64	A	77.98	84	1,047	170	157	3,584	32,800	14,307	5,985	44.6	18.1	17.0	3.6	3.6	83.3	53.5	21.7	20.4	4.4	100
	9H-5, 64–66	A	78.00	90	988	252	148	3,886	33,465	15,548	5,667	48.4	18.4	18.6	2.9	2.9	88.4	54.8	20.8	21.0	3.3	100
	9H-5, 66–68	A	78.02	62	962	186	163	4,047	32,349	14,625	5,036	49.4	17.8	17.3	2.1	2.1	86.5	57.1	20.5	20.0	2.4	100
	9H-5, 68–70	A	78.04	76	967	222	162	3,654	32,919	15,262	5,133	45.9	18.1	18.3	2.4	2.4	84.8	54.2	21.4	21.6	2.9	100
	9H-5, 70–71	A	78.06	90	1,025	242	112	4,190	33,660	15,686	3,918	51.5	18.5	18.7	0.4	0.4	89.0	57.8	20.7	21.0	0.5	100
	9H-5, 71–73	A	78.07	64	1,065	221	82	3,965	34,734	15,175	3,059	48.8	19.1	18.0	-0.6	0.0	85.9	56.8	22.3	21.0	0.0	100
	9H-5, 73–75	A	78.09	85	1,106	204	90	3,688	33,869	15,291	2,952	46.2	18.7	18.3	-0.5	0.0	83.1	55.5	22.5	22.0	0.0	100
IIA	9H-5, 71–73	A	78.07	65	765	179	26	4,354	23,736	11,048	709	50.0	12.8	12.8	-3.4	0.0	75.6	66.2	16.9	16.9	0.0	100
	9H-5, 73–75	A	78.09	77	934	214	52	4,997	29,795	12,987	1,048	57.5	16.2	14.9	-3.7	0.0	88.7	64.9	18.2	16.9	0.0	100
	9H-5, 75–77	A	78.11	89	1,013	195	3	4,592	35,416	14,708	1,052	54.5	19.5	17.2	-3.6	0.0	91.1	59.8	21.4	18.8	0.0	100
	9H-5, 77–79	A	78.13	94	1,123	238	42	5,513	37,370	14,772	1,389	63.6	20.5	16.9	-3.9	0.0	100.9	63.0	20.3	16.7	0.0	100
	9H-5, 79–81	A	78.15	100	1,005	204	39	4,945	32,674	13,430	953	57.2	17.8	15.4	-3.9	0.0	90.5	63.2	19.7	17.1	0.0	100
	9H-5, 81–89	A	78.17	70	992	191	44	5,088	33,914	13,624	1,124	58.7	18.5	15.6	-3.8	0.0	92.9	63.2	20.0	16.8	0.0	100
	9H-5, 102–103	W	78.38	77	1,053	215	35	4,472	34,224	15,229	1,448	53.8	18.8	18.0	-3.0	0.0	90.5	59.4	20.7	19.8	0.0	100
	10H-2, 103–104.5	WR	83.31	82	1,243	301	193	3,380	40,103	18,278	6,375	45.1	22.3	22.2	3.9	3.9	93.5	48.3	23.8	23.7	4.2	100
	10H-3, 0–1.5	WR	83.47	78	1,103	287	95	3,651	36,458	16,000	3,145	46.2	20.2	19.1	-0.3	0.0	85.5	54.0	23.6	22.4	0.0	100
	11H-1, 110.5–113	WR	85.91	81	1,206	229	160	3,834	37,039	14,775	5,176	47.2	20.5	17.4	2.3	2.3	87.3	54.0	23.5	19.9	2.6	100
	11H-2, 0–1.5	WR	86.24	62	996	218	161	3,639	29,840	12,853	6,344	44.2	16.4	15.1	4.2	4.2	80.0	55.3	20.5	18.9	5.3	100
	12X-6, 0–1.5	WR	94.99	74	1,167	219	106	3,881	36,591	14,656	3,303	47.5	20.3	17.2	-0.2	0.0	85.0	55.9	23.9	20.3	0.0	100



Table T4 (continued). (Continued on next page.)

Unit	Core, section, interval (cm)	Core type	Depth CSF (m)	Peak intensity (counts/step)				Integrated peak area (total counts)				Abundance calculated from SVD normalization factor											
				Clay	Quartz	Plagioclase	Calcite	Clay	Quartz	Plagioclase	Calcite	Calculated abundance (wt%)				Normalized abundance (wt%)							
												Clay	Quartz	Plagioclase	Calcite	Corrected calcite	Absolute total	Clay	Quartz	Plagioclase	Calcite	Relative total	
IIB	12X-8, 64–65.5	WR	97.32	86	1,090	229	114	3,534	35,571	14,763	4,461	44.2	19.7	17.5	1.6	1.6	83.1	53.2	23.8	21.1	1.9	100	
	13X-3, 0–1.5	WR	101.27	82	1,034	271	48	4,445	35,872	15,347	1,605	53.5	19.7	18.0	-2.9	0.0	91.3	58.6	21.6	19.8	0.0	100	
	13X-8, 10–11.5	WR	107.28	84	1,020	237	87	4,223	36,666	14,803	2,461	50.9	20.3	17.3	-1.6	0.0	88.5	57.5	22.9	19.6	0.0	100	
	14X-5, 0–1.5	WR	113.58	81	1,151	260	60	4,290	36,053	14,535	1,328	51.4	19.9	17.0	-3.1	0.0	88.3	58.2	22.5	19.2	0.0	100	
	14X-8, 15–16.5	WR	116.82	66	1,087	265	58	4,144	33,811	16,150	965	51.2	18.5	19.3	-3.4	0.0	89.1	57.5	20.8	21.7	0.0	100	
	15X-2, 0–1.5	WR	119.13	71	973	184	193	3,790	32,096	13,841	7,145	46.4	17.7	16.3	5.0	5.0	85.4	54.3	20.7	19.1	5.9	100	
	15X-7, 0–1.5	WR	125.91	78	983	194	94	4,144	34,403	12,869	3,119	48.9	19.0	14.8	-0.5	0.0	82.7	59.1	23.0	17.9	0.0	100	
316-C0004D-																							
IIB	4R-2, 0–1.5	WR	129.07	57	1,381	259	69	3,114	44,493	17,702	2,090	41.7	24.9	21.2	-1.6	0.0	87.8	47.5	28.4	24.2	0.0	100	
	5R-3, 0–1.5	WR	139.54	74	951	236	82	3,658	33,826	17,225	2,310	47.2	18.6	20.9	-1.4	0.0	86.8	54.4	21.4	24.1	0.0	100	
	7R-2, 0–1.5	WR	152.91	76	1,040	215	81	3,760	34,396	15,305	2,216	46.8	19.0	18.3	-1.5	0.0	84.0	55.7	22.6	21.7	0.0	100	
	9R-2, 93–94	W	162.84	77	936	245	61	4,363	35,819	15,137	2,253	52.6	19.7	17.8	-1.9	0.0	90.1	58.4	21.9	19.7	0.0	100	
	11R-3, 39–40	W	171.30	69	869	188	95	4,251	31,239	14,191	3,845	51.1	17.1	16.7	0.4	0.4	85.3	59.9	20.0	19.6	0.5	100	
	12R-1, 10–11	W	174.10	84	939	182	104	4,475	34,278	13,747	3,373	52.8	18.9	15.9	-0.5	0.0	87.6	60.3	21.5	18.2	0.0	100	
	13R-1, 10–11	W	178.60	73	1,356	218	47	4,321	41,717	16,135	1,073	52.6	23.1	18.9	-3.7	0.0	94.6	55.6	24.5	20.0	0.0	100	
	13R-2, 14–15	WR	179.54	75	1,189	237	89	4,430	38,073	17,790	1,996	55.1	20.9	21.3	-2.5	0.0	97.3	56.6	21.5	21.9	0.0	100	
	16R-1, 25–26	W	202.25	79	1,096	249	96	5,504	34,903	14,494	2,631	63.5	19.0	16.6	-2.2	0.0	99.1	64.0	19.2	16.8	0.0	100	
	16R-2, 13.5–15	WR	203.26	93	909	174	227	4,189	30,256	13,279	6,757	50.0	16.6	15.5	4.3	4.3	86.4	57.8	19.2	18.0	5.0	100	
	19R-1, 35–36	W	225.85	67	763	174	103	4,287	29,305	12,038	3,679	50.0	16.0	13.9	0.3	0.3	80.2	62.3	20.0	17.3	0.4	100	
	19R-2, 1–1.5	WR	226.67	77	842	215	221	4,262	29,331	14,849	7,485	51.9	16.0	17.7	5.2	5.2	90.8	57.2	17.6	19.5	5.7	100	
	21R-1, 49–51	W	238.49	66	1,175	216	56	4,956	37,379	15,651	2,227	58.8	20.5	18.2	-2.5	0.0	97.5	60.3	21.0	18.7	0.0	100	
	23R-1, 97–98.5	WR	247.97	68	853	174	125	4,038	29,088	12,305	4,179	47.7	15.9	14.3	1.1	1.1	79.1	60.3	20.2	18.1	1.4	100	
	24R-1, 105–107	W	252.55	65	970	181	82	3,284	29,843	13,705	2,786	41.2	16.4	16.4	-0.2	0.0	74.0	55.6	22.2	22.2	0.0	100	
	25R-2, 26–27	W	257.67	87	977	198	55	4,679	35,516	14,052	2,002	54.9	19.5	16.2	-2.4	0.0	90.7	60.6	21.5	17.9	0.0	100	
	III	26R-3, 0–1.5	WR	262.59	72	848	205	66	4,075	29,801	15,442	1,288	50.2	16.2	18.6	-2.8	0.0	85.0	59.1	19.1	21.9	0.0	100
		27R-2, 95.5–97	WR	267.37	76	934	181	134	5,049	31,493	11,979	4,451	57.4	17.2	13.5	0.7	0.7	88.7	64.7	19.4	15.2	0.8	100
		28R-1, 43.5–45	WR	269.94	61	801	207	122	3,759	26,509	12,521	4,356	45.2	14.5	14.8	1.6	1.6	76.2	59.4	19.0	19.4	2.2	100
		28R-2, 80–81.5	WR	271.71	73	950	191	263	3,754	31,223	13,395	9,156	45.8	17.2	15.8	7.7	7.7	86.5	52.9	19.9	18.2	8.9	100
		29R-2, 123–124	W	276.63	81	997	233	44	4,798	35,254	14,588	1,498	56.5	19.3	16.9	-3.2	0.0	92.8	60.9	20.8	18.3	0.0	100
29R-CC, 18–19		WR	277.14	78	885	182	162	4,610	30,902	12,601	5,520	53.6	16.9	14.5	2.4	2.4	87.3	61.3	19.4	16.6	2.7	100	
30R-1, 118–119		W	279.68	87	865	184	196	3,964	28,145	12,134	6,753	47.0	15.4	14.1	4.6	4.6	81.1	57.9	19.0	17.4	5.7	100	
30R-2, 53–54		W	280.44	75	865	184	223	4,000	30,802	12,566	6,846	47.6	17.0	14.6	4.6	4.6	83.7	56.8	20.3	17.4	5.5	100	
30R-2, 88–92		WR	280.79	72	892	217	266	3,996	30,347	13,130	8,536	48.0	16.7	15.4	6.8	6.8	86.9	55.3	19.2	17.7	7.8	100	
30R-3, 30–31		W	281.62	68	861	199	232	3,844	30,221	13,820	7,261	47.0	16.6	16.4	5.2	5.2	85.2	55.2	19.5	19.2	6.1	100	
30R-3, 76.5–78		WR	282.08	69	810	177	151	3,769	28,147	11,923	4,460	44.8	15.5	13.9	1.7	1.7	75.9	59.0	20.3	18.3	2.3	100	
32R-1, 63–65		W	288.13	75	991	213	142	4,480	31,454	12,775	6,447	52.4	17.3	14.7	3.7	3.7	88.1	59.5	19.6	16.7	4.2	100	
32R-2, 120–121.5		WR	290.11	81	899	232	18	4,363	32,683	15,928	1,264	53.3	17.8	19.0	-3.2	0.0	90.1	59.1	19.8	21.1	0.0	100	
32R-3, 76–77		W	291.07	81	930	207	54	4,723	32,815	13,469	1,613	55.1	18.0	15.5	-2.9	0.0	88.6	62.2	20.3	17.5	0.0	100	
34R-1, 34–16.5		WR	296.65	90	809	172	72	4,269	29,244	13,064	2,200	50.5	16.0	15.3	-1.7	0.0	81.7	61.8	19.5	18.7	0.0	100	
35R-1, 69–70		W	301.69	112	1,004	170	133	5,342	30,950	12,115	5,254	60.4	16.8	13.6	1.5	1.5	92.4	65.4	18.2	14.7	1.6	100	
36R-1, 25–27		W	305.75	77	867	186	101	4,823	29,761	12,261	3,516	55.4	16.2	14.0	-0.3	0.0	85.6	64.7	18.9	16.3	0.0	100	
36R-2, 0–1.5		WR	306.69	87	896	191	137	4,418	32,301	13,331	4,234	52.1	17.7	15.5	0.8	0.8	86.0	60.5	20.6	18.0	0.9	100	
IV		37R-1, 34–36	W	310.34	82	1,053	202	157	3,548	32,959	15,308	5,324	44.9	18.2	18.4	2.8	2.8	84.2	53.3	21.6	21.8	3.3	100
		37R-1, 59–61.5	WR	310.59	64	968	216	105	3,651	32,461	16,586	3,783	46.8	17.8	20.1	0.6	0.6	85.4	54.8	20.8	23.6	0.8	100
	38R-CC, 17–18	W	315.44	75	971	255	169	3,346	32,116	17,538	4,778	44.6	17.6	21.5	2.1	2.1	85.9	51.9	20.5	25.1	2.5	100	
39R-2, 8–9.5	WR	320.18	60	1,161	313	113	2,978	36,744	20,436	3,508	42.8	20.3	25.4	0.5	0.5	88.9	48.1	22.8	28.6	0.6	100		



Table T4 (continued).

Unit	Core, section, interval (cm)	Core type	Depth CSF (m)	Peak intensity (counts/step)				Integrated peak area (total counts)				Abundance calculated from SVD normalization factor									
				Clay	Quartz	Plagioclase	Calcite	Clay	Quartz	Plagioclase	Calcite	Calculated abundance (wt%)				Normalized abundance (wt%)					
												Clay	Quartz	Plagioclase	Calcite	Corrected calcite	Absolute total	Clay	Quartz	Plagioclase	Calcite
40R-1, 104–106	W	324.54	88	1,019	221	264	3,025	32,245	14,574	9,420	39.4	17.9	17.5	8.6	8.6	83.4	47.3	21.4	21.0	10.3	100
41R-2, 20–21.5	WR	329.60	60	1,080	261	150	3,093	36,073	18,841	4,911	42.8	19.9	23.2	2.3	2.3	88.3	48.5	22.6	26.3	2.6	100
42R-1, 68–69	W	333.18	66	1,168	297	121	3,271	39,292	21,540	4,227	46.4	21.7	26.7	1.1	1.1	95.9	48.4	22.6	27.9	1.2	100
42R-CC, 12–13	W	336.62	38	876	266	887	1,149	24,395	13,097	26,501	20.9	13.7	16.4	32.6	32.6	83.5	25.0	16.4	19.6	39.0	100
44R-2, 71–72.5	WR	343.61	77	922	286	180	2,895	33,667	20,073	5,849	41.9	18.5	25.1	3.7	3.7	89.2	47.0	20.7	28.1	4.2	100
44R-3, 0–1.5	WR	344.09	70	1,118	251	112	3,084	38,181	19,364	3,016	42.9	21.1	23.8	-0.2	0.0	87.9	48.8	24.0	27.1	0.0	100
45R-1, 61–63	W	346.61	78	1,024	213	182	3,597	32,521	13,125	6,312	43.9	18.0	15.4	4.1	4.1	81.4	53.9	22.1	18.9	5.1	100
46R-1, 41–44	W	350.91	51	1,452	351	93	2,209	41,684	26,143	2,730	39.0	23.0	33.2	-0.3	0.0	95.3	41.0	24.2	34.9	0.0	100
46R-2, 28.5–30	WR	352.20	72	1,033	308	103	2,734	35,990	20,581	3,907	40.5	19.9	25.7	1.2	1.2	87.3	46.4	22.7	29.5	1.4	100
48R-1, 37–38.5	WR	359.87	74	881	284	108	3,176	30,350	16,820	3,595	42.4	16.6	20.7	0.8	0.8	80.5	52.6	20.7	25.7	1.0	100
48R-1, 132–134	W	360.82	55	966	298	65	2,635	32,244	18,073	2,410	37.8	17.8	22.5	-0.4	0.0	78.1	48.4	22.8	28.8	0.0	100
48R-2, 17–18.5	WR	361.07	75	1,044	317	130	2,782	34,491	20,401	4,145	40.9	19.0	25.5	1.6	1.6	87.0	47.1	21.8	29.3	1.8	100
49R-1, 111–112.5	WR	365.11	79	1,137	210	65	3,864	37,293	15,740	2,072	48.0	20.6	18.7	-1.9	0.0	87.3	55.0	23.6	21.4	0.0	100
49R-2, 30–31.5	WR	365.72	91	1,086	303	80	3,263	38,654	22,147	2,232	46.7	21.3	27.6	-1.5	0.0	95.5	48.9	22.3	28.9	0.0	100
49R-3, 79–80.5	WR	367.61	82	1,014	259	48	3,622	37,172	16,426	1,235	46.1	20.6	19.7	-2.8	0.0	86.4	53.4	23.8	22.8	0.0	100
51R-1, 90.5–92	WR	373.91	69	875	229	126	3,311	30,922	15,001	3,978	42.4	17.0	18.1	1.3	1.3	78.8	53.8	21.6	23.0	1.6	100
51R-2, 50.5–52	WR	374.92	73	1,069	215	140	3,598	36,139	16,060	4,412	45.8	20.0	19.2	1.4	1.4	86.4	53.0	23.1	22.3	1.6	100
51R-2, 103–104.5	WR	375.45	71	1,163	323	135	2,837	36,168	20,232	4,351	41.3	20.0	25.2	1.7	1.7	88.2	46.8	22.6	28.6	2.0	100
52R-1, 10–11	WR	377.60	83	928	231	111	3,523	32,251	16,679	3,853	45.6	17.7	20.3	0.8	0.8	84.5	54.0	20.9	24.0	1.0	100
52R-2, 79–80.5	WR	379.69	57	935	295	89	3,171	33,436	22,930	3,070	46.6	18.2	28.9	-0.2	0.0	93.7	49.7	19.4	30.9	0.0	100
52R-3, 18–19.5	WR	380.49	64	1,084	223	102	3,446	32,027	15,762	4,107	44.2	17.6	19.1	1.3	1.3	82.2	53.8	21.4	23.2	1.5	100
52R-3, 76.5–78	WR	381.07	52	1,191	299	89	2,828	36,357	23,409	2,572	43.4	19.9	29.5	-0.7	0.0	92.9	46.7	21.5	31.8	0.0	100
52R-3, 110.5–112	WR	381.41	90	1,003	226	48	3,685	32,044	17,287	1,064	47.6	17.5	21.1	-2.9	0.0	86.2	55.2	20.3	24.5	0.0	100
53R-2, 51–52.5	WR	383.92	66	840	235	77	3,107	27,321	16,227	1,704	41.3	14.9	20.1	-1.5	0.0	76.3	54.2	19.5	26.3	0.0	100
54R-1, 107.5–109	WR	387.58	55	884	211	158	3,364	30,250	17,325	4,759	44.7	16.5	21.3	2.2	2.2	84.7	52.7	19.5	25.2	2.6	100
54R-2, 11.5–13	WR	388.02	40	992	371	158	1,925	29,798	23,163	5,023	34.7	16.2	29.8	3.4	3.4	84.1	41.3	19.3	35.4	4.0	100
54R-2, 116–117.5	WR	389.06	69	890	210	227	3,436	29,933	17,275	6,980	45.5	16.3	21.2	5.0	5.0	88.1	51.6	18.5	24.1	5.7	100
54R-3, 0–1.5	WR	389.31	52	994	297	209	3,081	33,489	17,597	8,368	42.1	18.5	21.6	7.0	7.0	89.1	47.2	20.7	24.2	7.8	100
54R-3, 44–44.5	WR	389.75	76	1,093	260	190	3,366	32,573	17,625	6,026	44.9	17.9	21.6	3.7	3.7	88.1	50.9	20.3	24.5	4.2	100
54R-3, 77.5–79	WR	390.09	66	845	219	129	2,721	29,954	16,896	4,360	38.0	16.5	20.9	2.2	2.2	77.6	49.0	21.2	27.0	2.8	100
55R-1, 36–37.5	WR	391.36	75	1,004	220	148	3,105	34,710	18,353	4,549	42.6	19.1	22.6	1.9	1.9	86.3	49.4	22.2	26.2	2.2	100
55R-2, 97–98.5	WR	393.38	69	1,177	442	112	3,034	39,265	23,249	3,421	45.2	21.6	29.1	0.2	0.2	96.2	47.0	22.5	30.3	0.2	100

Notes: CSF = core depth below seafloor. SVD = singular value decomposition. WR = whole-round, W = working half, A = archive half.

Table T5. XRD mineralogy by unit.

Mineral	Maximum	Minimum	Average	Standard deviation
Unit I				
Clay	61.7	39.0	51.3	5.6
Quartz	25.7	17.2	20.7	2.0
Plagioclase	25.0	13.3	18.8	2.9
Calcite	25.9	0.0	9.2	8.1
Subunit IIA				
Clay	66.2	48.3	58.4	4.7
Quartz	23.9	16.9	21.4	2.1
Plagioclase	23.7	16.7	19.4	2.1
Calcite	5.3	0.0	0.8	1.7
Subunit IIB				
Clay	64.0	28.4	24.2	5.9
Quartz	47.5	17.6	16.8	0.0
Plagioclase	57.8	21.5	19.7	1.1
Calcite	3.7	2.3	2.2	2.1
Unit III				
Clay	65.4	52.9	59.8	3.4
Quartz	20.8	18.2	19.6	0.7
Plagioclase	21.9	14.7	17.9	1.8
Calcite	8.9	0.0	2.7	2.9
Unit IV				
Clay	55.2	25.0	49.3	5.5
Quartz	24.2	16.4	21.4	1.7
Plagioclase	35.4	18.9	26.1	3.9
Calcite	39.0	0.0	3.1	6.6



**Table T6.** Calcareous nannofossil range chart of age-diagnostic fossils, Hole C0004C. (See table notes.)

Epoch	Nannofossil zone	Core, section, interval (cm)	Depth CSF (m)			Abundance	Preservation	<i>Calcidiscus macintyrei</i>	<i>Ceratolithus acutus</i>	<i>Ceratolithus rugosus</i>	<i>Discoaster asymmetricus</i>	<i>Discoaster bellus</i>	<i>Discoaster bergeni</i>	<i>Discoaster brouweri</i>	<i>Discoaster pentaradiatus</i>	<i>Discoaster surculus</i>	<i>Discoaster tamalis</i>	<i>Emiliana huxleyi</i>	<i>Gephyrocapsa</i> spp. large (>5.5 µm)	<i>Gephyrocapsa</i> spp. medium I (>3.5-4 µm)	<i>Gephyrocapsa</i> spp. medium II (>4-5.5 µm)	<i>Gephyrocapsa</i> spp. smaller (3.5 µm)	<i>Helicosphaera sellii</i>	<i>Pseudoemiliana lacunosa</i>	<i>Reticulofenestra asanoi</i>	<i>Reticulofenestra pseudoumbilicus</i> (>7 µm)	<i>Sphenolithus abies</i>
			Top	Bottom	Mean																						
Pleistocene	NN20	316-C0004C-1H-CC, 0-5	6.25	6.30	6.27	D	VG												C	D	D	D					
		2H-CC, 0-5	16.31	16.36	16.33	A	VG													A	C	D			C		
	NN19	3H-CC, 0-5	25.57	25.62	25.60	A	G													C	C	D			A	A	
		4H-CC, 5-10	35.34	35.39	35.36	A	G	T												C	F	D			C		
		5H-CC, 4-9	44.93	44.98	44.96	A	M	T												C	F	D			C		
		6H-CC, 11-16	54.60	54.65	54.62	A	VG	T												A	C	D			C		
		7H-CC, 0-5	63.77	63.82	63.79	A	G	R												A	C	A	D		C		
		8H-CC, 23.5-28.5	73.62	73.67	73.64	C	M	R						T						A	A	A	A		A		
		9H-2, 94	75.23		75.23	A	M	F												R	R	F	C		C		
		9H-5, 74	78.10		78.10	T	M	F												R	C	R	C		R		
?	?	9H-5, 94	78.30		78.30	B																					
middle Pliocene	NN16	9H-6, 17	78.76		78.76	B																					
		9H-6, 44	79.03		79.03	A	M		T	T				C	F	T	T										
		9H-CC, 0-5	80.87	80.92	80.90	F	M	T		R				F	F	F	T								C		
		10H-CC, 0-5	84.62	84.67	84.64	F	G	T			T			F	C	T							F			C	
		11H-CC, 0-5	89.20	89.25	89.23	R	M	R			T			T	C	R	R								R		T
		12X-CC, 0-5	98.49	98.54	98.51	F	M	F	T	T	R				C	C	T	T									
		13X-CC, 25.5-30.5	108.37	108.42	108.40	R	M	F	T	T					R	R	R	T									
		14X-CC, 0-5	117.77	117.82	117.80	R	M	F	T						C	C	T	T									
		15X-CC, 0-5	127.28	127.33	127.31	R	M	F	T						C	R	R	T									
		16H-CC, 4-9	128.81	128.86	128.84	R	M	F	R		R	T			C	C	F	T									T
17H-CC, 20.5-26	133.26	133.31	133.28	R	M	R	R					T	C	R	F	T									T		
18H-CC, 45-50	134.92	134.97	134.95	T	P	T	T						R	T	T												

Notes: CSF = core depth below seafloor. Abundance: D = dominant, A = abundant, C = common, F = few, R = rare, T = trace, B = barren. Preservation: VG = very good, G = good, M = medium, P = poor. ? = undetermined.

Table T7. Calcareous nannofossil range chart of age-diagnostic fossils, Hole C0004D. (See table notes.) (Continued on next page.)

Epoch	Nannofossil zone	Core, section, interval (cm)	Depth CSF (m)			Abundance	Preservation	<i>Calcidiscus macintyreii</i>	<i>Ceratolithus acutus</i>	<i>Ceratolithus rugosus</i>	<i>Discoaster asymmetricus</i>	<i>Discoaster brouweri</i>	<i>Discoaster pentaradiatus</i>	<i>Discoaster surculus</i>	<i>Discoaster tamalis</i>	<i>Discoaster triradiatus</i>	<i>Gephyrocapsa</i> spp. large (>5.5 µm)	<i>Gephyrocapsa</i> spp. medium I (>3.5–4 µm)	<i>Gephyrocapsa</i> spp. medium II (>4–5.5 µm)	<i>Gephyrocapsa</i> spp. smaller (3.5 µm)	<i>Helicosphaera sellii</i>	<i>Pseudoemiliania lacunosa</i>	<i>Reticulofenestra pseudoambilicus</i> (>7 µm)	<i>Sphenolithus abies</i>	
			Top	Bottom	Mean																				
early-middle Pliocene	NN16	316-C0004D-																							
		1R-CC, 0–5	103.81	103.86	103.84	F	G	F	T		F	R	T												
		2R-CC, 0–5	110.81	110.86	110.84	C	G	F	R	T		F	R	R	T										
		3R-CC, 0–5	120.40	120.45	120.43	C	M	F	T	T		F	R	R	T										
		4R-CC, 8.5–13.5	129.43	129.48	129.46	C	G	F	T			F	F	R	T										
		5R-CC, 0–5	140.20	140.25	140.23	F	M	F	T			F	R	R	T										
		7R-CC, 0–5	153.76	153.81	153.79	R	M	F	T			R	R												
		8R-CC, 9–14	157.46	157.51	157.48	R	M	F	T			T	T												
		9R-CC, 0–5	163.01	163.06	163.04	R	M	F		T	R	T	T												
		10R-CC, 0–5	165.00	165.05	165.03	F	M	F	T			F	R	T	T										
		11R-CC, 0–5	171.38	171.43	171.40	F	M	F				F	F	R	T										
		12R-CC, 0–5	175.17	175.22	175.19	C	G	F		T		F	F	T	T										
		13R-CC, 26–31	179.81	179.86	179.83	T	M					T													
		16R-CC, 20.5–25.5	203.49	203.54	203.51	C	M	F	T		R	F	F	T											
		19R-CC, 0–5	226.98	227.03	227.00	C	M	F	T		T	F	F	R	T										
20R-CC, 10–15	228.77	228.82	228.80	C	M	F	T	T		F	F	R					R	R							
21R-CC, 0–5	238.62	238.67	238.65	C	M	F	T		T	C	F	R	T												
22R-CC, 0–5	243.76	243.81	243.79	C	M	T		T	R	F	R	R	T					R	R						
24R-CC, 0–5	253.92	253.97	253.94	R	M	R		T		T	T	T													
25R-1, 79			256.79	C	M	R				T	T	T													
?	?	257.72	257.77	257.75	B																				
middle Pliocene	NN16	26R-1, 19			260.69	C	M	R	T	T	R	F	C	R	T										
		26R-CC, 0–5	262.80	262.85	262.83	C	M	R	T	T	R	F	F	R	T										
		27R-CC, 0–5	267.39	267.44	267.41	C	M	R		T	R	F	F	R	T										
		28R-CC, 0–5	272.97	273.02	273.00	C	M	R			T	F	F	R	T										
		29R-CC, 27.5–32.5	277.23	277.28	277.26	T	P					T	T	T											
		30R-CC, 7.5–12.5	282.37	282.42	282.40	C	M	R				R	F	F	R	T									
		31R-CC, 3–8	287.13	287.18	287.16	C	M	F				R	F	F	R	T									
		32R-CC, 0–5	291.94	291.99	291.97	C	M	F				R	F	F	R	T									
		33R-1, 20			292.20	R	M	F				R	R	R	T										
		33R-CC, 0–5	296.06	296.11	296.09	T	P						T	T											
?	?	34R-1, 77			297.27	B																			
		34R-CC, 0–5	298.39	298.44	298.41	B																			
		35R-1, 38			301.38	C	M	C				F	C	F											
		35R-CC, 0–4	302.61	302.65	302.63	A	M	F	T	T	R	R	R												
		36R-1, 50			306.00	R	P	F				R	R												
		36R-CC, 0–5	307.47	307.52	307.50	R	M	T		T	T	R	R	T	R	T									
		37R-1, 16			310.16	C	M	R										F							
		37R-CC, 0–1	312.62	312.63	312.62	T	P																		
		38R-1, 12			314.62	C	M	R																	
		38R-CC, 0–5	315.27	315.32	315.29	C	G	R	T																
early Pleistocene	NN19	39R-CC, 0–5	321.82	321.87	321.85	A	G	R																	
		40R-CC, 4–9	325.43	325.48	325.45	C	G	R																	
		41R-CC, 0–5	330.37	330.42	330.40	C	G	F																	
		42R-CC, 5–10	336.55	336.60	336.57	C	M	F																	
		43R-CC, 5–10	340.09	340.14	340.11	A	G	F																	
		44R-CC, 0–5	345.22	345.27	345.25	A	G	F																	
		45R-CC, 0–5	347.92	347.97	347.95	C	G	R																	
		46R-CC, 0–5	352.36	352.41	352.39	F	G	R																	
		47R-CC, 14–19	358.31	358.36	358.33	F	M	R																	
		48R-CC, 0–5	361.79	361.84	361.81	F	M	F						T	T										
		49R-CC, 17–22	368.40	368.45	368.42	F	M	R						T											
		50R-CC, 16–21	370.75	370.80	370.78	R	M	R																	
		51R-CC, 10–15	377.12	377.17	377.14	F	M	R																	
		52R-CC, 0–5	381.66	381.71	381.68	B																			



Table T7 (continued).

Epoch	Nannofossil zone	Core, section, interval (cm)	Depth CSF (m)			Abundance	Preservation	<i>Calcidiscus macintyreii</i>	<i>Ceratolithus acutus</i>	<i>Ceratolithus rugosus</i>	<i>Discoaster asymmetricus</i>	<i>Discoaster brouweri</i>	<i>Discoaster pentaradiatus</i>	<i>Discoaster surculus</i>	<i>Discoaster tamalis</i>	<i>Discoaster triradiatus</i>	<i>Gephyrocapsa</i> spp. large (>5.5 μm)	<i>Gephyrocapsa</i> spp. medium I (>3.5–4 μm)	<i>Gephyrocapsa</i> spp. medium II (>4–5.5 μm)	<i>Gephyrocapsa</i> spp. smaller (3.5 μm)	<i>Helicosphaera sellii</i>	<i>Pseudoemiliana lacunosa</i>	<i>Reticulofenestra pseudoumbilicus</i> (>7 μm)	<i>Sphenolithus abies</i>		
			Top	Bottom	Mean																					
early Pleistocene	NN19	53R-1, 59			382.59	F	M	R																		
		53R-CC, 0–5	384.56	384.61	384.58	F	M	R																		
		54R-CC, 0–5	390.89	390.94	390.91	R	P																			
		55R-CC, 16–21	394.74	394.79	394.76	F	G	R			T	T														
		56R-CC, 0–5	398.64	398.69	398.67	T	P	T																		
		56R-CC, 14			398.78	F	M	R																		

Notes: CSF = core depth below seafloor. Abundance: A = abundant, C = common, F = few, R = rare, T = trace, B = barren. Preservation: G = good, M = medium, P = poor. ? = undetermined.

Table T8. Recognized nannofossil events, Hole C0004C. (See table notes.)

Epoch	Zone (top)	Age (Ma)	Nannofossil event	Top		Bottom		Mean depth CSF (m)
				Core, section, interval (cm)	Depth CSF (m)	Core, section, interval (cm)	Depth CSF (m)	
Pleistocene	NN20	0.44	LO <i>Pseudoemiliana lacunosa</i>	316-C0004C-1H-CC, 0–5	6.27	316-C0004C-2H-CC, 0–5	16.33	11.30
		0.90	LCO <i>Reticulofenestra asanoi</i>	2H-CC, 0–5	16.31	3H-CC, 0–5	25.60	20.95
	NN19	1.078*	FCO <i>Reticulofenestra asanoi</i>	3H-CC, 0–5	25.60	4H-CC, 5–10	35.36	30.48
		1.24	LO <i>Gephyrocapsa</i> spp. large (>5.5 μm)	4H-CC, 5–10	35.36	5H-CC, 4–9	44.96	40.16
		1.46	FCO <i>Gephyrocapsa</i> spp. large (>5.5 μm)	8H-CC, 23.5–28.5	73.64	9H-2, 94	75.23	74.44
		1.60	LO <i>Calcidiscus macintyreii</i> (≥11 μm)	8H-CC, 23.5–28.5	73.64	9H-2, 94	75.23	74.44
		2.06	LO <i>Discoaster brouweri</i>	9H-6, 17	78.76	9H-6, 44	79.03	78.90
middle Pliocene	NN16	2.393–2.512*	LO <i>Discoaster pentaradiatus</i>	9H-6, 17	78.76	9H-6, 44	79.03	78.90
		2.52	LO <i>Discoaster surculus</i>	9H-6, 44	79.03	9H-CC, 0–5	80.87	79.95
		2.87	LO <i>Discoaster tamalis</i>	11H-CC, 0–5	89.23	12X-CC, 0–5	98.51	93.87

Notes: \* = data based on Atlantic or Mediterranean records. CSF = core depth below seafloor. LO = last occurrence, LCO = last consistent occurrence, FCO = first consistent occurrence.



Table T9. Recognized nannofossil events, Hole C0004D. (See table notes.)

Epoch	Zone (top)	Age (Ma)	Nannofossil event	Top		Bottom		Mean depth CSF (m)
				Core, section, interval (cm)	Depth CSF (m)	Core, section, interval (cm)	Depth CSF (m)	
early-middle Pliocene	NN16	2.52	LO <i>Discoaster surculus</i>	316-C0004D-1R-CC, 0-5	103.84	316-C0004D-2R-CC, 0-5	110.84	107.34
		2.87	LO <i>Discoaster tamalis</i>	1R-CC, 0-5	103.84	2R-CC, 0-5	110.84	107.34
		3.65	LO <i>Sphenolithus</i> spp.	16R-CC, 20.5-25.5	203.51	19R-CC, 0-5	227.00	215.26
-- -- -- --	NN15-14	3.79	LO <i>Reticulofenestra pseudoumbilicus</i> (>7 µm)	19R-CC, 0-5	227.00	20R-CC, 10-15	228.80	227.90
		4.13	FO <i>Discoaster asymmetricus</i>	25R-1, 79	256.79	25R-CC, 0-5	257.75	257.27
-- -- -- --	middle Pliocene	2.06	LO <i>Discoaster brouweri</i>	25R-CC, 0-5	257.75	26R-1, 19	260.69	259.22
		2.393-2.512*	LO <i>Discoaster pentaradiatus</i>	25R-CC, 0-5	257.75	26R-1, 19	260.69	259.22
-- -- -- --	NN16	2.52	LO <i>Discoaster surculus</i>	25R-CC, 0-5	257.75	26R-1, 19	260.69	259.22
		2.87	LO <i>Discoaster tamalis</i>	25R-CC, 0-5	257.75	26R-1, 19	260.69	259.22
-- -- -- --	early Pleistocene	3.65	LO <i>Sphenolithus</i> spp.	32R-CC, 0-5	291.97	33R-1, 20	292.20	292.08
		1.60	LO <i>Calcidiscus macintyreii</i> (≥11 µm)	36R-CC, 0-5	307.50	37R-1, 16	310.16	308.83
-- -- -- --	NN19	1.560-1.617*	FO <i>Gephyrocapsa</i> spp. large (>5.5 µm)	43R-CC, 5-10	340.11	44R-CC, 0-5	345.25	342.68
		1.67	FO <i>Gephyrocapsa</i> spp. medium I (>3.5-4 µm)	55R-CC, 16-21	394.76	56R-CC, 0-5	398.67	396.71

Notes: \* = data based on Atlantic or Mediterranean records. CSF = core depth below seafloor. FO = first occurrence, LO = last occurrence. Dashed lines = undetermined interval.

**Table T10.** Paleomagnetic and biostratigraphic age datums, Site C0004. (See table note.)

Datum		Age (Ma)		Hole C0004C Depth CSF (m)		Hole C0004D Depth CSF (m)		Sedimentation rate (m/m.y.)
Magnetostratigraphy (chron/subchron)	Biostratigraphy (nannofossil zone)	Magnetostratigraphy	Biostratigraphy	Magnetostratigraphy	Biostratigraphy	Magnetostratigraphy	Biostratigraphy	
Emperor	NN20	0.42	0.29–0.44	6.25–7.25	6.29			17
Brunhes/Matuyama	NN19h	0.78	0.44–0.90	15.87	16.35		314.62	20
Jaramillo	NN19f	0.99–1.07	0.89–1.078	17.92–40.18	25.62–35.33			265
Olduvai	NN19a	1.77–1.95	1.66–1.91	50.78–54.20		356.68	352.41	19
Reunion	NN18	2.14–2.15	1.95–2.36					47
	NN17		2.39–2.52		79.03–89.25			
Matuyama/Gauss	NN16	2.58	2.65–3.65	102.20	98.51–134.92	320.00–390.00	103.86–227.02	40
Gauss/Gilbert	NN15	3.59				242.55	228.80–243.81	

Note: CSF = core depth below seafloor.

**Table T11.** AMS measurements, Hole C0004C. (See table notes.)

Core, section, interval (cm)	Depth top CSF (m)	Susceptibility (SI)				<i>L</i>	<i>F</i>	<i>P</i>	<i>T</i>	K1 (°)		K2 (°)		K3 (°)		NRM (A/m)	Q-ratio
		Km	K1	K2	K3					Dec.	Inc.	Dec.	Inc.	Dec.	Inc.		
316-C0004C-																	
9H-3, 90–92	76.60	7.060E-04	7.121E-04	7.065E-04	6.992E-04	1.008	1.010	1.018	0.136	329.3	69.5	121.7	18.3	214.7	8.9	3.0489E-05	1.187E-02
9H-5, 33–35	77.69	5.908E-04	6.052E-04	5.911E-04	5.761E-04	1.024	1.026	1.050	0.044	131.8	11.9	32.6	37.1	236.6	50.4	2.2826E-05	1.062E-02
9H-5, 51–53	77.87	5.166E-04	5.225E-04	5.212E-04	5.060E-04	1.002	1.030	1.033	0.845	73.7	48.3	174.1	9.1	271.9	40.2	1.9161E-05	1.019E-02
9H-5, 84–86	78.20	1.500E-02	1.504E-04	1.500E-04	1.495E-04	1.003	1.003	1.006	0.074	325.6	1.4	56.7	38.6	233.8	51.3	1.0450E-06	1.914E-05
9H-5, 105–107	78.41	9.810E-03	9.868E-05	9.795E-05	9.767E-05	1.007	1.003	1.010	-0.444	31.5	7.7	126.6	32.8	289.9	56.0	1.7076E-06	4.783E-05
9H-6, 42–44	79.01	1.013E-04	1.017E-04	1.013E-04	1.010E-04	1.003	1.003	1.007	0.026	162.7	20.0	21.7	65.0	258.1	14.5	1.9561E-06	5.306E-03
9H-7, 53–55	80.53	1.922E-04	1.935E-04	1.926E-04	1.904E-04	1.005	1.012	1.016	0.438	213.6	13.1	92.1	66.0	308.4	19.8	1.2522E-05	1.790E-02

Notes: Km and K1, K2, and K3 represent bulk magnetic susceptibility and three principal axes of the magnetic ellipsoid, respectively.  $L = K1/K2$ .  $F = K2/K3$ .  $P = K1/K3$ .  $T = \{2 \times [\ln(K2) - \ln(K1) - \ln(K3)] / [\ln(K1) - \ln(K3)]\}$ . The International Geomagnetic Reference Field value at Site C0004 (45,706 nT) was used to calculate Q-ratios. Orientations in core coordinate system. CSF = core depth below seafloor. Dec. = declination, Inc. = inclination. NRM = natural remanent magnetization.

Table T12. Uncorrected geochemistry results from interstitial waters, Site C0004. (See table notes.)

Core, section	Depth CSF (m)			pH	Alkalinity (mM)	Salinity	Chlorinity (mM)	Cl (mM)	Br (mM)	SO <sub>4</sub> (mM)	Na (mM)	Na (mM)*	K (mM)	Mg (mM)	Ca (mM)	PO <sub>4</sub> (μM)	NH <sub>4</sub> (μM)
	Top	Bottom	Average														
316-C0004C-																	
1H-3	2.62	2.84	2.73	7.5	4.5	34.49	555	554	0.89	25.3	465	485	12.2	47.8	8.57	15.2	146
1H-6	5.44	5.65	5.54	7.9	7.0	34.17	557	556	0.95	17.2	481	479	12.0	45.9	7.28	13.7	30
2H-3	8.98	9.20	9.09	8.3	6.0	34.06	566	565	0.91	13.9	465	486	11.5	44.8	5.90	26.7	321
2H-7	13.28	13.49	13.38	8.3	11.2	33.68	569	568	0.93	6.9	455	491	11.3	41.1	4.43	33.9	428
3H-5	19.90	20.12	20.01	8.4	13.9	33.36	578	577	0.96	0.9	478	499	11.2	38.4	3.09	33.9	564
3H-8	22.76	22.98	22.87	8.3	18.3	33.36	569	568	0.96	0.0	481	492	11.3	38.0	3.12	41.1	602
4H-4	29.41	29.63	29.52	8.0	16.2	33.30	584	583	0.99	0.0	489	507	10.7	37.3	3.15	49.7	768
5H-4	39.07	39.28	39.17	7.9	15.8	33.52	584	583	1.02	0.0	514	509	10.6	36.1	3.54	55.4	981
6H-4	48.48	48.69	48.58	7.7	14.5	33.63	577	576	1.01	0.0	479	509	9.2	31.1	4.55	48.2	1214
7H-6	59.34	59.56	59.45	7.7	14.6	33.95	591	590	1.06	0.0	506	518	10.0	34.0	4.10	20.9	1311
8H-4	67.63	67.85	67.74	7.7	13.8	34.17	601	600	1.08	0.0	493	523	10.5	34.8	4.38	13.7	1554
9H-4	77.14	77.36	77.25	7.7	14.6	34.38	601	600	1.09	0.0	498	525	10.4	33.9	4.93	16.6	1612
10H-3	83.47	83.69	83.58	7.8	13.9	34.49	605	604	1.09	0.0	512	529	10.8	33.3	5.02	9.4	1700
11H-2	86.24	86.46	86.35	7.7	14.0	34.55	607	606	1.13	0.0	499	532	10.1	33.0	5.27	8.0	1855
12X-6	94.99	95.26	95.12	7.8	13.2	34.92	613	612	1.12	0.0	496	536	10.0	33.0	5.63	10.8	1952
13X-3	101.27	101.54	101.40	7.8	11.1	34.98	614	612	1.12	3.4	532	538	10.4	34.1	6.28	3.6	2040
14X-5	113.58	113.86	113.72	7.8	13.3	35.90	625	624	1.13	0.0	525	555	10.8	31.9	6.51	3.6	2341
15X-7	125.91	126.19	126.05	7.7	11.3	35.57	643	642	1.20	0.0	498	564	9.6	32.3	6.60	10.8	2515
316-C0004D-																	
3R-2	119.89	120.10	119.99	—	—	35.14	613	612	1.12	2.6	495	536	10.1	33.5	6.72	3.1	2980
4R-2	129.07	129.27	129.17	—	—	35.25	622	623	1.13	1.8	508	549	10.2	31.5	6.58	1.8	3229
5R-3	139.54	139.84	139.69	7.8	11.6	35.41	626	625	1.09	2.4	530	554	10.4	30.4	6.97	0.0	3376
7R-2	152.91	153.26	153.08	7.8	11.1	35.46	629	628	1.15	1.7	527	555	10.4	29.9	7.46	1.8	3712
13R-2	179.40	179.55	179.47	7.9	14.6	35.68	620	619	1.17	2.0	507	557	9.4	26.2	7.67	0.0	4393
16R-2	203.13	203.28	203.20	7.6	10.3	35.79	635	634	1.20	1.6	509	566	8.8	26.1	8.31	11.5	4408
19R-2	226.66	226.98	226.82	7.6	8.7	35.46	619	617	1.12	6.0	522	550	8.9	28.7	8.97	10.1	4694
23R-1	247.97	248.27	248.12	7.3	7.8	35.41	607	606	1.09	9.6	520	543	8.4	29.4	9.17	12.8	5118
26R-3	262.59	262.80	262.69	7.4	10.4	36.28	636	635	1.17	2.5	551	570	8.5	24.5	9.40	4.7	5420
28R-2	271.71	272.11	271.91	7.5	10.0	35.79	629	628	1.16	1.6	527	565	8.3	23.1	8.78	3.3	5371
30R-3	282.08	282.30	282.19	7.6	7.6	35.68	631	630	1.16	2.5	554	566	8.7	23.1	8.47	6.0	5363
32R-3	290.11	290.31	290.21	7.7	10.2	35.79	633	631	1.20	1.9	540	569	8.3	22.5	9.23	3.3	5396
34R-1	296.65	296.85	296.75	—	—	35.68	627	626	1.16	2.5	539	562	7.9	22.8	9.22	4.7	5565
36R-2	306.69	306.91	306.80	7.4	7.5	35.41	610	609	1.10	8.6	530	551	7.8	25.8	9.40	8.8	5889
39R-2	320.18	320.41	320.29	7.4	8.7	35.79	629	628	1.16	4.1	549	568	8.1	22.5	9.23	6.0	6164
41R-2	329.40	329.49	329.45	7.3	7.6	35.52	615	614	1.14	7.4	540	557	8.0	23.9	9.33	6.0	5897
44R-3	344.09	344.31	344.20	7.4	7.1	35.30	609	607	1.10	10.1	511	549	7.8	27.2	9.45	3.3	5428
46R-2	351.91	352.21	352.06	7.5	9.1	35.68	629	628	1.21	2.0	548	570	7.5	20.0	9.36	4.7	6099
48R-2	361.07	361.25	361.16	8.2	9.0	35.63	631	630	1.17	1.7	543	572	8.4	19.5	8.64	3.3	6430
49R-2	365.72	365.91	365.81	7.8	8.2	35.68	634	633	1.22	1.4	535	575	8.0	19.0	8.84	3.3	6067
51R-2	375.45	375.82	375.63	7.9	8.6	36.01	642	641	1.20	0.9	561	583	8.2	18.4	8.96	6.0	6131
53R-2	383.92	384.29	384.10	7.9	8.4	35.95	643	642	1.22	0.0	562	583	8.4	18.1	9.05	0.0	6309
55R-2	393.38	393.81	393.60	7.9	7.4	36.01	645	644	1.23	1.4	555	586	8.3	18.3	8.95	1.9	6447

Notes: \* = calculated by charge balance. CSF = core depth below seafloor. — = not analyzed.

Table T13. Uncorrected concentrations of minor elements in interstitial waters, Site C0004. (See table notes.)

Core, section	Depth CSF (m)			Minor elements (µm)							
	Top	Bottom	Average	Li	B	Sr	Ba*	Ba†	Si	Fe	Mn
316-C0004C-											
1H-3	2.62	2.84	2.73	24.3	498	84	0.45	0.47	625	2.5	2.5
1H-6	5.44	5.65	5.54	24.0	519	83	0.44	0.46	676	0.2	1.3
2H-3	8.98	9.20	9.09	25.2	478	86	0.67	0.68	695	0.1	0.6
2H-7	13.28	13.49	13.38	23.3	502	84	1.3	1.28	682	1.0	0.3
3H-5	19.90	20.12	20.01	18.9	446	90	50	50.94	686	0.0	0.1
3H-8	22.76	22.98	22.87	18.8	438	93	54	64.70	764	0.3	0.2
4H-4	29.41	29.63	29.52	18.5	408	95	80	94.84	724	0.0	0.2
5H-4	39.07	39.28	39.17	17.7	392	101	120	133.99	716	0.9	1.1
6H-4	48.48	48.69	48.58	21.8	348	107	157	102.50	739	5.5	1.7
7H-6	59.34	59.56	59.45	23.4	369	110	182	174.01	807	4.7	2.0
8H-4	67.63	67.85	67.74	28.8	257	111	166	182.64	757	12.8	1.9
9H-4	77.14	77.36	77.25	34.2	327	115	237	228.49	818	31.3	2.6
10H-3	83.47	83.69	83.58	37.9	281	116	238	231.67	765	0.7	1.9
11H-2	86.24	86.46	86.35	36.5	318	117	247	242.63	774	10.0	2.6
12X-6	94.99	95.26	95.12	41.0	283	120	200	257.48	864	26.6	3.6
13X-3	101.27	101.54	101.40	43.8	277	97	51	31.04	665	12.9	3.5
14X-5	113.58	113.86	113.72	55.5	276	121	288	266.79	787	1.0	4.5
15X-7	125.91	126.19	126.05	57.7	228	118	285	71.86	851	8.9	5.7
316-C0004D-											
3R-2	119.89	120.10	119.99	52.3	334	93	38	14.10	777	0.7	7.9
4R-2	129.07	129.27	129.17	59.9	302	99	89	29.41	835	0.5	5.9
5R-3	139.54	139.84	139.69	82.2	325	112	16	7.34	899	1.0	7.8
7R-2	152.91	153.26	153.08	75.8	272	95	11	6.06	812	0.3	6.1
13R-2	179.40	179.55	179.47	99.6	249	101	20	10.06	780	1.2	5.1
16R-2	203.13	203.28	203.20	116.2	262	106	26	12.06	995	2.9	7.7
19R-2	226.66	226.98	226.82	104.3	266	95	9	6.11	840	4.0	7.7
23R-1	247.97	248.27	248.12	89.0	315	91	12	5.54	824	29.2	8.4
26R-3	262.59	262.80	262.69	102.1	265	105	20	8.22	894	27.4	6.7
28R-2	271.71	272.11	271.91	98.9	228	104	34	13.71	877	0.2	4.3
30R-3	282.08	282.30	282.19	90.9	217	100	21	9.15	848	0.2	4.6
32R-3	290.11	290.31	290.21	89.7	199	106	48	37.14	895	0.7	4.4
34R-1	296.65	296.85	296.75	79.2	230	103	25	10.25	914	38.7	7.5
36R-2	306.69	306.91	306.80	60.3	290	99	10	4.45	814	71.2	6.5
39R-2	320.18	320.41	320.29	59.5	244	103	8	8.77	788	16.3	5.0
41R-2	329.40	329.49	329.45	51.3	289	99	5	6.09	762	17.8	5.5
44R-3	344.09	344.31	344.20	44.3	303	97	6	3.58	761	4.2	5.9
46R-2	351.91	352.21	352.06	48.6	257	106	51	17.09	812	1.1	5.1
48R-2	361.07	361.25	361.16	46.6	229	102	48	17.65	543	0.1	3.5
49R-2	365.72	365.91	365.81	45.9	207	105	51	24.74	628	0.1	3.8
51R-2	375.45	375.82	375.63	42.2	203	105	49	37.40	612	0.1	4.6
53R-2	383.92	384.29	384.10	42.7	193	105	48	24.12	591	0.1	3.7
55R-2	393.38	393.81	393.60	43.5	229	106	47	18.25	603	0.5	3.2

Notes: \* = shipboard ICP-AES, † = shore-based by ICP-MS. CSF = core depth below seafloor.

**Table T14.** Uncorrected concentrations of trace elements and  $\delta^{18}\text{O}$  in interstitial waters, Site C0004. (See table notes.)

Core, section	Depth CSF (m)			V (nM)	Cu (nM)	Zn (nM)	Rb ( $\mu\text{M}$ )	Mo ( $\mu\text{M}$ )	Cs (nM)	Pb (nM)	U (nM)	Y (pM)	$\delta^{18}\text{O}$ (‰)
	Top	Bottom	Average										
Seawater	NA	NA	NA	32.5	55.0	90.0	1.160	98.0	1.8	0.0	13	0.33	—
316-C0004C-													
1H-3	2.62	2.84	2.73	110	89	141	1.71	19.1	2.7	0.39	18.2	0.95	0.00
1H-6	5.44	5.65	5.54	45	170	827	1.58	10.5	2.7	0.34	14.7	1.02	-0.03
2H-3	8.98	9.20	9.09	11.9	59	64	1.51	6.4	2.2	0.78	2.2	0.79	-0.20
2H-7	13.28	13.49	13.38	27.8	237	568	1.46	5.1	2.2	1.57	2.8	1.18	-0.20
3H-5	19.90	20.12	20.01	22.5	364	310	1.22	4.9	2.1	1.76	2.1	1.35	-0.34
3H-8	22.76	22.98	22.87	20.1	606	643	1.10	7.1	1.6	0.71	2.6	1.48	-0.38
4H-4	29.41	29.63	29.52	19.0	280	380	1.00	5.3	1.9	1.11	2.8	1.21	-0.50
5H-4	39.07	39.28	39.17	38	81	267	0.98	66.1	1.8	0.87	3.3	0.51	-0.67
6H-4	48.48	48.69	48.58	27	454	395	1.03	86.5	1.9	0.32	3.9	1.50	-0.97
7H-6	59.34	59.56	59.45	21	294	1023	0.89	31.8	1.8	0.99	2.1	0.45	-1.19
8H-4	67.63	67.85	67.74	21	62	1096	1.01	103.4	2.7	1.54	1.8	0.61	-1.44
9H-4	77.14	77.36	77.25	18	44	1380	0.96	73.5	2.8	1.90	1.9	1.01	-1.67
10H-3	83.47	83.69	83.58	23	66	609	1.04	53.6	3.2	0.67	2.2	0.72	-1.82
11H-2	86.24	86.46	86.35	13.8	45	1344	0.99	32.1	3.0	0.53	1.6	0.85	-2.04
12X-6	94.99	95.26	95.12	14.5	51	625	0.94	46.8	3.0	0.42	1.7	0.41	-2.23
13X-3	101.27	101.54	101.40	13.2	77	909	0.98	46.8	3.2	0.58	1.5	1.60	-2.11
14X-5	113.58	113.86	113.72	26	52	2299	0.96	46.6	3.2	0.39	2.2	1.75	-2.68
15X-7	125.91	126.19	126.05	19.3	7339	1467	0.96	80.2	3.6	0.19	1.5	1.16	-2.82
316-C0004D-													
3R-2	119.89	120.10	119.99	53	7041	3172	1.08	67.3	4.8	0.58	2.0	3.6	-2.57
4R-2	129.07	129.27	129.17	94	5671	1959	1.10	166	5.1	1.45	3.4	3.0	-2.70
5R-3	139.54	139.84	139.69	15.7	3080	826	1.02	281	4.1	0.37	1.3	0.83	-2.81
7R-2	152.91	153.26	153.08	17.5	492	627	1.06	243	4.8	0.51	1.9	1.49	-2.80
13R-2	179.40	179.55	179.47	23.1	1763	614	1.04	184	4.5	0.95	3.2	1.11	-3.16
16R-2	203.13	203.28	203.20	12.6	3675	1108	0.91	104	3.7	1.63	1.7	0.65	-3.51
19R-2	226.66	226.98	226.82	19.8	3418	1364	0.97	80	4.0	0.88	1.3	1.23	-2.78
23R-1	247.97	248.27	248.12	6.7	6962	933	0.88	95	3.6	3.36	1.0	1.41	-2.43
26R-3	262.59	262.80	262.69	13.3	7891	1407	0.87	102	3.6	0.61	1.0	1.31	-3.67
28R-2	271.71	272.11	271.91	24.3	10015	1227	0.91	91	3.9	0.46	—	1.24	-3.71
30R-3	282.08	282.30	282.19	15.5	16117	1063	0.88	212	3.4	0.59	1.7	0.62	-3.81
32R-3	290.11	290.31	290.21	25.3	6281	1374	0.89	251	4.7	0.59	2.9	0.90	-3.87
34R-1	296.65	296.85	296.75	28.5	727	649	0.83	514	3.4	0.00	0.8	1.04	-3.71
36R-2	306.69	306.91	306.80	16.9	4750	753	0.82	155	3.4	1.02	0.6	1.29	-2.89
39R-2	320.18	320.41	320.29	9.6	7426	588	0.84	83	4.5	0.35	1.4	0.73	-3.57
41R-2	329.40	329.49	329.45	32.6	3188	827	0.86	117	4.3	0.25	1.0	1.08	-3.03
44R-3	344.09	344.31	344.20	35.6	2056	857	0.86	159	4.4	0.48	1.6	0.41	-2.50
46R-2	351.91	352.21	352.06	29.0	162	2272	0.85	142	4.7	0.00	0.98	0.92	-3.87
48R-2	361.07	361.25	361.16	41.3	82	56	0.92	618	5.8	1.57	4.9	0.36	-3.85
49R-2	365.72	365.91	365.81	42.3	368	372	0.94	338	6.2	0.24	5.3	3.1	-4.06
51R-2	375.45	375.82	375.63	28.2	1734	158	0.93	407	5.6	0.69	2.2	0.52	-4.21
53R-2	383.92	384.29	384.10	28.0	1058	289	0.95	336	6.1	—	4.1	—	-4.26
55R-2	393.38	393.81	393.60	18.9	1838	281	0.96	266	6.5	0.83	4.3	0.47	-3.98

Notes: CSF = core depth below seafloor. — = not analyzed.



Table T15. Corrected geochemistry results from interstitial waters, Site C0004. (See table notes.)

Core section	Depth CSF (m)			pH	Alkalinity (mM)	Refractive index	Salinity	Chlorinity (mM)	Cl (mM)	Br (mM)	SO <sub>4</sub> (mM)	Na (mM)	Na (mM)*	Na/Cl	K (mM)	Mg (mM)	Ca (mM)	PO <sub>4</sub> (µM)	NH <sub>4</sub> (µM)
	Top	Bottom	Average																
Seawater	NA	NA	NA	8.9	2.45	1.33946	34.99	560	559	0.86	28.90	480	480	0.86	10.4	54.0	10.55	3.0	19
316-C0004C-																			
1H-3	2.62	2.84	2.73	7.5	4.45	1.33937	34.49	555	554	0.89	25.31	465	485	0.87	12.2	47.8	8.57	15.2	146
1H-6	5.44	5.65	5.54	7.9	6.99	1.33931	34.17	557	556	0.95	17.19	481	479	0.86	12.0	45.9	7.28	13.7	30
2H-3	8.98	9.20	9.09	8.3	6.01	1.33929	34.06	566	565	0.91	13.91	465	486	0.86	11.5	44.8	5.90	26.7	321
2H-7	13.28	13.49	13.38	8.3	11.25	1.33922	33.68	569	568	0.93	6.94	455	491	0.86	11.3	41.1	4.43	33.9	428
3H-6	19.90	20.12	20.01	8.4	13.93	1.33916	33.36	578	577	0.96	0.86	478	499	0.86	11.2	38.4	3.09	33.9	564
3H-8	22.76	22.98	22.87	8.3	18.32	1.33916	33.36	569	568	0.96	0.00	481	492	0.87	11.3	38.0	3.12	41.1	602
4H-4	29.41	29.63	29.52	8.0	16.21	1.33915	33.30	584	583	0.99	0.00	489	507	0.87	10.7	37.3	3.15	49.7	768
5H-4	39.07	39.28	39.17	7.9	15.76	1.33919	33.52	584	583	1.02	0.00	514	509	0.87	10.6	36.1	3.54	55.4	981
6H-4	48.48	48.69	48.58	7.7	14.50	1.33921	33.63	577	576	1.01	0.00	479	509	0.88	9.2	31.1	4.55	48.2	1214
7H-6	59.34	59.56	59.45	7.7	14.59	1.33927	33.95	591	590	1.06	0.00	506	518	0.88	10.0	34.0	4.10	20.9	1311
8H-4	67.63	67.85	67.74	7.7	13.81	1.33931	34.17	601	600	1.08	0.00	493	523	0.87	10.5	34.8	4.38	13.7	1554
9H-4	77.14	77.36	77.25	7.7	14.55	1.33935	34.38	601	600	1.09	0.00	498	525	0.88	10.4	33.9	4.93	16.6	1612
10H-3	83.47	83.69	83.58	7.8	13.94	1.33937	34.49	605	604	1.09	0.00	512	529	0.88	10.8	33.3	5.02	9.4	1700
11H-2	86.24	86.46	86.35	7.7	14.00	1.33938	34.55	607	606	1.13	0.00	499	532	0.88	10.1	33.0	5.27	8.0	1855
12X-6	94.99	95.26	95.12	7.8	13.16	1.33945	34.92	613	612	1.12	0.00	496	536	0.88	10.0	33.0	5.63	10.8	1952
13X-3	101.27	101.54	101.40	7.6	12.28	1.33946	34.98	621	620	1.16	0.00	539	546	0.89	10.4	31.4	5.71	3.7	2311
14X-6	113.58	113.86	113.72	7.8	13.34	1.33963	35.90	625	624	1.13	0.00	525	555	0.89	10.8	31.9	6.51	3.6	2341
15X-7	125.91	126.19	126.05	7.7	11.30	1.33957	35.57	643	642	1.20	0.00	498	564	0.88	9.6	32.3	6.60	10.8	2515
316-C0004D-																			
3R-2	119.89	120.10	119.99	—	—	1.33949	35.15	618	617	1.15	0.00	497	541	0.88	10.1	31.5	6.35	3.2	3267
4R-2	129.07	129.27	129.17	—	—	1.33951	35.27	626	627	1.15	0.00	510	554	0.89	10.2	30.0	6.31	1.7	3445
5R-3	139.54	139.84	139.69	7.6	12.38	1.33955	35.45	632	631	1.11	0.00	535	561	0.90	10.4	28.3	6.65	0.0	3678
7R-2	152.91	153.26	153.08	7.7	11.68	1.33956	35.49	634	633	1.16	0.00	530	560	0.89	10.4	28.4	7.27	1.7	3938
13R-2	179.40	179.55	179.47	7.8	15.55	1.33960	35.73	624	623	1.19	0.00	509	563	0.91	9.3	24.1	7.45	0.0	4724
16R-2	203.13	203.28	203.20	7.5	10.78	1.33962	35.83	639	638	1.22	0.00	511	571	0.90	8.7	24.5	8.18	11.9	4662
19R-2	226.66	226.98	226.82	7.2	10.30	1.33957	35.59	634	633	1.19	0.00	532	568	0.92	8.5	22.1	8.55	11.9	5922
23R-1	247.97	248.27	248.12	6.5	10.49	1.33958	35.62	630	629	1.20	0.00	540	575	0.95	7.4	17.1	8.48	17.8	7671
26R-3	262.59	262.80	262.69	7.2	11.14	1.33972	36.39	643	642	1.20	0.00	557	578	0.91	8.3	21.8	9.29	4.8	5921
28R-2	271.71	272.11	271.91	7.4	10.42	1.33962	35.84	633	632	1.17	0.00	530	570	0.91	8.2	21.3	8.68	3.3	5682
30R-3	282.08	282.30	282.19	7.5	8.12	1.33960	35.75	637	636	1.19	0.00	561	574	0.91	8.5	20.2	8.27	6.3	5869
32R-3	290.11	290.31	290.21	7.6	10.71	1.33962	35.84	638	636	1.23	0.00	544	575	0.91	8.2	20.3	9.14	3.3	5770
34R-1	296.65	296.85	296.75	—	—	1.33960	35.75	633	632	1.19	0.00	545	570	0.91	7.7	19.8	9.09	4.8	6097
36R-2	306.69	306.91	306.80	6.7	9.66	1.33958	35.59	631	630	1.21	0.00	551	581	0.95	6.7	13.9	8.91	11.2	8365
39R-2	320.18	320.41	320.29	7.2	9.69	1.33964	35.92	640	639	1.20	0.00	561	583	0.93	7.7	17.2	9.01	6.5	7192
41R-2	329.40	329.49	329.45	6.8	9.41	1.33960	35.70	634	632	1.23	0.00	561	583	0.95	7.2	13.6	8.91	7.1	7906
44R-3	344.09	344.31	344.20	6.6	9.64	1.33955	35.47	635	634	1.23	0.00	527	586	0.96	6.4	12.8	8.86	3.4	8343
46R-2	351.91	352.21	352.06	7.4	9.60	1.33960	35.73	635	633	1.23	0.00	553	577	0.92	7.3	17.5	9.27	4.8	6546
48R-2	361.07	361.25	361.16	8.1	9.37	1.33959	35.67	635	634	1.18	0.00	547	578	0.92	8.3	17.4	8.52	3.3	6829
49R-2	365.72	365.91	365.81	7.7	8.54	1.33960	35.72	638	637	1.24	0.00	538	580	0.92	7.9	17.2	8.75	3.3	6384
51R-2	375.45	375.82	375.63	7.9	8.81	1.33966	36.04	645	644	1.21	0.00	563	586	0.92	8.1	17.2	8.91	6.1	6339
53R-2	383.92	384.29	384.10	7.9	8.39	1.33964	35.95	643	642	1.22	0.00	562	583	0.91	8.4	18.1	9.05	0.0	6309
55R-2	393.38	393.81	393.60	7.8	7.62	1.33966	36.06	650	649	1.24	0.00	558	591	0.92	8.2	16.5	8.87	1.9	6773

Notes: \* = calculated by charge balance. CSF = core depth below seafloor. NA = not applicable. — = not analyzed.

Table T16. Corrected concentrations of minor elements in interstitial waters, Site C0004. (See table notes.)

Core, section	Depth CSF (m)			Minor elements ( $\mu\text{m}$ )						
	Top	Bottom	Average	Li	B	Sr	Ba	Si	Fe	Mn
Seawater	NA	NA	NA	26	480	87	0.15	150	0.0	0.0
316-C0004C-										
1H-3	2.62	2.84	2.73	24.3	498	84	0.45	625	2.5	2.5
1H-6	5.44	5.65	5.54	24.0	519	83	0.44	676	0.2	1.3
2H-3	8.98	9.20	9.09	25.2	478	86	0.67	695	0.1	0.6
2H-7	13.28	13.49	13.38	23.3	502	84	1.3	682	1.0	0.3
3H-5	19.90	20.12	20.01	18.9	446	90	50	686	0.0	0.1
3H-8	22.76	22.98	22.87	18.8	438	93	54	764	0.3	0.2
4H-4	29.41	29.63	29.52	18.5	408	95	80	724	0.0	0.2
5H-4	39.07	39.28	39.17	17.7	392	101	120	716	0.9	1.1
6H-4	48.48	48.69	48.58	21.8	348	107	157	739	5.5	1.7
7H-6	59.34	59.56	59.45	23.4	369	110	182	807	4.7	2.0
8H-4	67.63	67.85	67.74	28.8	257	111	166	757	12.8	1.9
9H-4	77.14	77.36	77.25	34.2	327	115	237	818	31.3	2.6
10H-3	83.47	83.69	83.58	37.9	281	116	238	765	0.7	1.9
11H-2	86.24	86.46	86.35	36.5	318	117	247	774	10.0	2.6
12X-6	94.99	95.26	95.12	41.0	283	120	200	864	26.6	3.6
13X-3	101.27	101.54	101.40	46.2	250	99	58	734	14.6	4.0
14X-5	113.58	113.86	113.72	55.5	276	121	288	787	1.0	4.5
15X-7	125.91	126.19	126.05	57.7	228	118	285	851	8.9	5.7
316-C0004D-										
3R-2	119.89	120.10	119.99	54.8	320	93	41	838	0.8	8.7
4R-2	129.07	129.27	129.17	62.2	290	100	95	881	0.5	6.3
5R-3	139.54	139.84	139.69	87.2	311	115	17	966	1.1	8.5
7R-2	152.91	153.26	153.08	78.8	259	96	12	853	0.4	6.5
13R-2	179.40	179.55	179.47	105.1	231	102	21	827	1.3	5.5
16R-2	203.13	203.28	203.20	121.5	250	107	28	1043	3.0	8.1
19R-2	226.66	226.98	226.82	124.8	210	97	11	1022	5.1	9.7
23R-1	247.97	248.27	248.12	120.5	232	93	18	1161	43.7	12.7
26R-3	262.59	262.80	262.69	109.2	245	107	21	963	29.9	7.3
28R-2	271.71	272.11	271.91	103.1	214	105	36	919	0.2	4.6
30R-3	282.08	282.30	282.19	97.1	192	101	23	914	0.2	5.0
32R-3	290.11	290.31	290.21	94.1	180	108	52	947	0.7	4.7
34R-1	296.65	296.85	296.75	84.3	206	105	27	987	42.4	8.3
36R-2	306.69	306.91	306.80	74.8	210	104	14	1094	101.2	9.3
39R-2	320.18	320.41	320.29	65.1	204	106	9	895	19.0	5.9
41R-2	329.40	329.49	329.45	59.9	223	103	7	972	23.9	7.4
44R-3	344.09	344.31	344.20	54.2	208	103	9	1090	6.4	9.0
46R-2	351.91	352.21	352.06	50.3	240	107	54	861	1.2	5.4
48R-2	361.07	361.25	361.16	47.9	213	103	51	567	0.1	3.8
49R-2	365.72	365.91	365.81	46.9	193	106	53	653	0.1	4.0
51R-2	375.45	375.82	375.63	42.7	194	105	51	628	0.1	4.8
53R-2	383.92	384.29	384.10	42.7	193	105	48	591	0.1	3.7
55R-2	393.38	393.81	393.60	44.4	216	107	49	626	0.5	3.4

Notes: CSF = core depth below seafloor. NA = not applicable.

Table T17. Hydrocarbon gas concentration from additional headspace gas analysis, Site C0004. (See table notes.)

Core, section, interval (cm)	Depth CSF (m)	Headspace gas (ppmv)			Headspace gas ( $\mu$ M)	
		Methane	Ethane	C <sub>1</sub> /C <sub>2</sub>	Methane	Ethane
316-C0004C-						
1H-2, 116.5–120.5	2.60	10.2	0.0	—	1.84	0.00
1H-5, 115.5–119.5	5.42	25.4	0.0	—	4.95	0.00
2H-2, 115.5–119.5	8.96	61.4	0.0	—	10.05	0.00
2H-6, 117–121	13.26	106.5	0.0	—	19.67	0.00
2H-8, 137.4–141.4	14.88	157.7	3.5	45	30.15	0.67
3H-2, 114.5–118.5	18.46	5,725.4	6.4	899	1,037	1.15
3H-7, 117–121	22.74	18,076.4	7.7	2,337	3,410	1.46
3H-9, 137–141	24.37	23,676.5	10.0	2,366	4,597	1.94
4H-2, 138–142	28.20	19,502.2	7.0	2,787	6,208	2.23
4H-8, 138–142	35.32	50,683.5	15.1	3,367	9,723	2.89
5H-3, 121.5–125.5	39.05	45,672.7	14.4	3,163	8,187	2.59
5H-7, 136.5–140.5	43.63	24,865.1	9.3	2,684	4,852	1.81
6H-7, 147–151	53.10	16,363.0	6.2	2,633	7,502	2.85
7H-3, 115.7–119.7	57.90	32,911.7	11.2	2,951	6,658	2.26
7H-8, 136.5–140.5	62.35	5,944.1	5.8	1,027	1,564	1.52
8H-3, 140–144	67.61	16,202.8	8.0	2,037	3,311	1.63
8H-7, 137–141	71.89	8,616.7	5.4	1,590	1,604	1.01
9H-2, 137–141	75.68	9,545.3	6.7	1,425	1,973	1.38
10H-2, 115.5–119.5	83.45	8,947.3	8.7	1,023	1,873	1.83
11H-1, 137–141	86.19	3,507.3	3.8	913	1,242	1.36
12X-5, 33–37	90.75	7,067.9	5.9	1,201	2,006	1.67
12X-8, 137–141	98.07	4,519.2	5.9	762	1,072	1.41
13X-2, 41–47	100.57	14,322.2	6.9	2,071	4,022	1.94
13X-7, 136.5–140.5	107.16	4,983.1	4.6	1,088	2,002	1.84
14X-4, 110–114	113.56	12,982.4	9.0	1,449	3,055	2.11
14X-7, 136.5–140.5	116.65	5,016.5	4.9	1,032	2,078	2.01
15X-4, 136.5–140.5	123.34	3,577.6	4.5	796	1,474	1.85
15X-6, 110–114	125.89	6,680.5	7.6	876	2,597	2.96
316-C0004D-						
5R-2, 67.5–71.5	139.52	7,403.4	9.2	802	1,657	2.07
7R-3, 45.5–49.5	153.74	12,090.9	8.1	1,484	3,041	2.05
8R-1, 133–137	157.35	5,351.4	5.5	980	1,285	1.31
16R-1, 108.5–112.5	203.11	8,108.9	3.8	2,134	3,094	1.45
19R-1, 11.5–115.5	226.14	4,641.2	3.7	1,264	1,311	1.04
23R-1, 137–141	248.39	8,332.7	5.8	1,445	2,881	1.99
24R-1, 136.5–140.5	252.89	5,459.8	3.8	1,443	2,566	1.78
26R-2, 63.4–67.4	262.57	4,329.4	2.9	1,468	1,449	0.99
27R-1, 137–141	266.39	15,282.0	9.2	1,666	3,503	2.10
30R-1, 137.2–141.2	279.89	7,523.9	4.4	1,696	8,101	4.78
31R-1, 137–141	284.39	4,975.9	2.8	1,778	1,417	0.80
32R-2, 136–140	290.29	14,625.3	5.5	2,636	4,202	1.59
33R-1, 136–140	293.38	14,359.1	4.6	3,121	5,415	1.74
34R-1, 134.5–140.5	297.88	22,618.2	6.3	3,612	8,638	2.39
35R-1, 134.5–140.5	302.38	14,452.4	4.8	2,982	3,463	1.16
36R-1, 113–119	306.66	3,776.3	2.6	1,437	1,151	0.80
39R-1, 105.5–109.5	320.08	6,178.7	4.6	1,348	1,742	1.29
40R-1, 136–140	324.88	11,246.1	3.7	3,074	5,141	1.67
41R-1, 136–140	329.38	4,189.6	3.4	1,234	1,277	1.04
42R-3, 74–78	335.67	2,381.8	2.4	1,007	814	0.81
43R-2, 96.5–100.5	339.40	2,325.7	2.9	815	841	1.03
44R-2, 115.5–119.5	344.07	4,599.8	3.8	1,214	1,175	0.97
45R-1, 137–141	347.39	20,439.0	6.0	3,415	8,958	2.62
47R-1, 137.2–141.2	356.39	6,409.8	2.9	2,214	2,631	1.19
49R-1, 137.5–141.5	365.40	9,126.4	4.8	1,882	2,492	1.32
51R-1, 137.5–141.5	374.40	1,545.0	0.0	—	706	0.00
54R-1, 136–140	387.88	2,079.9	0.0	—	844	0.00
56R-1, 138–142	396.90	2,565.6	0.0	—	1,576	0.00

Notes: CSF = core depth below seafloor. — = not applicable.

Table T18. Headspace gas composition for safety monitoring in sediments, C0004. (See table notes.)

Core, section, interval (cm)	Depth CSF (m)	Headspace gas (ppmv)		
		Methane	Ethane	C <sub>1</sub> /C <sub>2</sub>
316-C0004C-				
1H-1, 137.5–141.5	1.38	3.2	0.0	—
2H-1, 136.7–140.7	7.75	21.2	0.0	—
3H-1, 137.3–141.3	17.25	1,836.4	3.1	587
4H-1, 137.5–141.5	26.76	29,260.9	10.5	2,786
5H-1, 138.5–142.5	36.27	29,748.1	10.8	2,757
6H-1, 138.5–142.5	45.77	16,849.7	6.5	2,610
7H-1, 137.7–141.7	55.26	20,514.7	8.4	2,453
8H-1, 136–140	64.74	12,610.8	6.5	1,936
9H-1, 137.2–141.2	74.25	8,227.4	4.6	1,774
10H-1, 139.5–143.5	82.24	8,141.4	6.0	1,355
11H-1, 137–141	86.17	5,003.7	4.4	1,128
12X-1, 114–118	90.36	5,777.5	6.0	966
13X-1, 137–141	100.09	3,721.5	4.5	832
14X-1, 136.5–140.5	109.59	19,449.1	11.7	1,661
15X-1, 137–141	119.09	11,495.2	9.4	1,217
16H-1, 116.5–120.5	128.39	2,873.4	5.2	555
316-C0004D-				
5R-1, 128–132	138.78	5,477.2	5.5	998
7R-1, 136.5–140.5	152.87	7,370.3	5.5	1,329
8R-1, 133–137	157.33	4,050.6	3.3	1,241
11R-1, 105–109	170.55	6,269.2	6.5	958
16R-1, 108.5–112.5	203.09	2,995.9	2.1	1,448
19R-1, 111.5–115.5	226.62	5,839.7	4.6	1,266
23R-1, 137–141	248.37	2,639.9	2.9	903
24R-1, 136.5–140.5	252.87	2,083.2	2.2	941
28R-1, 137–141	270.87	5,103.1	4.3	1,198
29R-1, 135.5–139.5	275.36	15,386.8	5.6	2,732
30R-1, 137.2–141.2	279.87	10,187.5	4.4	2,333
31R-1, 137–141	284.37	9,991.6	4.8	2,067
32R-2, 136–140	290.27	10,557.7	4.1	2,555
33R-1, 136–140	293.36	4,721.9	2.5	1,870
34R-1, 134.5–140.5	297.85	11,432.1	4.9	2,353
35R-1, 134.5–140.5	302.35	7,295.8	4.0	1,832
36R-1, 113–119	306.63	4,245.8	3.5	1,198
37R-1, 133–141	311.33	4,062.8	2.7	1,510
39R-1, 105.5–109.5	320.06	5,654.4	5.7	998
41R-1, 136–140	329.36	2,460.5	2.7	903
42R-1, 136–140	333.86	4,888.3	4.9	991
45R-1, 137–141	347.37	3,932.6	2.8	1,409
47R-1, 137.2–141.2	356.37	4,038.4	1.9	2,089
49R-1, 137.5–141.5	365.38	5,678.0	3.5	1,626
51R-1, 137.5–141.5	373.14	3,437.0	2.8	1,235
54R-1, 136–140	387.86	4,725.8	2.6	1,805

Notes: CSF = core depth below seafloor. — = not applicable.

Table T19. Carbonate, carbon, nitrogen, and sulfur in sediments, Site C0004. (See table notes.)

Core, section, interval (cm)	Depth CSF (m)	CaCO <sub>3</sub> (wt%)	TOC (wt%)	TN (wt%)	C/N	TS (wt%)	Core, section, interval (cm)	Depth CSF (m)	CaCO <sub>3</sub> (wt%)	TOC (wt%)	TN (wt%)	C/N	TS (wt%)
316-C0004C-							23R-1, 97-98.5	247.98	2.60	0.62	0.11	5.82	0.56
1H-2, 119-120.5	2.61	16.36	0.46	0.06	7.72	0.04	26R-3, 0-1.5	262.59	0.76	0.38	0.10	3.75	0.42
1H-5, 117-118.5	5.42	10.68	0.47	0.06	7.47	0.18	27R-2, 95.5-97	267.37	3.62	0.53	0.07	7.11	0.50
1H-5, 92.5-94	5.17	14.70	0.43	0.07	5.92	0.09	28R-1, 43.5-45	269.94	3.18	0.37	0.05	7.27	0.36
2H-4, 0-1.5	9.20	9.90	0.59	0.07	7.96	0.25	28R-2, 80-81.5	271.72	3.17	0.45	0.08	5.42	0.21
2H-5, 35-36.5	10.99	9.86	0.49	0.07	6.99	0.14	29R-CC, 18-19.5	277.15	6.92	*	0.07	*	0.23
2H-6, 119.5-121	13.27	12.71	0.49	0.07	7.17	0.28	30R-2, 88-92	280.81	6.88	0.34	0.06	5.33	0.16
3H-2, 25-26.5	17.55	15.39	0.42	0.07	6.35	0.16	30R-3, 76.5-78	282.09	8.45	0.31	0.07	4.30	0.13
3H-8, 20-21.5	22.97	11.88	0.27	0.05	5.43	0.18	32R-2, 120-121.5	290.12	0.23	0.37	0.08	4.73	0.17
4H-1, 58.5-60	25.97	15.37	0.39	0.07	5.74	0.22	34R-1, 15-16.5	298.06	1.12	0.41	0.08	4.96	0.23
4H-4, 20-21.5	29.62	7.33	0.47	0.07	6.48	0.34	36R-2, 0-1.5	306.70	3.19	0.42	0.08	5.14	0.21
5H-1, 63-64.5	35.52	3.03	0.41	0.07	5.81	0.37	37R-1, 79.5-81.5	310.60	5.13	0.43	0.06	6.88	0.20
5H-4, 0-1.5	39.07	8.01	0.47	0.07	6.82	0.50	39R-2, 8-9.5	320.18	3.67	0.41	0.08	5.14	0.09
6H-2, 63.5-65	46.45	12.37	0.46	0.08	6.01	0.30	41R-2, 20-21.5	329.61	5.53	0.49	0.09	5.75	0.17
6H-4, 0-1.5	48.48	12.98	0.61	0.09	7.08	0.18	44R-2, 71-72.5	343.61	5.30	0.51	0.09	5.92	0.23
6H-7, 15-16.5	51.76	12.43	0.46	0.08	5.95	0.14	44R-3, 0-1.5	344.10	3.31	0.47	0.10	4.92	0.12
7H-6, 0-1.5	59.35	3.94	0.53	0.06	9.27	0.05	46R-2, 28.5-30	352.20	4.69	0.60	0.09	6.35	0.14
7H-7, 129-130.5	60.85	1.84	0.43	0.07	5.75	0.09	48R-1, 37-38.5	359.88	2.74	0.50	0.09	5.32	0.07
7H-9, 15-16.5	62.53	9.46	0.35	0.04	7.71	0.57	48R-2, 17-18.5	361.08	2.83	0.45	0.09	5.07	0.06
8H-2, 68-69.5	65.47	13.16	0.52	0.08	6.49	0.12	48R-1, 111-112.5	365.12	3.40	0.46	0.08	6.04	0.34
8H-4, 0-1.5	67.64	10.75	0.43	0.08	5.45	0.04	49R-2, 30-31.5	365.72	3.62	0.48	0.09	5.42	0.12
8H-5, 91-92.5	68.76	7.89	0.40	0.06	6.11	0.04	49R-3, 79-80.5	367.61	1.77	0.47	0.08	6.12	0.11
9H-2, 68-69.5	74.98	1.87	0.28	0.06	4.47	0.34	51R-1, 90.5-92	373.91	2.92	0.31	0.08	3.71	0.09
9H-4, 0-1.5	77.15	2.03	0.34	0.05	6.26	0.05	51R-2, 103-104.5	375.45	1.61	0.35	0.08	4.44	0.08
10H-2, 103-104.5	83.31	4.52	0.43	0.07	5.82	0.11	51R-2, 50.5-52	374.93	4.48	0.43	0.09	5.05	0.07
10H-3, 0-1.5	83.48	1.79	0.47	0.06	7.69	0.14	52R-1, 10-11	377.61	4.28	0.55	0.07	8.08	0.11
11H-1, 110.5-113	85.92	3.33	0.40	0.07	5.45	0.13	52R-2, 79-80.5	379.70	3.08	0.46	0.07	6.46	0.26
11H-2, 0-1.5	86.25	4.64	0.43	0.07	6.13	0.22	52R-3, 18-19.5	380.49	3.64	0.43	0.09	4.83	0.15
12X-6, 0-1.5	95.00	2.44	0.42	0.08	5.49	0.18	52R-3, 76.5-78	381.08	2.08	0.37	0.07	5.06	0.23
12X-8, 64-65.5	97.32	4.76	0.40	0.07	5.61	0.39	52R-3, 110.5-112	381.42	1.44	0.44	0.07	5.96	0.37
13X-3, 0-1.5	101.28	0.78	0.38	0.07	5.31	0.12	53R-2, 51-52.5	383.92	1.49	0.36	0.04	10.01	0.13
13X-8, 10-11.5	107.29	2.50	0.45	0.07	6.45	0.13	54R-1, 107.5-109	387.58	3.86	0.44	0.09	4.98	0.11
14X-5, 0-1.5	113.58	0.83	0.47	0.06	8.04	0.20	54R-2, 11.5-13	388.02	5.38	0.45	0.08	5.58	0.49
14X-8, 15-16.5	116.83	1.07	0.32	0.09	3.73	0.20	54R-2, 116-117.5	389.07	5.55	0.41	0.09	4.64	0.09
15X-2, 0-1.5	119.14	6.01	0.44	0.09	5.12	0.26	54R-3, 0-1.5	389.32	6.80	0.39	0.06	6.15	0.16
15X-7, 0-1.5	125.91	4.13	0.40	0.05	7.41	0.25	54R-3, 44-44.5	389.75	6.58	0.40	0.09	4.64	0.17
316-C0004D-							54R-3, 77.5-79	390.09	3.11	0.31	0.05	6.32	0.31
4R-2, 0-1.5	129.08	1.72	0.31	0.06	4.92	0.24	55R-1, 36-37.5	391.37	5.70	0.24	0.07	3.56	0.17
5R-3, 0-1.5	139.55	1.78	0.29	0.07	4.35	0.55	55R-2, 97-98.5	393.39	4.01	0.49	0.09	5.46	0.14
7R-2, 0-1.5	152.91	1.49	0.40	0.08	4.91	0.36							
13R-2, 14-15	179.54	1.46	0.43	0.06	7.19	0.19							
16R-2, 13.5-15	203.27	5.50	0.30	0.07	4.08	0.23							
19R-2, 1-1.5	226.67	6.07	0.41	0.09	4.53	0.43							

Notes: \* = total carbon < inorganic carbon. CSF = core depth below seafloor. TOC = total organic carbon, TN = total nitrogen, TS = total sulfur.

**Table T20.** Sample depth and processing for microbiological and biogeochemical studies, Site C0004. (See table notes.)

Core, section	Depth CSF (m)	Frozen		Anaerobic pack (4°C)	Slurry (-20°C)	
		-80°C	-20°C		FISH	Acetone
316-C0004C-						
1H-1	0.60	X			X	X
1H-1	0.75			X		
1H-1	0.90	X		X	X	
1H-1	1.05			X		
1H-1	1.13	X				
1H-1	1.13		X			
1H-4	4.15	X			X	X
1H-4	4.00			X		
1H-4	3.85	X		X	X	
1H-4	3.70	X				
1H-4	3.60		X			
2H-4	9.99		X			
2H-4	10.07			X		
2H-4	10.22	X		X	X	
2H-4	10.37			X		
2H-4	10.52	X			X	X
3H-4	19.28		X			
3H-4	19.35	X				
3H-4	19.50	X		X	X	
3H-4	19.65			X		
3H-4	19.80	X			X	X
5H-2	36.47	X			X	X
5H-2	36.62			X		
5H-2	36.75	X		X	X	
5H-2	36.92			X		
7H-3	57.35			X		
7H-3	57.43	X				
7H-3	57.53	X		X	X	
7H-3	57.66			X		
7H-3	57.81	X			X	X
9H-2	74.82		X			
9H-2	74.89	X			X	X
9H-2	75.04			X		
9H-2	75.13	X				
9H-2	75.23	X		X	X	
11H-1	86.07	X			X	X
11H-1	86.28			X		
13X-7	105.81		X			
316-C0004D-						
13X-7	105.88	X				X X
13X-7	106.03			X		
13X-7	106.14	X		X		X
13X-7	106.25	X				
4R-2	129.80	X				
7R-2	153.09	X				
19R-1	225.65	X		X		X X
19R-2	226.82	X				
23R-1	248.12	X				
27R-1	265.57	X		X		X X
28R-2	271.11	X	X	X		X X
30R-3	280.78	X	X			X X
32R-2	290.21	X				X X
34R-1	296.75	X	X			X X
36R-2	306.80	X				X
39R-2	320.29	X				X X
39R-3	320.47	X		X		X X
39R-3	320.56	X				
41R-2	329.50	X				X X
42R-1	333.40			X		
42R-1	333.55	X				X X
42R-1	333.73			X		
42R-1	333.88	X				
43R-3	339.52	X		X		X X
44R-3	344.20		X			
51R-1	373.11	X				X X
51R-1	373.42			X		X
51R-1	373.50			X		X
53R-2	384.10				X	
56R-2	396.96		X			
56R-2	397.04	X				
56R-2	397.16			X		X
56R-2	397.46	X				
56R-2	397.31			X		X X

Notes: CSF = core depth below seafloor. FISH = fluorescence in situ hybridization.

Table T21. Thermal conductivity measurements, Site C0004. (See table notes.) (Continued on next page.)

Core, section, interval (cm)	Depth CSF (m)	Method	Thermal conductivity (W/[m-K])		N	Standard deviation (W/[m-K])	Thermal conductivity (W/[m-K]) <sup>f</sup>
			Raw average	Calibrated*			
316-C0004C-							
1H-2, 60	2.02	V10305	0.96	0.91	3	0.25	0.93
1H-4, 40	3.24	V10305	1.03	0.99	3	0.01	1.01
2H-2, 60	8.39	V10305	1.03	0.98	3	0.01	1.01
2H-4, 68	9.88	V10305	1.01	0.96	3	0.00	0.98
2H-6, 60	12.67	V10305	1.05	1.01	3	0.00	1.04
2H-8, 60	14.09	V10305	1.03	0.99	3	0.01	1.01
3H-1, 40	24.79	V10305	1.13	1.09	3	0.01	1.12
3H-2, 60	17.90	V10305	1.02	0.98	3	0.00	1.00
3H-4, 50	19.19	V10305	1.02	0.98	3	0.01	1.00
3H-6, 60	20.72	V10305	1.05	1.00	3	0.01	1.02
4H-2, 60	27.40	V10305	1.08	1.04	3	0.01	1.07
4H-5, 60	30.23	V10305	1.05	1.01	3	0.00	1.03
4H-7, 60	33.10	V10305	0.99	0.94	3	0.02	0.96
5H-2, 50	36.82	V10305	1.01	0.97	3	0.04	0.99
5H-5, 56	39.84	V10305	0.95	0.90	3	0.00	0.92
5H-7, 60	42.84	V10305	1.14	1.10	3	0.01	1.12
6H-1, 60	44.98	V10305	0.93	0.89	3	0.01	0.91
6H-3, 63	47.89	V10305	0.84	0.79	3	0.02	0.81
6H-5, 90	49.59	V10305	1.07	1.03	3	0.00	1.05
6H-7, 60	52.21	V10305	0.95	0.91	3	0.01	0.93
7H-1, 55	54.43	V10305	1.00	0.96	3	0.01	0.98
7H-2, 60	55.90	V10305	0.98	0.93	3	0.00	0.95
7H-5, 60	58.74	V10305	1.09	1.05	3	0.00	1.07
7H-9, 60	62.97	V10305	1.03	0.99	3	0.01	1.01
8H-1, 50	63.88	V10305	0.95	0.91	3	0.01	0.93
8H-3, 50	66.69	V10305	0.97	0.93	3	0.01	0.95
8H-5, 50	68.35	V10305	0.95	0.91	3	0.01	0.93
8H-7, 50	71.00	V10305	1.04	1.00	3	0.01	1.02
9H-1, 50	73.38	V10305	1.04	1.00	3	0.01	1.02
9H-3, 60	76.31	V10305	1.00	0.95	3	0.00	0.97
9H-5, 54	77.90	V10305	1.05	1.00	3	0.00	1.03
9H-7, 40	80.40	V10305	1.15	1.11	3	0.01	1.13
10H-1, 25	81.09	V10305	1.11	1.07	3	0.02	1.09
10H-4, 55	84.24	V10305	1.06	1.01	3	0.01	1.04
11H-1, 30	85.10	V10305	1.17	1.13	3	0.01	1.15
11H-3, 60	87.06	V10305	1.13	1.09	3	0.01	1.11
12X-1, 70	89.92	V10305	1.09	1.05	3	0.00	1.07
12X-3, 90	92.71	V10305	1.14	1.10	3	0.00	1.12
12X-5, 20	94.82	V10305	1.16	1.12	3	0.01	1.15
12X-7, 70	95.97	V10305	1.11	1.06	3	0.00	1.09
13X-1, 60	99.32	V10305	1.07	1.03	3	0.01	1.05
13X-5, 43	103.43	V10305	1.09	1.05	2	0.00	1.07
13X-7, 60	106.38	V10305	0.93	0.89	3	0.01	0.90
14X-1, 60	108.82	V10305	1.13	1.08	3	0.00	1.11
14X-3, 70	111.73	V10305	1.10	1.06	3	0.00	1.08
14X-7, 60	115.87	V10305	0.97	0.92	1	—	0.94
15X-1, 50	118.22	V10305	1.10	1.05	3	0.00	1.08
15X-3, 50	121.04	V10305	1.04	0.99	3	0.00	1.01
15X-5, 75	124.11	V10305	1.06	1.01	3	0.00	1.04
16H-1, 75	127.97	V10305	0.84	0.79	3	0.02	0.81
17H-1, 17	132.85	V10305	1.10	1.06	3	0.01	1.08
18H-1, 56	133.74	V10305	1.06	1.02	3	0.00	1.04
1R-1, 80	100.80	QTM500	1.13	1.13	2	—	1.15
1R-3, 50	103.31	QTM500	1.03	1.03	1	—	1.05
3R-1, 30	119.30	QTM500	0.67	0.67	1	—	0.68
4R-1, 29	128.79	QTM500	1.78	1.78	1	—	1.82
5R-1, 53	138.03	QTM500	1.09	1.09	1	—	1.11
5R-4, 28	140.14	QTM500	0.76	0.76	1	—	0.78
7R-1, 61	152.11	QTM500	0.88	0.88	1	—	0.90
9R-1, 36	160.86	QTM500	1.05	1.05	1	—	1.07
52R-3, 62	380.90	QTM500	1.55	1.55	1	—	1.57
53R-2, 8	383.49	QTM500	1.50	1.50	1	—	1.52
54R-2, 65	388.55	QTM500	1.39	1.39	1	—	1.41
55R-1, 86	391.86	QTM500	1.45	1.45	1	—	1.48
56R-2, 69	397.61	QTM500	1.44	1.44	1	—	1.47

Table T21 (continued).

Core, section, interval (cm)	Depth CSF (m)	Method	Thermal conductivity (W/[m·K])		N	Standard deviation (W/[m·K])	Thermal conductivity (W/[m·K]) <sup>†</sup>
			Raw average	Calibrated*			
316-C0004D-							
1R-1, 80	100.80	V10305	1.13	1.08	2	0.03	1.11
1R-3, 50	103.31	V10305	1.03	0.99	1	—	1.01
3R-1, 30	119.30	V10305	0.67	0.62	1	—	0.63
4R-1, 29	128.79	V10305	1.78	1.75	1	—	1.78
5R-1, 53	138.03	V10305	1.09	1.05	1	—	1.07
5R-4, 28	140.14	V10305	0.76	0.72	1	—	0.73
7R-1, 61	152.11	V10305	0.88	0.83	1	—	0.85
9R-1, 36	160.86	V10305	1.05	1.00	1	—	1.03
52R-3, 62	380.90	V10305	1.55	1.51	1	—	1.53
53R-2, 8	383.49	V10305	1.50	1.46	1	—	1.49
54R-2, 65	388.55	V10305	1.39	1.35	1	—	1.37
55R-1, 86	391.86	V10305	1.45	1.41	1	—	1.44
56R-2, 69	397.61	V10305	1.44	1.41	1	—	1.43

Notes: \* = Thermal conductivities were adjusted based on calibration formulas and constants given in “Physical properties” in the “Expedition 316 Methods” chapter, † = thermal conductivities were corrected for temperature and pressure as described in “Physical properties” in the “Expedition 316 Methods” chapter. CSF = core depth below seafloor. — = not applicable.

Table T22. APCT3 temperature measurements, Hole C0004C. (See table notes.)

Core	Depth CSF (m)	BWT (°C)	Time delay (s)	Fit		Equilibrium temperature (°C)
				Start (min)	End (s)	
316-C0004C-						
3H	25.40	1.90	13.0	1	8.0	3.24
6H	53.90	1.84	21.6	1	7.6	4.77
9H	80.80	—	19.7	1	9.6	6.42
18H	135.00	1.86	25.3	1	21.0	8.86

Notes: CSF = core depth below seafloor. BWT = bottom water temperature. — = not measured.

**Table T23.** Correlation and depth shifts among all holes, Site C0004. (See table notes.)

Depth LSF (m)	Depth CSF-B (m)		Depth shift (m)	
	Hole C0004B	Hole C0004C	Hole C0004D	Hole C0004D
2.6	8.8		6.2	
4.8	11.0		6.2	
6.8	14.8		8.0	
14.7	23.4		8.7	
17.7	26.0		8.3	
23.3	31.0		7.7	
34.9	43.0		8.1	
42.6	49.9		7.3	
48.4	59.1		10.7	
54.7	65.8		11.1	
59.0	70.2		11.2	
63.5	73.6		10.1	
67.5	78.0		10.5	
70.7	80.4		9.7	
80.3	89.1		8.8	
91.5	98.3		6.8	
95.0	102.3	100.8	7.3	5.8
100.6	112.5	106.4	11.9	5.8
105.1	117.6	110.9	12.5	5.8
114.5	128.7	120.3	14.2	5.8
120.8		126.6		5.8
122.0		128.5		6.5
123.6		130.1		6.5
133.5		139.7		6.2
146.0		153.0		6.9
149.4		156.5		7.1
153.9		160.8		6.9
163.6		171.0		7.4
171.2		179.0		7.8
195.7		202.7		7.0
218.9		226.4		7.5
256.1		260.9		4.8
267.5		274.3		6.8
272.6		279.8		7.2
284.6		292.0		7.4
286.9		294.2		7.3
291.9		298.4		6.5
305.2		312.2		7.0
318.2		324.9		6.7
330.3		336.4		6.1
339.8		346.7		6.9
348.5		356.8		8.4
359.2		368.4		9.2
367.0		375.7		8.7
375.4		381.6		6.2
383.0		390.5		7.5
386.3		393.4		7.1

Notes: Hole C0004B logs are from LWD data acquired during Expedition 314. Hole C0004C and C0004D logs are from MSCL-W data from whole-round cores. LSF = LWD depth below seafloor, CSF-B = core depth below seafloor, IODP Method B (see "Expedition 316 methods" chapter).